

MAIKE KÄÄRIK

Nanoporous carbon:  
the controlled nanostructure,  
and structure-property  
relationships





**MAIKE KÄÄRIK**

Nanoporous carbon:  
the controlled nanostructure,  
and structure-property  
relationships



Institute of Chemistry, Faculty of Science and Technology, University of Tartu,  
Estonia

The dissertation was accepted for the commencement of the degree of Doctor of  
Philosophy in Molecular Engineering on April 24th, 2020, by the Doctoral  
Committee of the Institute of Chemistry, University of Tartu.

Supervisors: Senior Research Fellow Jaan Leis, PhD  
Institute of Chemistry, University of Tartu, Estonia

Senior Research Fellow Uko Maran, PhD  
Institute of Chemistry, University of Tartu, Estonia

Opponent: Prof. Dr. Elzbieta Frackowiak  
Institute of Chemistry and Technical Electrochemistry,  
Poznan University of Technology, Poland

Commencement: June 19th, 2020 at 12:15, Ravila 14a, Tartu, room 1020

This work has been partially supported by Graduate School of Functional materials  
and technologies receiving funding from the European Regional Development  
Fund in University of Tartu, Estonia



European Union  
European Regional  
Development Fund



Investing  
in your future

ISSN 1406-0299

ISBN 978-9949-03-339-3 (print)

ISBN 978-9949-03-340-9 (pdf)

Copyright: Maike Käärrik, 2020

University of Tartu Press  
[www.tyk.ee](http://www.tyk.ee)

## TABLE OF CONTENTS

LIST OF ORIGINAL PUBLICATIONS .....	6
LIST OF ABBREVIATIONS .....	7
INTRODUCTION .....	9
1 LITERATURE OVERVIEW .....	10
1.1 Nanoporous carbon .....	10
1.2 Carbide-derived carbon .....	10
1.3 Characterization of carbon materials .....	12
1.3.1 Porosity characterization .....	13
1.3.2 Surface chemistry .....	16
1.3.3 Structure analysis .....	17
1.3.4 Analysis of bonding structure .....	19
1.4 Quantitative structure-property relationship approach .....	19
1.4.1 <i>In silico</i> models for nanomaterials .....	21
1.4.2 Structure-property relationships for the EDL carbon .....	21
2 MATERIALS AND METHODS .....	23
2.1 Synthesis of CDC .....	23
2.2 Texture characterization of CDC .....	24
2.3 Capacitance measurements .....	25
2.4 Quantitative nano-structure-property relationships .....	26
3 RESULTS AND DISCUSSION .....	28
3.1 Synthesis and modification of CDC nanostructure .....	28
3.1.1 Effects of graphitization catalysts on pore size distribution ...	30
3.1.2 Steam-treated CDC .....	31
3.1.3 Biomorphic CDC .....	35
3.2 QnSPR of nanoporous CDC .....	37
3.2.1 TEMA-BF <sub>4</sub> electrolyte case .....	37
3.2.2 SBP-BF <sub>4</sub> electrolyte case .....	40
SUMMARY .....	46
REFERENCES .....	48
SUMMARY IN ESTONIAN .....	59
ACKNOWLEDGEMENTS .....	61
PUBLICATIONS .....	63
CURRICULUM VITAE .....	145
ELULOOKIRJELDUS .....	149

## LIST OF ORIGINAL PUBLICATIONS

The present thesis is based on five articles:

- I. **Käärrik, M.**; Arulepp, M.; Karelson, M.; Leis, J. The Effect of Graphitization Catalyst on the Structure and Porosity of SiC Derived Carbons. *Carbon*, **2008**, *46* (12), 1579–1587.
- II. **Käärrik, M.**; Arulepp, M.; Kook, M.; Mäeorg, U.; Kozlova, J.; Sammelselg, V.; Perkson, A.; Leis, J. Characterisation of Steam-Treated Nanoporous Carbide-Derived Carbon of TiC Origin: Structure and Enhanced Electrochemical Performance. *J. Porous Mater.*, **2017**, *25* (4), 1057–1070
- III. **Käärrik, M.**; Arulepp, M.; Kook, M.; Kozlova, J.; Ritslaid, P.; Aruväli, J.; Mäeorg, U.; Sammelselg, V.; Leis, J. High-Performance Microporous Carbon from Deciduous Wood-Origin Metal Carbide. *Microporous Mesoporous Mater.*, **2019**, *278*, 14–22.
- IV. **Käärrik, M.**; Maran, U.; Arulepp, M.; Perkson, A.; Leis, J. Quantitative Nano-Structure–Property Relationships for the Nanoporous Carbon: Predicting the Performance of Energy Storage Materials. *ACS Appl. Energy Mater.*, **2018**, *1* (8), 4016–4024.
- V. **Käärrik, M.**; Arulepp, M.; Käärrik, M.; Maran, U.; Leis, J. Characterization and Prediction of Double-Layer Capacitance of Nanoporous Carbon Materials Using the Quantitative Nano-Structure-Property Relationship Approach Based on Experimentally Determined Porosity Descriptors. *Carbon*, **2020**, *158*, 494–504.

### Author's contribution

- I: Performed material synthesis, experimental measurements, data analysis and wrote an article.
- II: Performed material synthesis, adsorption measurements, data analysis and wrote an article.
- III: Performed material synthesis, adsorption and electrochemical measurements, data analysis and wrote an article.
- IV: Performed material synthesis, adsorption measurements, participated in the development of *in silico* models and in the writing of an article.
- V: Performed material synthesis, experimental measurements, pre-treatment of data before modeling, developed *in silico* models and wrote an article.

## LIST OF ABBREVIATIONS

AC	activated carbon
ACN	acetonitrile
AIC	Akaike information criterion
APS	average pore size
BET	Brunauer-Emmett-Teller
BJH	Barrett, Joyner and Halenda
BMLR	best multiple linear regression
$C$	capacitance
CC	constant current
$C_{CC}$	capacitance calculated from constant current data
$C_{CV}$	capacitance calculated from cyclic voltammetry data
$C_{CV,g}^-$	gravimetric cathodic capacitance calculated from cyclic voltammetry data
CDC	carbide-derived carbon
CNT	carbon nanotube
CV	cyclic voltammetry
$C_{V,NEG}$	volumetric cathodic capacitance calculated from constant current data
$D_{el}$	bulk density of electrode
DFT	density functional theory
EDL	electrical double-layer
EDLC	electrical double-layer capacitor
EDX	energy dispersive X-ray spectroscopy
EELS	electron energy loss spectroscopy
FTIR	Fourier-transform infrared spectroscopy
$h_2^*$	double mean value
$h_3^*$	triple mean value
HRTEM	high-resolution transmission electron microscopy
IUPAC	International Union of Pure and Applied Chemistry
NLDFT	non-local density functional theory
PC	propylene carbonate
PSD	pore size distribution
PTFE	polytetrafluoroethylene
QSAR	quantitative structure-activity relationship
QSPR	quantitative structure-property relationship
QnSPR	quantitative nano-structure-property relationship
QSDFT	quenched solid density functional theory
$R^2$	squared coefficient of correlation
$s^2$	squared standard error of regression
$S_{BET}$	specific surface area by Brunauer-Emmett-Teller
SBP-BF <sub>4</sub>	spiro-(1,1')-bipyrrrolidinium tetrafluoroborate
$S_{dft}$	specific surface area by density functional theory

SEM	scanning electron microscopy
SSA	specific surface area
TEM	transmission electron microscopy
TEMA-BF <sub>4</sub>	triethylmethylammonium tetrafluoroborate
TGA	thermal gravimetric analysis
$V_{\mu}$	micropore volume
$V_{\text{CO}_2[0.4-0.7]}$	measured pore size fractions from CO <sub>2</sub> adsorption
VIF	variance inflation factor
$V_t$	total pore volume
XPS	X-ray photoelectron spectroscopy
XRD	X-ray diffraction
$\hat{\sigma}$	estimated model scale parameter (standard deviation of the response variable)

## INTRODUCTION

Environmental issues are becoming more and more topical every year and therefore more and more attention is being paid to the introduction of new renewable energy sources. The wide range of these applications requires materials whose structure can be precisely controlled and which also have cost-effective synthesis schemes. Such material is nanoporous carbon, which is characterized by a large surface area and well-controlled pore size distribution (PSD), where most pores are below 1 nm.

Nanoporous carbon has proven to be an attractive adsorbent in the storage of different gases [1], or in purification and separation systems [2–4]. Even more important is the use of nanoporous carbons as an electrode material in energy storage devices, such as batteries and supercapacitors [5–8], or as an additive to support the oxygen reduction catalyst of ion exchange membrane fuel cells [9–11]. In these applications, the electrostatic interaction between the electrolytic ions and the surface of the carbon electrode plays an important role, such as in the case of an electric double layer capacitor (EDLC), for which the general rule is that the larger the accessible surface, the higher the energy capacity. In addition to the relationship between specific surface area and capacitance, the relevance of the pore size distribution of carbon material has been discussed [7].

Carbide-derived carbons (CDC) with well-controlled porosity and PSD [12] have received increasing attention in recent decades as prospective high-capacity electrode materials. The peculiarity of the CDC is that carbon particles “remember” the shape and dimensions of the initial carbide and are significantly influenced by its chemical composition and structure. This allows the production of carbon materials with the desired micro- and macrostructure by varying the initial carbide and synthesis conditions [13]. For each nanoporous carbon application, there is a material with an optimal nanostructure, with a suitable porosity and pore size distribution. Therefore, controlling the process of modifying the nanostructure is crucial in finding materials suitable for different applications.

This dissertation focuses on a study of various methods of controlling the nanostructure of CDCs with the aim of seeking quantitative relationships between experimental properties relevant to practical applications and the structure of porous carbon material. A reliable and high-quality database of nanoporous carbon materials and their structural properties was designed. For this a large number of CDCs were synthesized from metal carbides or similar precursors by varying the synthesis conditions, and post-treatment methods, coupled by a thorough analysis of their porous structure. The systematic database created the preconditions for the development of quantitative nanostructure-property relationship (QnSPR) models and the developed models made it possible to explain the electrical double-layer capacitance based on the structure of nanoporous carbon and make predictions for similar nanoporous carbon material.

# 1 LITERATURE OVERVIEW

## 1.1 Nanoporous carbon

Nanoporous carbon materials have a large specific surface area, variable pore size distribution and skeletal structure, depending on the precursor materials, synthesis conditions and post-treatment methods [14]. Activated carbon (AC) forms the majority of the nanoporous carbon. Since AC is prepared by the pyrolysis of organic starting materials with simultaneous or subsequent activation of a carbon derivative, its structure depends to a large extent on the carbon content of the precursor and the activation method used [14, 15]. Activated carbon can be made from many precursors [4], such as: sugar [16], vegetables [17, 18], wood [19, 20], organic resins [21, 22], and various biomass [23–26].

Template-made nanoporous carbons are produced using porous materials of regular structure (like different zeolites) that enables a precise control over the pore size distribution. For example, zeolite-templated carbons consist of curved graphene frameworks and a uniform micropore size [27]. CDCs are a large family of nanoporous carbons, which can also be considered as template-made carbon materials. The structure and porosity of CDCs vary widely and are strongly influenced by the regular composition and crystalline structure of the metal carbide used as the carbon feedstock [13].

## 1.2 Carbide-derived carbon

CDC is a porous carbon obtained by the removing of metal atoms from metal carbide by halogenation, thermal or hydrothermal processing [12]. CDC is produced by chlorination from many different carbides [28] such as  $\text{Al}_4\text{C}_3$  [29, 30],  $\text{SiC}$  [31, 32],  $\text{Mo}_2\text{C}$  [33, 34],  $\text{TiC}$  [35, 36],  $\text{ZrC}$  [37],  $\text{NbC}$  [38–40],  $\text{B}_4\text{C}$  [41],  $\text{Fe}_3\text{C}$  [42],  $\text{VC}$  [38] and others [32–34]. The unique feature of CDC is that carbon particles remember the shape and size of their predecessor carbide, and their structure is also significantly influenced by the structural composition of this carbide. Scanning electron microscopy (SEM) images of the starting carbide and its synthesized carbon (Figure 1) show that the macro- and microstructure of the CDC retains the shape and dimensions of the starting carbide. The general rule is that the higher the synthesis temperature, the higher the structural order. Thus, it is possible to synthesize carbon materials with the desired macro- and microstructure by changing the carbide type and the synthesis parameters [46]. Kukushkina *et al.* showed that using the nonstoichiometric titanium carbide, the larger average micropore size is achieved in CDC as compared to stoichiometric  $\text{TiC}$ , and the average mesopore size increases by reducing carbon content in carbide [47]. The etching of  $\text{Ti}_3\text{SiC}_2$  can generate a larger pore volume compared with  $\text{TiC}$  or  $\text{SiC}$  [13] and the CDCs synthesized from  $\text{Ta}_4\text{HfC}_5$  and  $\text{WTiC}_2$  demonstrate higher specific surface areas and a higher degree of mesoporosity [48]. The wider pore size distribution of CDC is

achieved by chlorinating the carbonitride ( $\text{TiC}_{1-x}\text{N}_x$ ). In this case, the activation of CDC during chlorination occurs *in situ* due to the degradation of low-stability carbon nitrides [49–51].

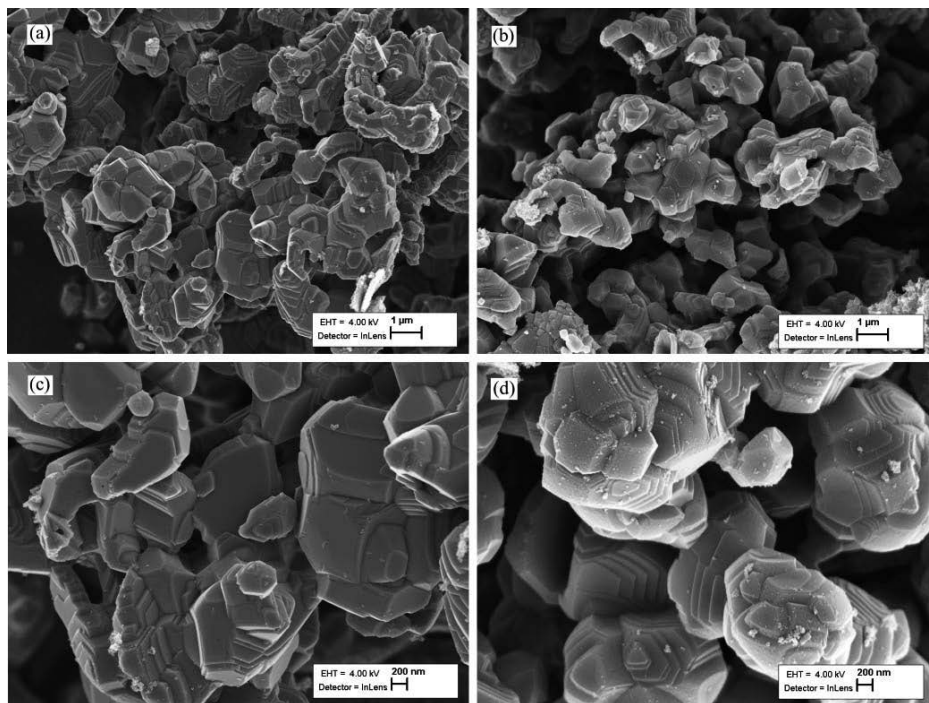


**Figure 1.** High-resolution SEM images of precursor biomorphic TiC (a, c) and CDC (b, d) [52].

In most cases, chlorination is used in the preparation of CDCs, and there are few examples of the use of other halogens [53, 54]. Chlorination temperatures above 1000 °C increase the proportion of graphitic carbon in the CDC, but also increase the average pore size due to large voids between the graphitic flakes and the ribbons. [36]. Catalysts, such as d-metals Fe, Co and Ni, increase the graphitization and formation of nanostructure during the chlorination of carbides [35]. Catalytic d-metals as impurities may be present in the precursor carbide material [30]. The degree of graphitisation in the CDC, thus, depends on both the amount of catalyst and the synthesis temperature. For example, d-metal chlorides are successfully used in the synthesis of graphite-structured carbon from TiC and  $\text{Al}_4\text{C}_3$  at relatively low temperatures [30, 35]. However, studies also show that by increasing the amount of catalyst and raising the synthesis temperature, the degree of graphite can be changed in the desired direction [35, 55]. In addition, Jeong *et al.* have shown that the presence of an iron catalyst promotes

the growth of a highly ordered carbon phase during the formation of CDC from SiC [56]. It is also possible to vary the ratio of graphite to amorphous structure in carbon material by using core-shell carbonaceous materials and a catalyst on the shell porous surface [57].

In addition to varying the synthesis temperature and starting carbide, the structure of a CDC can be influenced by chemical or physical activation. Typically, the chemical activation is performed with KOH [58–60], while the physical activation is made with CO<sub>2</sub> [61–64] or water vapour [14, 65] or a combination of both [66]. Both activation strategies are quite effective for generating new pores and increasing the volume of initially small pores. However, the disadvantage of chemically activated carbon materials is much higher oxygen content than in physically activated ones [59, 67]. It has been proved that the etching of carbon material by water vapor etches carbon approximately 6 times faster than CO<sub>2</sub> [14, 65] and that low-structured carbon materials are more susceptible to activation than carbon with high structural order [68]. The CO<sub>2</sub>-activation mainly causes microporosity, while the water vapour also widens the micropores due to the different surface oxygen groups formed by each activation agent [69, 70].

Biomorphic materials do have unique cellular structure, making biomorphic carbides attractive candidates in CDC synthesis. The methods for making biomorphic carbides are sol-gel technology, liquid infiltration, chemical vapor infiltration and carbothermal reduction [71, 72]; most of them focus on SiC preparations for different applications [73–76]. SiC with a wood-like macroporosity has been made from birch wood by polycarbosilane impregnation [77], and the amount of polycarbosilane allows to control the volume and surface area of micropores of CDC, derived from this biomorphic SiC. In another example, Kormann *et al.* showed that CDC derived from biomorphic paper-origin TiC or SiC, retains the fiber morphology of the paper and gives narrow pore size distribution, which can be further modified by physical activation [62, 78, 79].

### 1.3 Characterization of carbon materials

Different applications using carbonaceous materials require specific carbon structure, such as certain pore size distributions or a specific binding of carbon or the carbon of certain morphology. Consequently, appropriate analytical and carbon structure descriptions methods must be selected when studying carbon for specific application. Figure 2 gives an overview of analytical methods frequently used to characterize carbon materials. Within the current dissertation, the main emphasis is on porosity analysis. Other analytical methods are therefore only briefly discussed in the following text.

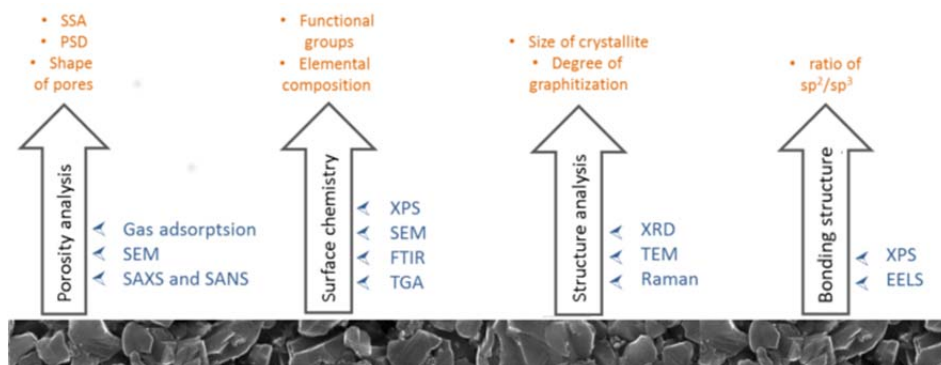


**Figure 2.** The most widely used techniques for characterization of carbon materials.

### 1.3.1 Porosity characterization

The main characteristics of porous materials, including carbon materials, are the specific surface area (SSA,  $m^2g^{-1}$ ), specific pore volume (usually micro ( $V_\mu$ ) or total ( $V_t$ ) pore volume,  $cm^3g^{-1}$ ) and pore size distribution (PSD) [4, 80, 81]. According to IUPAC, the pores are divided into three main groups [81]:

- micropores - pores with diameter smaller than 2 nm;
- mesopores - pores with diameter between 2 and 50 nm;
- macropores - pores with diameter over 50 nm.

The micropores are further subdivided into ultra-micropores (narrow micropores less than 0.7 nm) and super-micropores (wide micropores 0.7–2 nm). In general terms, the expressions like “nanopore” and “nanoporous material”, as used in recent years, refer to pore sizes up to 100 nm [80–82].

The most common technique for measuring porosity parameters is a gas adsorption. Upon adsorption, the gas molecules accumulate on the adsorbent surface by increasing the pressure, whereas in the course of desorption, the adsorbed gas is removed from the adsorbent by reducing the pressure. Gas adsorption isotherm is a simple relationship between the amount of adsorbed gas and the pressure, and measuring the adsorption isotherm, the adsorbent is kept at a constant temperature, usually near to the boiling point of the adsorbed gas. The basic isotherm shapes of the IUPAC classification [81, 83] are shown in Figure 3.

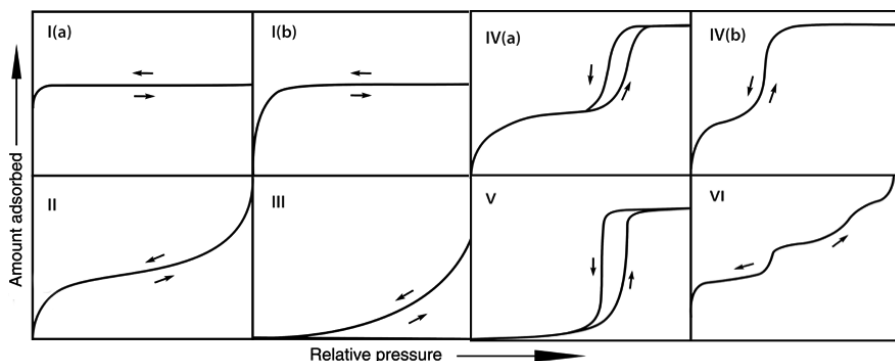


**Figure 3.** IUPAC classification of gas physisorption isotherms. (Adapted from [81].)

Isotherm shapes provide useful preliminary information about pore structure before making accurate calculations [4, 80, 81]. The main feature of the Type I isotherm is the long plateau, which refers to highly microporous material. Type I(a), however, refers to a narrow distribution of micropores, whereas I(b) shows the distribution of the wider micropores. The Type II and III isotherms are characteristic of materials that are non-porous or macroporous. The Type IV isotherm is characteristic of a material, which is micro-mesoporous. In most cases, the Type IV isotherm also shows a hysteresis loop (Type IV(a)). The Type V and VI isotherms occur very rarely. The Type VI isotherm, for example, is associated with layer-by-layer adsorption on a very uniform surface such as graphitized carbon. The most characteristic isotherm shapes of nanoporous carbon materials are Type I and IV, as measured by  $N_2$  adsorption.

Hysteresis (see isotherms IV(a) and V in Fig. 3), which is of five different types H1 – H5 according IUPAC [80, 81], is mostly associated with capillary condensation of the adsorbate in mesopores. H1-type hysteresis loop characterises materials with a similar pore distribution and describes a good pore inter-connection. The H2 loop is the characteristic of materials with a complex shape and distribution of pores and is therefore quite difficult to interpret. H3 and H4 loops are characteristic of slit-like pores, wherein H3 loop coexists with Type II isotherm and H4 loop with Type I isotherm. H4-type hysteresis loop is often associated with narrow slit-like pores in micro-mesoporous carbons. The H5 loop is unusual and associated to the characteristic shape of mesopores, which may be either open or partially blocked.

Carbon materials have been characterized mainly by the adsorption of Ar,  $N_2$  and  $CO_2$  gas at 77 K, 87 K and 273 K, respectively [4, 81, 84–86]. Despite similar kinetic dimension, their behavior as an adsorbate is different and therefore the choice of the suitable adsorbate-gas should be carefully considered. Also, the pore size should be considered when selecting a method, for example, especially small pores cannot be measured by the same technique as meso- and macropores. Most frequently, the nitrogen adsorption is used to study carbon

materials, but it has drawbacks, such as the specific interaction of  $N_2$  with surface functional groups. The difficulty of measuring very narrow micropores due to diffusional limitations at cryogenic temperatures must be taken into account. To eliminate the latter problem,  $CO_2$  is recommended for the analysis of ultramicropores, the adsorption of which is measured at 273 K [81, 84, 85].

The Brunauer-Emmett-Teller (BET) [87] method is a most common technique to estimate the specific surface area ( $S_{BET}$ ) of porous carbon. The method is based on a multilayer adsorption model described by the adsorption isotherm equation:

$$\frac{1}{W\left(\left(\frac{P_0}{P}\right)-1\right)} = \frac{1}{W_m C} + \frac{C-1}{(W_m C)} \left(\frac{P}{P_0}\right), \quad (1)$$

where  $W$  is the weight of the gas adsorbed at a relative pressure  $P/P_0$ , and  $W_m$  is the weight of the adsorbate in a monolayer of surface coverage and  $C$  is a dimensionless BET constant related to the enthalpy of adsorption of the adsorbed gas.

BET method is suitable mostly for Type II and Type IV isotherm, but extra care is needed with micropores (Type I isotherm) because of the difficulty to separate the monolayer-multilayer adsorption and micropores filling [4, 81, 84]. Nevertheless, the BET method (with a suitable relative pressure range) is still a widespread method for evaluating and comparing porous carbon materials.

For calculating the total volume of the pores ( $V_t$ ), the pressure of the adsorbed gas must be as close as possible to the saturation pressure. Then the  $V_t$  is equal to  $V_{liq}$ , by assuming that all the pores are filled with liquid adsorbate.  $V_t$  can be calculated with the equation:

$$V_t = V_{liq} = \frac{P V_{ads} V_M}{RT}, \quad (2)$$

where  $P$  and  $T$  are ambient pressure and temperature,  $V_M$  is the molar volume of  $N_2$  ( $34.7 \text{ cm}^3 \text{ mol}^{-1}$  at 77 K) and  $V_{ads}$  is the volume of nitrogen adsorbed [88].

In order to determine micropore volume ( $V_\mu$ ) the  $t$ -method is most often used, which is based on standard isotherms and  $t$ -curves describing the statistical thickness ( $t$ , nm) of the adsorptive film on a non-porous substrate [89, 90]. The statistical thickness of the adsorbed nitrogen layer is defined as:

$$t = 0.354 \cdot \frac{V_a}{V_m}, \quad (3)$$

where  $V_a$  is the amount of adsorbed nitrogen,  $V_m$  is the amount of nitrogen adsorbed in the monolayer and the constant, 0.354 nm, is a thickness of single nitrogen layer. For porous materials, the  $t$  parameter can be calculated from empirical  $t$  vs.  $P/P_0$  relationships proposed by Halsey [91] or de Boer methods [92], whereby the preferred one for microporous adsorbents is the de Boer equation:

$$t(\text{\AA}) = \left[ \frac{13.99}{\log(P_0/p) + 0.034} \right]^{1/2}. \quad (4)$$

For microporous material the  $V_a-t$  curve, so called  $t$ -plot, indicates a positive intercept ( $i$ ) and converting the intercept to a liquid volume, we can calculate the micropore volume ( $V_\mu$ ) according to the equation:

$$V_\mu = i \cdot 0.001547. \quad (5)$$

The constant 0.001547 represents the conversion of the gas volume to the liquid volume in the case of nitrogen adsorption at 77 K.

An alternative to the BET and  $t$ -plot methods is the DFT method that also measures the specific surface area and PSD for micro- and mesoporous material. The DFT model is based on the concept that the free energy of a system such as a liquid in a porous material can be expressed as a density function [93],

$$N\left(\frac{P}{P_0}\right) = \int_{W_{min}}^{W_{max}} N\left(\frac{P}{P_0}, W\right) f(w) dW, \quad (6)$$

where  $N\left(\frac{P}{P_0}\right)$  is the experimental data,  $f(w)$  PSD function and  $N\left(\frac{P}{P_0}, W\right)$  the isotherm on a single pore of width  $W$  [4, 88].

Also, various mathematical models are available [81, 85, 86, 88], which are applied to model the pores of different geometry (cylindrical, slit, spherical or hybrids) and surface chemistry: non-local (NLDFT) and quenched solid (QSDFT) density functional theories. The QSDFT model is found as the best one for micro-mesoporous carbon and it takes quantitatively into account the surface geometrical inhomogeneity characterized by a roughness parameter [81, 94]. Although DFT methods have been used most frequently to calculate PSD for micro- and mesopores, the Barrett-Joyner-Halenda (BJH) method [95] is also applied, but it must be kept in mind that this method underestimates the pore sizes for narrow mesopores [81]. The BJH method calculates pore size distribution from experimental isotherms using the Kelvin model of pore filling [81].

### 1.3.2 Surface chemistry

Carbon materials, depending on their preparation history, contain different guest atoms and different functional groups on their surface. The surface chemistry of carbon material can be studied by energy dispersive X-ray spectroscopy EDX and X-ray photoelectron spectroscopy (XPS). While EDX gives a general understanding on the quantities of different heteroatoms in carbon skeleton, the XPS delivers specific information on surface chemistry – elemental composition and the bonding of heteroatoms on carbon surface. Fourier transform infrared spectroscopy (FTIR) provides information on surface functional groups.

In IR spectra, most carbon samples have peaks in 3000–2850  $\text{cm}^{-1}$  area, which belong to the C–H symmetric and asymmetric vibrations from  $\text{CH}_2$  and  $\text{CH}_3$  groups [96]. The oxygen-containing groups have vibrations at around 1000–1700  $\text{cm}^{-1}$ ; the peak at 1720  $\text{cm}^{-1}$  is caused by C=O stretching [96]. The vibrations at around 1000–1200  $\text{cm}^{-1}$  belong to the functional groups like C–O and C–O–C in esters and ethers [97]. The peak at 2820  $\text{cm}^{-1}$  is the characteristic of nitrogen contamination [96]. Thermal gravimetric analysis (TGA) also provides information about the quantities of oxygen surface groups. However, for the precise designation of functional groups, it is advisable to use a combined analysis of TG-FTIR, TG-MS or TG-XPS [4, 98, 99].

### 1.3.3 Structure analysis

Since most carbon materials are polycrystalline, X-ray diffraction (XRD) is often used to characterize their structural order. The X-ray spectrum of powdered nanoporous carbon typically shows up to 4 diffraction peaks representing the order of the graphite-like structural fragments: 002 and 004 diffraction peaks at  $\sim 26^\circ$  ( $2\Theta$ ) and  $\sim 54^\circ$  ( $2\Theta$ ), respectively, corresponding to the parallel graphene layers; 10 and 11 diffraction peaks at  $\sim 43^\circ$  ( $2\Theta$ ) and  $\sim 78^\circ$  ( $2\Theta$ ), respectively, corresponding to the in-plane symmetry along the graphene layers. In the case of natural graphite with high planar crystalline regularities, peak 10 is split into peaks 100 and 101, with much higher intensities and narrower shapes compared to amorphous carbon [98]. To calculate the mean diameter  $L_a$  and the height  $L_c$  of the crystallite, one can use the Sherrer's formula:

$$L_{a,c} = K\lambda/\beta\cos\Theta, \quad (7)$$

where  $\lambda$  is the wavelength of the X-ray radiation,  $\beta$  is the width of the corresponding peak at half height in radians (in terms of  $2\Theta$ ) and  $K$  is a constant depending on the reflection [100]. The values of peaks 002 or 004 are used to calculate  $L_c$  and the values of peaks 10, 11 or 100 are used to calculate  $L_a$  [101].  $L_a$ ,  $L_c$  and  $d_{002}$  are thus basic parameters that characterize the structure of carbon materials using XRD analysis [102].

XRD analysis also allows the degree of graphitization ( $G$ ,  $q$ ) to be characterized by the empirical equations:

$$G(\%) = \frac{0.3440 - d_{002}}{0.3440 - 0.3354} 100, \quad (8)$$

where 0.3440 (nm) is the interlayer spacing of fully non-graphitized carbon, 0.3354 is the interlayer spacing of the ideal graphite crystallite and the  $d_{002}$  is the interlayer spacing derived from XRD (nm) [103].

Another way to estimate the degree of graphitization ( $q$ ) is to compare the relative intensities of the 002 and 100 reflections according to the following empirical formula:

$$q(\%) = \frac{I_{002}/I_{10}}{14.3} 100, \quad (9)$$

where the empirical constant 14.3 corresponds to the ratio of  $I_{002}$  and  $I_{10}$  (intensities of 002 and 10 diffraction peaks) in high-density pyrolytic carbon without amorphous constituent, when most of the graphene sheets are organised into packets [29, 104].

Raman spectroscopy effectively characterizes porous carbon materials including crystalline, nanocrystalline and amorphous carbon [98, 100]. The major magnitudes of the Raman first-order spectra of carbon materials are the so-called D (disordered) and G (graphitic) peaks at  $\sim 1360 \text{ cm}^{-1}$  and  $\sim 1560 \text{ cm}^{-1}$ . Although the G-band is called as graphite peak, it appears due to the bond stretching of pairs of  $\text{sp}^2$  atoms and does not distinguish between carbon bonding in rings or in chains. The D-band, whereas, is due to the breathing modes of  $\text{sp}^2$  atoms in rings, and it is forbidden in the graphitic carbon [100, 105]. The mean crystallite diameter  $L_a$  can be found using the Tuinstra and Koenig formula [106]:

$$L_a = 4.4(I_D/I_G)^{-1}, \quad (10)$$

where  $I_D$  and  $I_G$  are the areas or intensities of the D and G peaks, respectively. For more amorphous materials, the use of the Ferrari-Robertson (F-R) formula is justified,

$$I_D/I_G = C(\lambda)L_a^2, \quad (11)$$

where  $C(\lambda)$  is a wavelength dependent constant [100]. Carbon materials show additional peaks in the second order region of  $\sim 2700$  to  $3300 \text{ cm}^{-1}$ . The second order peak of the D-band (2D) at  $\sim 2700 \text{ cm}^{-1}$  is historically named as the G'-band as it appears in more graphitic carbons [105]. D+G peak at  $\sim 2950 \text{ cm}^{-1}$  is a combination of D- and G-bands suggested to be a defect-induced mode and only occurs in disordered carbons, and the peak at  $\sim 3250 \text{ cm}^{-1}$ , called 2D', is a counterpart in the second order spectrum of the D'-band (at  $\sim 1620 \text{ cm}^{-1}$ ) [107, 108].

Transmission electron microscopy (TEM) makes it possible to study specific aspects of carbon nanostructures [109]. For example, Oschatz *et al.* proved that high-resolution TEM (HRTEM) analysis is sensitive enough to detect even small variations in the CDC nanostructure [110]. TEM has also been effectively used to visualise the effects of synthesis temperature [30, 41, 42, 111] and starting carbide [112] on the structure of CDC.

### 1.3.4 Analysis of bonding structure

In carbon materials, each carbon atom is bonded to two ( $sp$  bonding), three ( $sp^2$  bonding) or four ( $sp^3$  bonding) other carbon atoms. By the type of bonding one can divide the carbon family into diamond ( $sp^3$ ), graphite ( $sp^2$ ) and carbene ( $sp$ ). Amorphous carbon, such as CDC, mostly consists of the mixture of structures of  $sp^2$  and  $sp^3$  bonding type, and is rarely represented by the structure of  $sp$  bonding type [90, 98, 113].

Electron energy loss spectroscopy (EELS) and XPS allow to measure the ratio of  $sp^2/sp^3$  [113, 114]. EELS studies reveal that CDCs have high  $sp^2$  content (80-98%) and this depends on precursor carbide [36, 112]. However, it should be noted that the penetration depth of EELS and XPS measurements is different, so their results are not directly comparable [112, 114]. While XPS may not be the best method estimate the overall  $sp^3/sp^2$  ratio, it has justified its use with carbon materials with significant surface effects [114], as well as for analyzing the composition of elements on the carbon surface [99]. When studying high-resolution XPS spectra, one must remember that the result always depends on the model used for fitting ( $O_{1s}$ ,  $C_{1s}$  or  $N_{1s}$ ) [4, 99, 115].

## 1.4 Quantitative structure-property relationship approach

The development of new materials with innovative properties can be approached both experimentally and computationally. The latter, the computational approach, can be broadly divided into two, methods applying physics models (*e.g.*, quantum chemistry, molecular mechanics, molecular dynamics) or methods driven by data (with the aim of identifying relationships within data, which in turn are transformed into computational models).

The most prominent example of computational models driven by data analysis are quantitative structure-property relationships (QSPR) that use a variety of statistical data analysis methods, as well as artificial intelligence and machine learning, and various cheminformatics solutions [116]. QSPR approach started prominent development in the context of physical organic chemistry (*i.e.* chemical reactivity), medical chemistry (such as drug design), environmental chemistry (for example predictive toxicology) and many other fields of chemical industry [116]. The broad aim of the approach is to make experimental chemistry research more efficient, as it helps to better understand and predict on structural basis the processes under the study, and thus helps to achieve the desired result more quickly.

QSPR is presented through following mathematical representation [117, 118]:

$$\text{Property} = f(\text{Structure}), \quad (12)$$

where Structure is represented with molecular descriptors that characterize chemical or material structure.

Typically, QSPR uses molecular descriptors [117] derived from theoretical calculations (*e.g.*, graph theory and quantum mechanics). Unfortunately, modern knowledge does not yet allow us to calculate theoretical molecular descriptors for nanostructured heterogeneous materials (such as nanoporous carbon) as we do for small molecules. In this case, it is rational to perform experimental measurements that allow the structure of the material to be described numerically, so called experiment-derived structure descriptors, and that can be used in QSPR as molecular descriptors.

Several statistical methods, or machine learning algorithms, are suitable for developing QSPRs. Regression-based approaches, such as multi linear regression (MLR) and partial least squares (PLS), are most common [116, 118]. In recent years, a wide range of machine learning methods have been used to develop models, such as artificial neural networks (ANN),  $k$ -nearest neighbors ( $k$ -NN), linear discriminant analysis (LDA), decision trees (DT), random forests (RF), and support vector machines (SVM) [116]. Machine learning methods are used in cases when there is a complex, often non-linear, relationship between property and structure of material, and this makes it difficult to describe the property under study by linear regression [119].

Regardless of the mathematical form of the QSPR, the selection of molecular descriptions into the model is an important step, as the number of molecular descriptions is usually large. Intuition often does not help here, and therefore different methodologies are used to select molecular descriptors [120]. One of the most common ways of selection is to stepwise add molecular descriptors to the model and check their effect on the model statistics. In the case of MLR one of the typical approaches is best multi-linear regression (BMLR) [121] stepwise forward selection algorithm that eliminates non-significant descriptors and then incrementally adds significant descriptors to the model *via* checking various statistical parameters. The final model has the best representation of the property in the given descriptor pool within the given number of parameters. Besides forward (or bottom-up) algorithms, also backward (or top-down) approach can be used, where the full set of molecular descriptors is included into the initial model and insignificant descriptors are eliminated step by step until only descriptors with statistically significant coefficients are left in the model [122, 123].

When using QSPR models, their applicability domain and diagnostics are providing information on how well the model is derived and to what extent it is usable [124–126]. In the case of MLR, the most common way to assess the goodness of a model is the so-called influence plot, also known as the Williams plot [127]. It allows to identify outliers, high leverage data points (data points with an unusual combination of descriptor values), characterized by their hat values, and influential data points (data points that exert substantial influence on the regression coefficients), characterized by Cook’s distances [123, 128].

Nanostructured heterogeneous materials cause the change in naming convention for QSPR [IV]. Since the structure (or material) is now on a nanoscale, this method can be abbreviated, QnSPR (quantitative nano-structure-property relationship), where the fact that the model is using descriptors of nano-

structured heterogenous material is referred to by the corresponding prefix abbreviation. Other research groups have introduced alternative abbreviation conventions, such as nano-QSAR [129] and QNAR [130].

#### **1.4.1 *In silico* models for nanomaterials**

QnSPR of nanomaterials have been derived mainly for metals and metal oxides, while less attention has been paid to carbon-based materials [131]. Of the carbon-based materials, fullerene and its analogs have received the most attention, mainly for the derivation of QSPRs for solubility [132]. One recent example is an application of norm indexes to model solubility of fullerenes in various organic solvents [133]. In all these studies, the nanostructure is not directly described, but the properties of nanocompound are modeled through the structure of organic solvent, which is presented using conventional molecular descriptors. There are also examples in the literature where fullerene nanostructures are used to calculate theoretical molecular descriptors to model solubility and some other properties. Thus, QnSPR models have been derived for fullerenes with poly-aromatic hydrocarbons for solubility in 1-octanol and n-heptane [134] as well as for polarizability [135]. In addition to solubility, another widely modelled property of carbon nanomaterials is the adsorption of small organic molecules on the carbon surface. For example Metivier-Pignon *et al.* studied the mechanism of adsorption of dyes on activated carbon materials via deriving QnSPR models [136] and they noted that the small size of the database limits predictive ability. More recent articles present the modeling of adsorption of aromatic compounds [137], agrochemicals [138] and organic contaminants [139] on carbon nanotubes (CNT). In addition to adsorption, the dispersion ability of single-walled CNTs in different organic solvents has also been modelled [140]. Nanostructure description with molecular descriptors is developing field in QnSPR. Gonzales-Durruthy and co-workers found that Raman spectra are valuable source of structural information to be used for model development; they proposed star graph (SG) transformation of the CNT Raman spectra to obtain structural information and used these descriptors in development of QnSPR to study the effect of CNT on mitochondrial respiration [141]. Numerous recent works have presented a potential of the QnSPR method and pointed out the need to use such methods, for example in the field of nanotoxicology [142], but the major problem is the limited availability of high-quality datasets [116, 136, 143–145]. Therefore, all developments in QnSPR methods for nanomaterials are currently of great interest, especially those defining novel structural descriptors for nanostructured carbon, including nanoporous carbon.

#### **1.4.2 Structure-property relationships for the EDL carbon**

Nanoporous carbon is often used as an electrode material in electrical double-layer (EDL) capacitors due to large specific surface area and good electrical

conductivity. The EDL capacitance of a carbon electrode is related to the corresponding carbon pore size distribution [146–148] and generally the capacitance increases with increasing specific surface area (SSA). The last fact is also well visible from the modified relationship for the parallel plate capacitor, where to increase the charge stored, it is necessary to increase the accessible carbon surface area or use the smaller ions in the electrolyte:

$$C = \frac{A\varepsilon}{4\pi d}, \quad (13)$$

where  $\varepsilon$  is the dielectric constant of the medium between ion and carbon surface,  $A$  is the surface area of the porous electrode accessible to ions and  $d$  is a distance between the center of the ion and carbon surface [5, 149].

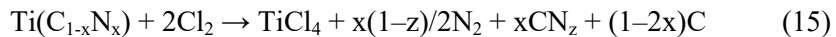
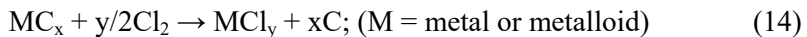
However, the relationship between capacitance and surface area is not trivial. It has been shown that, at the SSA values above  $\sim 1400 \text{ m}^2\text{g}^{-1}$ , the capacitance does not increase linearly and, therefore, using the materials with very high SSA does not lead to the expected increase in capacitance [146, 150]. This is partly due to the incomplete description of the accessible surface area. For example, the BET surface area, which is the most common characteristic of porous carbon, underestimates the SSA for pores smaller than 0.8 nm and overestimates them for pores larger than 1.1 nm. Therefore, the use of BET surface areas can lead to misinterpretation of the effects of SSA [151].

One-parameter relationships on SSA do not give sufficiently accurate results, so matching the pore sizes of carbon to the sizes of electrolyte ions provides better solution for optimizing the carbon texture and developing high-capacitance carbon materials [7]. Our pioneering study showed that experimentally measured porosity parameters from  $\text{N}_2$  adsorption make it possible to derive a three-parameter MLR model, giving a reasonable estimate ( $R^2 = 0.94$ ) for the volumetric capacitance of carbon electrode in a non-aqueous electrolyte, when combining in one equation the pore size characteristic, SSA and electrode packing density [IV]. Even more accurate three-parameter model for describing EDL capacitance ( $R^2 = 0.95$ ) was obtained, when the pore characteristics of sub-nanometer-sized pores from  $\text{CO}_2$  adsorption, using DFT based data reduction methods, were included [V]. The research in this direction has received momentum and Heimböckel *et al.* [152] have presented a combined model for micro- and mesoporous activated carbon material to show relationship between capacitance and pore sizes. They showed that it is possible to imitate the gravimetric capacitance using data derived from the  $\text{CO}_2$  and  $\text{N}_2$  adsorption. Very recently machine learning methods have been used to describe the EDL capacitance [153] and solvents effects on capacitance [154]. Zhou *et al.* [153] showed that ANN gives the best reproduction of the capacitance relationship on micropore and mesopore SSA over a wide range of the scan rates. That allowed constructing a Ragone plot that predicts the desirable features of activated carbons leading to the highest energy and power density.

## 2 MATERIALS AND METHODS

### 2.1 Synthesis of CDC

The presented QnSPR research involves approximately 200 different CDC-type carbon materials [IV, V], which were synthesized by chlorination (Eqs. 14 and 15) under various reaction conditions (chlorination temperature and time) from different precursors, including commercially available metal carbides (TiC, SiC, B<sub>4</sub>C, NbC, ZrC, Mo<sub>2</sub>C, Al<sub>4</sub>C<sub>3</sub>) and carbonitrides (TiC<sub>1-x</sub>N<sub>x</sub>). Variable non-stoichiometric titanium carbides (TiC<sub>x<1</sub>) used for synthesis of CDCs were prepared in SIAC (St.-Petersburg) [47].



The rules for the synthesis of CDC materials are described in details in the following references [29, 33, 35]. In short, the metal carbide powder was placed in a horizontal tubular quartz reactor and was treated with chlorine gas (AGA, 2.8) at chosen reaction temperature until complete conversion of carbide into CDC. The progress of the chlorination process was monitored through the acidic reaction of metal chloride produced. After that the reactor was flushed with argon (AGA, 4.0) at 1000°C to remove the excess of chlorine and the residues of gaseous by-products from carbon. Finally, the CDC powder produced was dechlorinated with hydrogen (AGA, 4.0) at 800°C.

To have CDC materials with hierarchical pore size distribution, the synthesis was carried out according to following two schemas: 1) *in situ* etching of CDC with TiO<sub>2</sub> additive (*e.g.*, 10–20 wt. %) mixed with metal carbide prior chlorination [155]; and 2) post-activation of CDC for moderately increasing the pores, using the etching of carbon at high-temperature (900 °C) with water previously absorbed into micropores [156].

For studying the catalyst effects on the structure of CDC [I] and for making the partially graphitized porous CDC for QnSPR study, the SiC was thoroughly mixed with graphitization catalyst (a mixture of CoCl<sub>2</sub>, NiCl<sub>2</sub> and FeCl<sub>3</sub> in ethanol). The SiC/catalyst composite was thereafter placed in a quartz boat and was reacted with a flow of chlorine gas (AGA, 2.8) in a horizontal quartz tube at a fixed temperature. After chlorination the product was additionally treated with hydrogen at 800°C to dechlorinate the sample.

Physical post-activation [II] of carbon materials was performed in tubular horizontal quartz reactor. CDC powder loaded into the reactor was flushed with argon to remove air and the furnace was heated up to 800 °C. Then the CDC was preliminary purified in hydrogen gas (AGA, 4.0) for 0.5 hours, after that the temperature was raised to 900 °C. The argon flow was then passed with a flow rate of 1.5 l/min through distilled water heated up to 75-80 °C and the resultant argon/water vapor mixture was let to interact with a carbon at 900 °C

for the predetermined time (30 or 45 minutes). After that, the reactor was flushed again with argon for 30 more minutes at 900 °C to complete the activation of a carbon surface and then slowly cooled to room temperature in argon atmosphere. The weight loss of post-activated CDC in the case of 30-minutes activation is within 16-31% and in the case of 45-minutes activation within 25–48%. The higher the synthesis temperature of CDC, the smaller the weight loss is observed.

Biomorphic carbon [III] was prepared by chlorinating of titanium carbide made from a mixture of charcoal and titanium dioxide by a carbothermic reaction. The BBQ-charcoal from deciduous wood (Põrgupõhja, Estonia) was sieved to a grain size of <0.5 mm and mixed with titanium oxide composite powder (Kemira RDD, 83% TiO<sub>2</sub>, <1 μm) in isopropanol (Aldrich, 99.5%). After desiccation, the mixture was loaded in the horizontal graphite-core reactor and heated at 1600°C for an hour. Thereafter, the wTiC powder was moved in horizontal tubular quartz reactor and treated with chlorine gas (AGA, 2.8) at 800°C for 120 min. After chlorination the reactor was flushed with argon (AGA, 4.0) at 1000°C for 1 h to remove the excess chlorine and the residues of gaseous by-products. Finally, the CDC powder produced was treated with hydrogen (AGA, 4.0,) at 800°C to result the crude product. For the removal of unwanted impurities, which resulted from the wood-derived material (*e.g.*, calcium and chlorine compounds [157]), the crude product was washed repeatedly with hot distilled water. The efficiency of washing was monitored by the pH of rinse water, which after the first washing was slightly basic (pH ~8.2) but changed to neutral (pH ~6.7) by the end of fourth washing. During the whole washing procedure, the carbon sample lost almost 12% of its weight. The liquid ion-chromatography of rinse water confirmed Ca<sup>2+</sup> and Cl<sup>-</sup> ions as the main impurities washed out. Also, the traces of Na<sup>+</sup>, K<sup>+</sup> and F<sup>-</sup> were detected, which is to be expected for the wood-derived material. The X-ray fluorescence spectroscopy (XRF) analysis of purified bio-CDC indicates that most of Ca<sup>2+</sup> and Cl<sup>-</sup> can be removed by careful washing.

## 2.2 Texture characterization of CDC

Porosity characteristics of carbon samples were determined from N<sub>2</sub> and CO<sub>2</sub> adsorption at 77K and 273K, respectively, using the NOVAtouch LX2 (Quantachrome Instruments) [II, III, V] or Gemini 2375 (Micromeritics) [I, IV]. Before measurements, the samples were dried in vacuum at 300°C. The BET surface area ( $S_{\text{BET}}$ ) of carbon samples was calculated from N<sub>2</sub> adsorption according to the BET theory [87] in the  $P/P_0$  interval of 0.02–0.2. The total volume of pores  $V_t$  was calculated at close to saturation pressure  $P/P_0 = 0.95$  [IV] or  $P/P_0 = 0.97$  [I, II, III, V]. The pore size distribution (PSD) and specific surface areas ( $S_{\text{dff}}$ ) were [II, III, V] calculated from N<sub>2</sub> isotherms using a quenched solid density functional theory (QSDFT) equilibria model for slit type pores [81, 84, 90]. The slit-geometry is the one that is most often recommended for nanoporous carbon

[1, 90]. The PSD for sub-nanometer-size [II, III, V] pores was calculated from CO<sub>2</sub> adsorption using a non-local density functional theory (NLDFT) model for slit-type pores [81, 84]. In Paper [IV], the PSD was calculated according to the BJH method [95]. Different pore size fractions were calculated from the cumulative PSD data.

## 2.3 Capacitance measurements

Carbon electrodes were made by pressing the slurry of CDC and PTFE (Aldrich, 60% dispersion in water) into the carbon sheet. The bulk density of electrodes was calculated as  $D_{el} = S_{el} \cdot h/m$ , where  $S_{el}$  is the visible surface area,  $h$  is the thickness, and  $m$  is the weight of the electrode. In the case of three-electrode cells, the reference and counter electrodes were made from high-surface area carbon film, coated on one side with 2 μm layer of pure Al [158]. Carbon electrodes and separators used were dried under vacuum prior to the assembly of the cells. After assembling, the cells were vacuumed and filled with non-aqueous electrolyte (details can be found in Papers [II-V]). The Potentiostat-Galvanostat 1286 Solartron was used for all electrochemical measurements.

The electrochemical characteristics of carbon materials at positive and negative polarization were measured in three-electrode test-cell using cyclic voltammetry (CV) and galvanostatic, *i.e.* constant current (CC) methods [5]. The integral capacitance ( $C_i$ ) was calculated from CC according to the equation:

$$C_i^+, (C_i^-) = \frac{i\Delta t \cdot S_{WE}}{E_{max} - E_{min}}, \quad (16)$$

where  $i$  is discharge current density,  $S_{WE}$  is the visible surface area of the working electrode and  $\Delta t$  is the discharge time in the potential range of  $E_{max}$  to  $E_{min}$ .

The differential capacitance ( $C_d$ ) values were calculated from CV plots, according to equation:

$$C_d^+, (C_d^-) = \frac{I^+, (I^-)}{g}, \quad (17)$$

where  $C_d^+$  is positively charged electrode capacitance (anodic capacitance),  $C_d^-$  is negatively charged electrode capacitance (cathodic capacitance),  $I^+$  and  $I^-$  are current values at fixed electrode potential. All current values were taken from the third CV discharge cycles. Specific capacitance values of CDC ((F g<sup>-1</sup>), (F cm<sup>-3</sup>)) were calculated as  $C_{CC} = C_i/m$  and  $C_{CC} = C_i/V$  (or  $C_{CV} = C_d/m$ ,  $C_{CV} = C_d/V$ ), where  $m$  is the weight of the CDC in the working electrode and  $V$  is the volume of the working electrode.

The cathodic and anodic capacitances of CDCs in 1M triethylmethylammonium tetrafluoroborate ((C<sub>2</sub>H<sub>5</sub>)<sub>3</sub>CH<sub>3</sub>NBF<sub>4</sub>, Stella, H<sub>2</sub>O<0.005%) solution in propylene carbonate (PC, anhydrous, Merck Selectipur) were calculated at

5 mAcm<sup>-2</sup> from the constant current discharge experiments at the potential range of 0 to -1.4 V and 0 to +1.4 V, respectively [IV]. Before discharge the materials were kept at constant voltages for 3 minutes to achieve the equilibrium condition. Examples of CC discharge curves of two CDC samples are presented in Figure 4a.

In the electrolyte of 1.5 M SBP-BF<sub>4</sub> in acetonitrile (KKE-15-TAN, Japan Carlit Co., Ltd; H<sub>2</sub>O < 30ppm), the capacitance of CDCs at positive (0 to +1.2 V) and negative (0 to -1.2 V) polarization potentials was determined with two methods [V]: constant current discharge at 0.5 mA cm<sup>-2</sup>, and cyclic voltammetry at fixed potential +0.7 V or -0.5 V using voltage scan rate  $\nu = 2 \text{ mV s}^{-1}$ . The capacitance values,  $C_{CV}$  and  $C_{CC}$ , from cyclic voltammetry and galvanostatic cycling, respectively, are in very good correlation with each other, especially for cathodic capacitance ( $R^2 = 0.99$ ). In QnSPR analysis, the  $C_{CV}$  values were used because of simplicity [5, 159, 160]. Figure 4b exemplifies CV curves of two CDC samples.

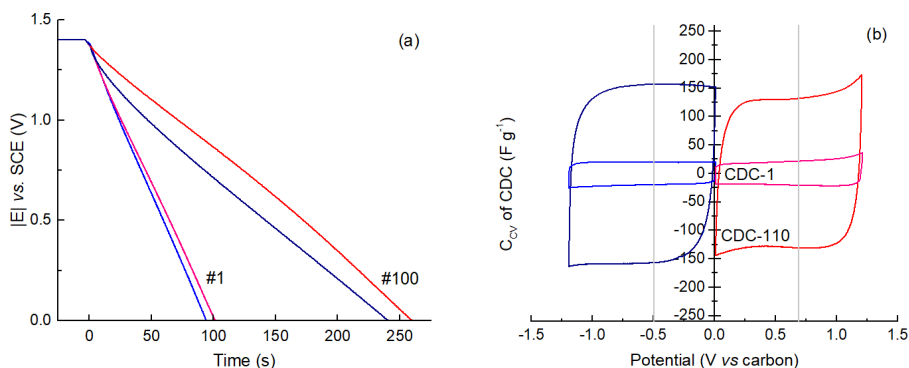


**Figure 4.** Constant current discharge potential profiles (at 5mAcm<sup>-2</sup>) of samples 1 and 100 (a), and cyclic voltammetry curves ( $\nu = 2 \text{ mV s}^{-1}$ ) expressed as gravimetric capacitance for CDC-1 and CDC-110 (b), wherein the fixed potential values for  $C_{CV}$  readings are shown by vertical lines at -0.5 and +0.7 V.

## 2.4 Quantitative nano-structure-property relationships

The EDL capacitance was modelled with experiment-derived structure descriptors encoding CDC surface area, porosity, and electrode packing. The response variable was modelled by a linear combination of descriptor variables (see refs. [122, 123]):

$$y_i = \beta_0 + \beta_1 x_{i1} + \dots + \beta_k x_{ik} + \varepsilon_i, \quad (18)$$

where  $x_{i1}, \dots, x_{ik}$  are descriptors and  $\beta_0, \dots, \beta_k$  are respective coefficients, and  $\varepsilon_i$  are the model errors. Besides estimating the coefficients, also the model scale

parameter (standard deviation of the response variable)  $\sigma$  is to be estimated. The descriptor variables for modelling were: various pore size fractions,  $V_{N_2,CO_2[x-y]}$  (where  $x$  and  $y$  are the lowest and highest pore sizes of the fraction), calculated according BJH or DFT; SSA by BET ( $S_{BET}$ ) or DFT ( $S_{dft}$ ); total pore volume ( $V_t$ ), micropore volumes by  $t$ -plot ( $V_\mu$ ) or DFT ( $V_{\mu,dft}$ ); the average pore size ( $APS = 2V_t/S_{dft}$ ); and the electrode-related descriptor – bulk density ( $D_{el}$ ) to describe the packing conditions of carbon particles in the electrode.

QnSPR models for the volumetric cathodic capacitance of carbon in TEMA-BF<sub>4</sub>/PC electrolyte [IV] were developed using BMLR method. BMLR, performed using CODESSA program [161], follows a stepwise forward algorithm to select significant descriptors while building a multiple linear model. During the BMLR procedure, the nonsignificant descriptors ( $R^2 < 0.1$ ) were excluded, and the noncollinearity criteria  $R^2 < 0.7$  was applied to the descriptors selected. The final model has the best representation of the property in the given descriptor pool within the given number of parameters [121]. The quality of the models was assessed by the square of coefficient of determination ( $R^2$ ), the square of cross-validated (leave-one-out) coefficient of determination ( $R^2_{CV}$ ), the square of standard error of the estimate ( $s^2$ ), and the Fisher's criterion (F) [117].

QnSPR models for gravimetric and volumetric cathodic capacitances of carbon in SBP-BF<sub>4</sub>/ACN electrolyte [V] were developed using R statistical computing language [122, 162]. Significance level for all parameters was chosen to be 0.05, so that all the coefficients of remaining descriptors in the model have  $p$ -value less than 0.05. Akaike Information Criterion (AIC) and the coefficient of determination ( $R^2$ ) were used to determine, which descriptor to leave out next (in case of top-down method) or include next (in case of bottom-up method). Also, because several descriptors were highly correlated, variance inflation factor ( $VIF$ ) was calculated and the descriptors with  $VIF > 5$  were omitted. High  $VIF$  value means that all other descriptors quite well explain the variability of given descriptor [123].

For models diagnostics, the outliers, high leverage points and influential points were analyzed [122]. The model diagnostics are summarized in the influence plot (also called the Williams plot), where vertical axis shows the standardized residuals  $r_i$ , horizontal axis shows the leverage (hat values)  $h_i$  of each material and the circle radii show the influence of the points (measured by Cook's distance) [128].

## 3 RESULTS AND DISCUSSION

### 3.1 Synthesis and modification of CDC nanostructure

There are four main strategies to influence the CDC-type carbon structure: 1) choosing the appropriate starting carbide, 2) varying the synthesis temperature, 3) using catalytic additives during CDC formation [I], and 4) post-activation [II]. All of these strategies have found a combined use in the synthesis of more than 200 different carbon samples in this study [IV, V]. The CDC materials with variable nanostructure and pore size distributions were made by the chlorination of ten different metal carbides or carbide-like precursors (Eqs. 14 and 15 in previous sections) at the temperatures between 400°C and 1100°C.

As already discussed above, the structural order and porosity of CDC are strongly related to the synthesis temperature; the higher the temperature, the higher degree of graphitisation. In Figure 5a, one can see that the N<sub>2</sub> adsorption isotherms, for TiC-derived CDCs synthesized at lower temperatures, correspond to Type I(a), which is the characteristic of microporous materials, and in the case of higher synthesis temperature, the shape of the isotherm refers to a wider pore size distribution. In addition, the total porosity of TiC-derived CDC differs by ~1.5-fold at synthesis temperatures of 500 and 1000°C. Even more structural variation is achieved for Mo<sub>2</sub>C-derived carbons in the same chlorination temperature interval (Figure 5c). A noticeable hysteresis loop observed for Mo<sub>2</sub>C-derived materials at chlorination temperatures above 600°C, indicates a partial graphitization and the presence of mesopores. The temperature range actually used for chlorination varies for different carbides, for example, SiC and B<sub>4</sub>C achieve a complete conversion to CDC at much higher temperatures than most metal carbides, which creates less scope for influencing the CDC structure (cf. Figure 5b).

Different starting carbides result in distinct distributions of pore-sizes in carbon due to different chemical nature and location of the carbon atoms in the initial metal carbide. Results for PSDs for CDC materials synthesized from different carbides at 600°C and 1000°C (Figures 6a and 6b) show that CDC with a narrow pore size distribution in the range of micropores should be made from silicon or titanium carbide, a wider micropore size distribution is more easily achieved with NbC or ZrC. Mo<sub>2</sub>C or B<sub>4</sub>C can be used if more advanced mesoporosity is required. Materials synthesized from Mo<sub>2</sub>C at lower temperatures (<600°C) produce Type I isotherms (Figure 5c) and materials synthesized at higher temperatures are characterized by Type IV isotherms with H4-type hysteresis loop, caused by capillary condensation in mesopores. While in the case of TiC (cf. Figure 5a), the SSA increases from 1127 to 1569 m<sup>2</sup>g<sup>-1</sup> proportionally with the synthesis temperature (within the interval of 500 to 1000°C), then with Mo<sub>2</sub>C-derived carbon (cf. Figure 5c), the SSA gains the highest value with synthesis temperature of 800°C (~ 1951 m<sup>2</sup>g<sup>-1</sup>). At higher temperatures, the SSA starts to decrease due to the development of mesoporosity, and drops to the value of 1052 m<sup>2</sup>g<sup>-1</sup> at 1000°C. As one can see in Figure

6b, CDC synthesized from  $\text{Mo}_2\text{C}$  at  $1000^\circ\text{C}$  is mesoporous with low microporosity. These results confirm that varying and combining of precursor carbides and the synthesis temperature can result in CDCs with a very wide variety of PSDs.

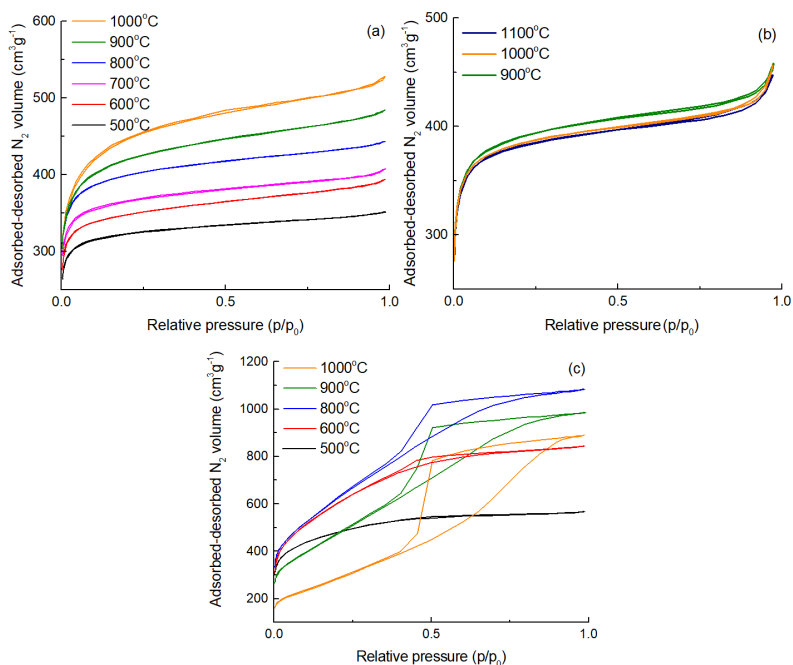


**Figure 5.** Nitrogen adsorption isotherms of CDC materials synthesized from TiC (a), SiC (b) and  $\text{Mo}_2\text{C}$  (c).

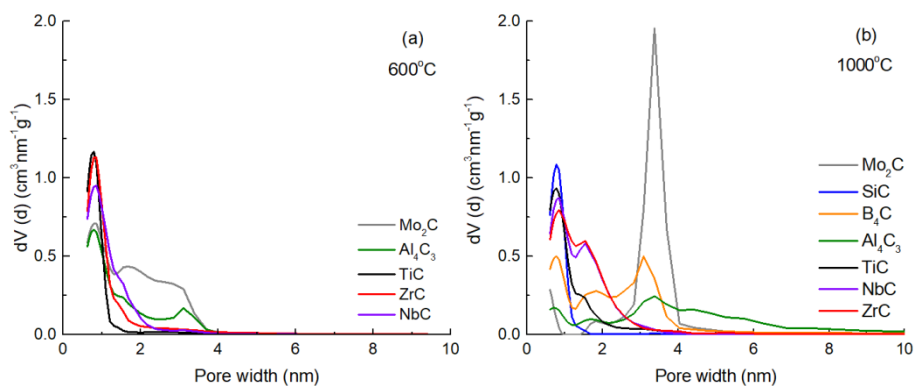


**Figure 6.** Differential PSD calculated by QSDFT method from  $\text{N}_2$  adsorption of CDC materials synthesized from different precursor carbides at  $600^\circ\text{C}$  (a) and  $1000^\circ\text{C}$  (b).

### 3.1.1 Effects of graphitization catalysts on pore size distribution

Systematic study performed on catalyst-supported chlorination of  $\alpha$ -SiC [I] confirms the earlier findings on the catalytically influenced TiC- and  $Al_4C_3$ -derived carbons [30, 35] and shows that the structure and the PSD of CDCs can be well tuned by using a Ni–Co–Fe catalyst while changing the chlorination temperature. Applying different temperatures and amounts of catalyst, the SiC-derived CDC has a change in  $S_{BET}$  of approximately 1000 units ( $\sim 300 - \sim 1360 \text{ m}^2 \text{ g}^{-1}$ ). The adsorption isotherms of CDC materials synthesized at  $1100^\circ\text{C}$  (see Figure 7a) demonstrate that increasing of the concentration of catalysts in reaction medium decreases the relative amount of micropores and increases the amount of mesopores. Without catalyst or with only small amount of catalyst the  $N_2$  adsorption isotherms of CDC belong to Type I, as characteristic of microporous materials. The isotherms at increased catalyst concentration belong also to microporous material but confirming the wider pore-size distribution. The H4 loop in respective adsorption isotherms is seen at relative pressure between 0.4 and 0.5, as typical for partially graphitic carbon materials. The reduction in microporosity with increasing the catalyst concentration is clearly seen in Figure 7b, where the pore size distribution of CDC is presented. However, it has to be noted that the effect of catalysts on the formation of CDC from  $\alpha$ -SiC appears at significantly higher temperature than in the case of titanium and aluminium carbides [30, 35].

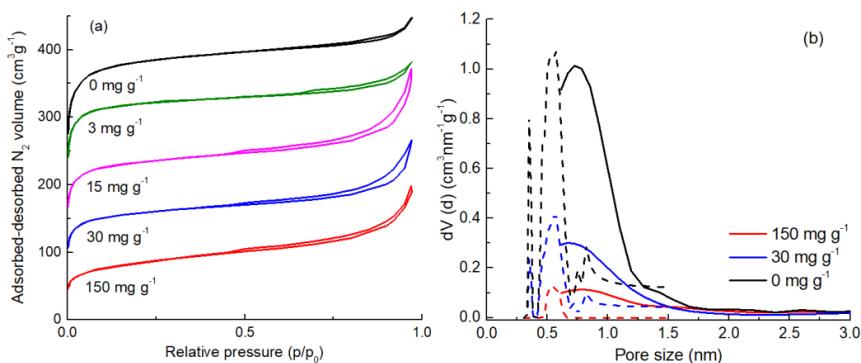


**Figure 7.**  $N_2$  adsorption isotherms for SiC-derived carbon at  $1100^\circ\text{C}$  for various amounts of catalyst (a) and PSD curves calculated from  $N_2$  (solid line) and  $CO_2$  (dashed line) adsorption isotherms (b) [I].

Thus, this study shows that the structural order and porosity of the SiC-derived CDC depend on both the catalyst concentration and the synthesis temperature. Consequently, the SSA and PSD of CDC materials can be controlled in a wide range by varying the amount of catalyst.

### 3.1.2 Steam-treated CDC

The effects of physical activation were studied systematically by varying the structural order and porosity of precursor CDCs [II]. More precisely, the set of TiC-derived CDCs, synthesized at 6 different temperatures in-between 500 and 1000°C, were post-activated by using high-temperature etching with water vapor (see (Eq. 19)).

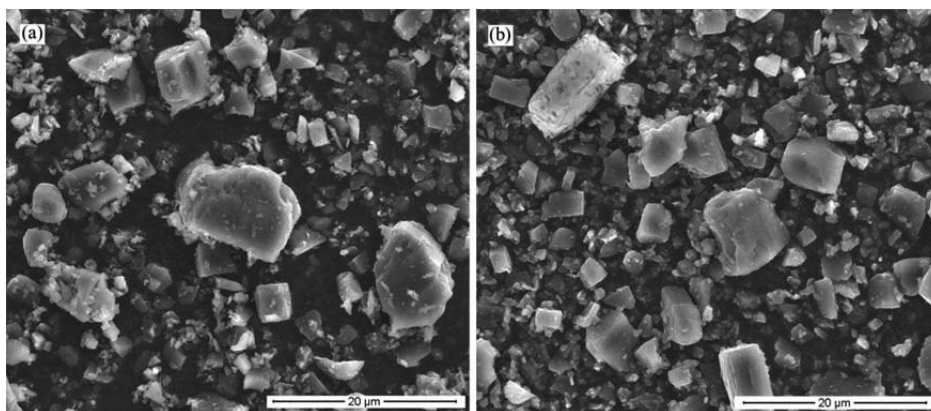
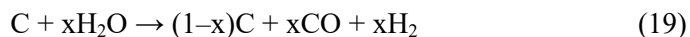


**Figure 8.** SEM images of non-activated (a) and post-activated (b) CDC synthesized at 500°C [II].

It was shown that both the initial structure of the CDC and the activation time are important for controlling the steam-treatment product. The weight loss of post-activated CDC is 16–31% for 30 minutes of activation and 25–48% for 45 minutes of activation and this depends on the initial structure of the CDC. The higher the synthesis temperature of CDC, the smaller the weight loss is observed. The oxygen content in the post-activated CDC stays almost at the same level as non-activated samples and increases slightly during activation from 4 to 6% (wt) according to XPS.

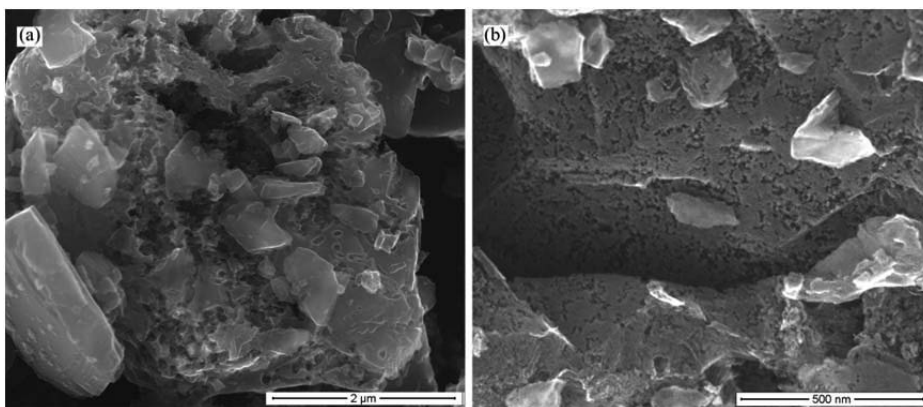


**Figure 9.** High-resolution SEM images of different magnifications (a, b) of post-activated CDC synthesized at 500°C [II].

SEM pictures show that etching by water vapour does not change the macroscopic structure of carbon powder (cf. Figure 8). Although, the carbon particles retain their initial size and shape during the activation, the etching impact is clearly seen on the surface of particles (see Figure 9). The worm-like surface morphology may be due to diffusion-restricted activation, leading to widespread etching on already destroyed and penetrated surfaces, which have easier access to active centers.

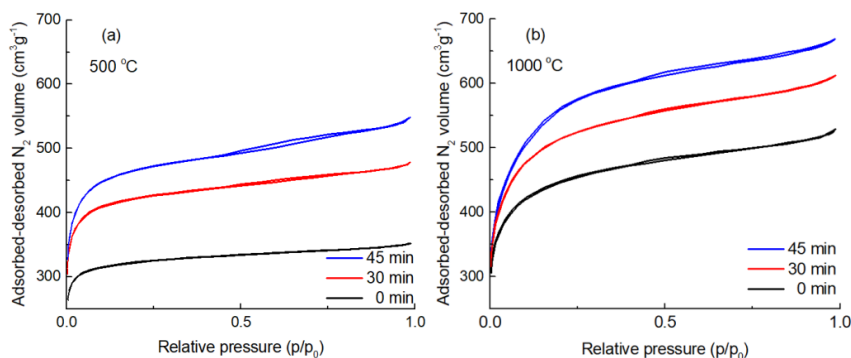


**Figure 10.** Low-temperature nitrogen adsorption isotherms of precursors (0 min) and activated (30 min and 45 min) CDCs synthesized at 500 (a) and 1000°C (b) [II].

Physical activation increases both the total pore volume and microporosity, as appears from nitrogen adsorption isotherms (Figure 10). Isotherms of non-activated CDCs appear as Type I by IUPAC [81], which is characteristic to microporous materials. Post-activated materials have the Type H4 hysteresis on

the desorption curve, which confirms the formation of mesopores during activation. Extending the activation time from 30 minutes to 45 minutes increases the total pore volume, but does not significantly change the shape of the isotherm. The surface area ( $S_{\text{BET}}$ ) of the CDC was controlled during the activation in the range of 1000–2000  $\text{m}^2\text{g}^{-1}$  (see Table 1).

**Table 1.** BET and DFT surface areas ( $S_{\text{BET}}$ ,  $S_{\text{dft}}$ ), total pore volumes ( $V_t$ ), volumes of micropores ( $V_\mu$ ) and average pore diameters (APS) of preceding and post-activated CDC materials.

Code of CDC*	$S_{\text{BET}}$ ( $\text{m}^2\text{g}^{-1}$ )	$S_{\text{dft}}$ ( $\text{m}^2\text{g}^{-1}$ )	$V_t$ ( $\text{cm}^3\text{g}^{-1}$ )	$V_\mu$ ( $\text{cm}^3\text{g}^{-1}$ )	APS (nm)
TiC500	1127	1289	0.54	0.51	0.84
TiC600	1210	1375	0.61	0.56	0.88
TiC700	1276	1429	0.62	0.58	0.87
TiC800	1394	1417	0.68	0.64	0.97
TiC900	1468	1534	0.75	0.68	0.97
TiC1000	1569	1569	0.81	0.73	1.03
TiC500-30	1473	1560	0.73	0.68	0.94
TiC600-30	1624	1679	0.79	0.73	0.94
TiC700-30	1809	1830	0.92	0.83	1.00
TiC800-30	1820	1790	0.96	0.86	1.07
TiC900-30	1957	1806	0.99	0.91	1.10
TiC1000-30	1818	1691	0.94	0.85	1.11
TiC500-45	1637	1639	0.84	0.76	1.02
TiC600-45	1753	1763	0.85	0.80	0.97
TiC700-45	1951	1838	0.96	0.87	1.04
TiC800-45	1914	1856	1.06	0.88	1.14
TiC900-45	1983	1874	1.00	0.91	1.07
TiC1000-45	1985	1756	1.03	0.93	1.17

\* A code indicates the precursor carbide, chlorination temperature in  $^\circ\text{C}$  (500–1000) and activation time in minutes (30 or 45) if post-activated.

The pore size distributions (PSD) were calculated from  $\text{N}_2$  and  $\text{CO}_2$  adsorption isotherms and are presented in Figure 11. The PSD of all samples tested contains peaks, which correspond to pores sizes of around 0.34, 0.55 and 0.8 nm. The volume of micropores increases during physical activation, most probably due to the etching of the original micropores, but also by opening the initially

“closed” pores. The greatest effect of the activation is observed for a CDC, synthesized at 500°C. For this low-temperature-derived carbon the steam treatment for 45 minutes leads to increase of total pore volume from 0.54 to 0.84 cm<sup>3</sup>g<sup>-1</sup>. In Figure 11a, one can see that the activation has particularly big impact to pores within sub-nanometer range. The activation increases the volume of 0.8 nm pores but decreases the volume of 0.34 nm pores. The PSD plots of more graphitic CDC, which were synthesised at higher temperatures, reveal noticeable changes also in the range of pore sizes over 1 nm.

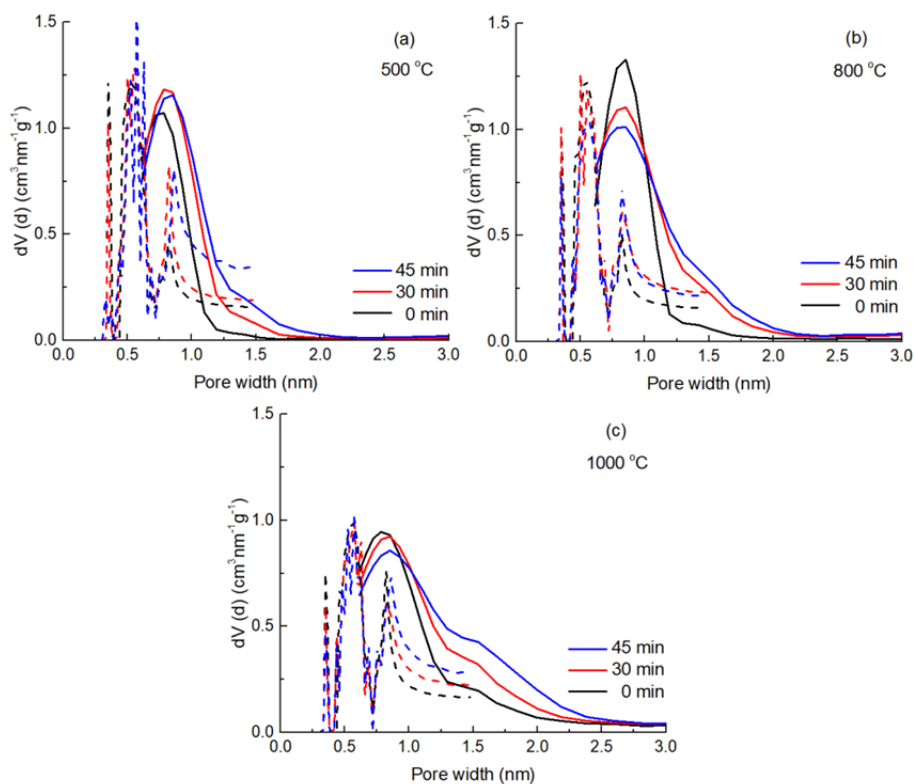


**Figure 11.** The pore size distribution curves of precursors (0 min) and activated (30 min and 45 min) CDCs calculated from  $\text{N}_2$  (solid line) and  $\text{CO}_2$  (dashed line) adsorption isotherms at different chlorination temperatures (a-c) [II].

In summary, the results confirm that the post-activation attacks first and foremost disordered carbon and in a lower degree influences carbon with the ordered structure. Therefore, by varying the initial CDCs for the post-activation treatment, it is possible to generate carbon materials with widely varying pore size distributions.

### 3.1.3 Biomorphic CDC

One way for enhancing the porous texture of CDC and improving the access to micropores is to use biomorphic precursor carbides with a cellular wood structure. This leads to the CDC-type carbon produced by chlorinating a carbothermal reduction product of a  $\text{TiO}_2$  composite and hardwood charcoal [III]. Here, the abbreviation bio-CDC is used to distinguish the biomorphic CDC (note that in Article III the wCDCp is used for the same).

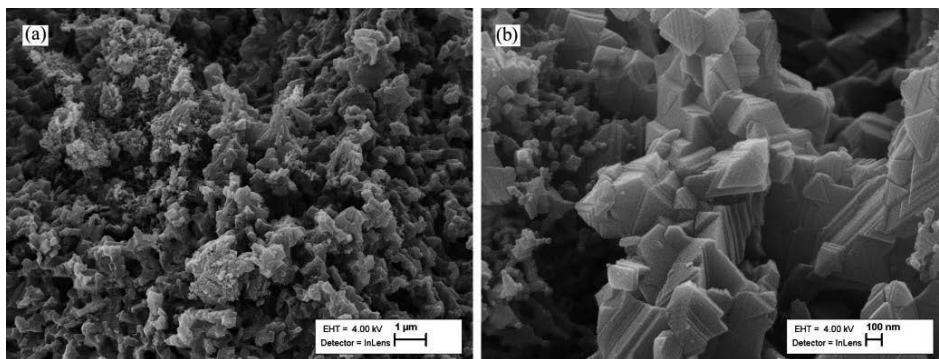


**Figure 12.** SEM images of different magnifications (a, b) of biomorphic CDC (bio-CDC) [III].

The SEM images (cf. Figure 12) of the bio-CDC show that the carbon is very porous and consists of fine intergrown particles. The macroscopic structure comprises of voids and macropores that originates from the cellular structure of precursor wood but partly can also be caused by volatile organic compounds released from incompletely pyrolyzed charcoal. The unique precursor carbide structure, which consists of submicrometer-sized crystals whose shape is also transmitted to the resulting bio-CDC, is due to the particle size of the  $\text{TiO}_2$  converted to carbide by carbothermal reduction.

The wood-origin bio-CDC has a remarkably higher surface area ( $S_{\text{BET}}$  2464 vs. 1562  $\text{m}^2\text{g}^{-1}$ ), and  $\sim 0.3$  nm higher APS value (1.27 vs. 0.96 nm) compared to common CDC made from commercial TiC powder at the same chlorination conditions. The  $\text{N}_2$  adsorption-desorption isotherms of both bio-CDC and common CDC, shown in Figure 13a, are typical Type I isotherms according to the IUPAC classification [81]. Yet, the common CDC shows Ia isotherm shape in opposite to the bio-CDC, which is characterized by Type Ib isotherm, showing that pore filling occurs over a wider range of relative pressures as inherent to microporous solids with a wider distribution of pore-sizes. The PSD plots, presented in Figure 13b, confirm that in the region of sub-nanometer sized micropores, the bio-CDC does not differ too much from the common TiC-derived CDC. Both have a large quantity of pores in between  $\sim 0.4$  and  $\sim 0.7$  nm,

however, the volume of pores at 0.4 nm is significantly smaller for the bio-CDC. The major difference from the common TiC-derived CDC is a wider pore-size distribution of the bio-CDC with a visible shoulder at around 1.6 nm. Similar shoulder appears in the PSD of post-activated CDC materials, which indicates that bio-CDC is most likely *in situ* activated/etched by the oxygen from biomorphic TiC.

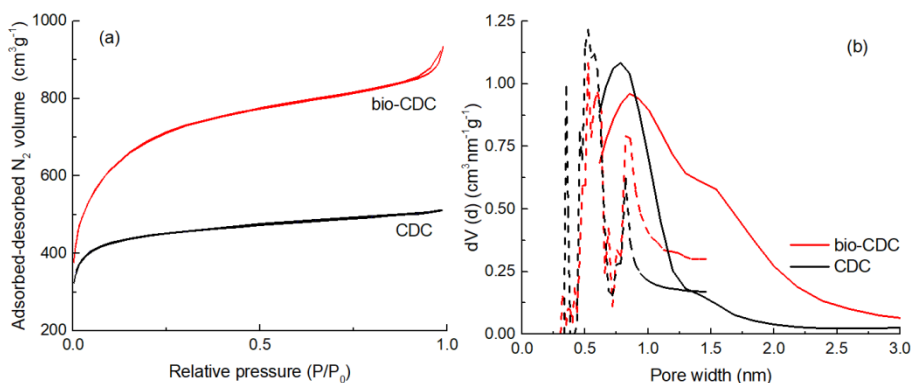


**Figure 13.** N<sub>2</sub> adsorption-desorption isotherms (a), and pore size distribution of biomorphic TiC-derived bio-CDC compared to common TiC-derived CDC calculated from N<sub>2</sub> (solid line) and CO<sub>2</sub> (dashed line) adsorption (b).

The oxygen content of bio-CDC according to EDX and XPS was 6% and 11%, respectively. Most of the oxygen is assumed to originate from mineral oxide impurities, the oxygen bearing functional groups also exist on carbon surface as confirmed by the FT-IR analysis. Modelling of the high-resolution scan of O1s region by XPS analysis confirms the occurrence of oxygen bearing functional groups such as carbonyl and ether-like oxygen groups, which dominate over quinonic and phenolic oxygen. A complete removal of surface oxygen can be achieved with hydrogen post-treatment at around 1000°C [163].

The study proved that carbothermal reduction of titanium dioxide-based white pigment and hardwood charcoal yields biomorphic titanium carbide as a suitable precursor for nanoporous CDC. Chlorination of this highly porous biomorphic carbide resulted in a bio-CDC with an accessible surface area ( $S_{\text{BET}}$ ) of  $\sim 2500 \text{ m}^2 \text{ g}^{-1}$ .

## 3.2 QnSPR of nanoporous CDC

### 3.2.1 TEMA-BF<sub>4</sub> electrolyte case

The QnSPR approach was used for the statistical analysis and modelling of the volumetric capacitance ( $C_V$ ) of 100 CDC materials against numerous porosity and pore size distribution-related characteristics as experiment-derived descriptors of carbon structure. The range of carbon materials, used in this study, reflects the high variability of nanoporous CDC [IV]: 53 samples were obtained from TiC, 14 samples from Mo<sub>2</sub>C, 19 samples from Al<sub>4</sub>C<sub>3</sub>, 10 samples from SiC and 4 samples were from B<sub>4</sub>C. Of this selection, 19 samples were treated *in situ* with TiO<sub>2</sub> during chlorination, 21 materials were synthesized using a chlorination protocol with two consecutive synthesis temperatures [164], and 53 materials were post-treated with H<sub>2</sub>O in micropores [156].

Capacitance values for all 100 CDC materials are shown in Figure 14. In a low-capacitance region, which is characterized by CDCs with a very low content of subnanometer-sized pores, the anodic and cathodic capacitances are almost equal. At higher capacitance values, the difference between the anodic and cathodic capacitances increases significantly. This phenomenon can be explained by the compatibility of pore sizes and electrolyte ions. Since tetrafluoroborate (BF<sub>4</sub><sup>-</sup>) anions are smaller than triethylmethylammonium ((C<sub>2</sub>H<sub>5</sub>)<sub>3</sub>CH<sub>3</sub>N<sup>+</sup>) cations, approximately 0.46 nm vs. 0.65 nm, respectively [160], the anodic capacitance exceeds the cathodic one, when pore-size becomes the limiting factor in nanoporous carbon electrodes.

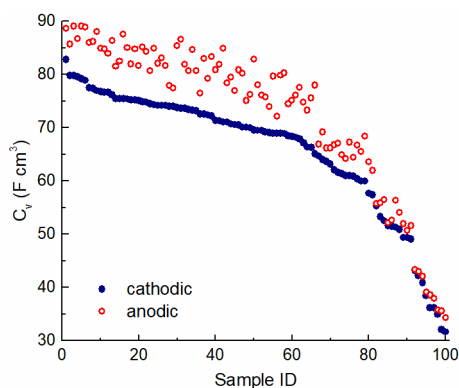


**Figure 14.** Values of anodic (red) and cathodic (blue) volumetric capacitance of a set of 100 CDC materials.

Examining the one-parameter relationships between the capacitance and common porosity characteristics of CDCs reveals that no correlation can be found between capacitance and SSA, while the clear trend exists for the volumes of

micropores ( $V_{\mu}$ ) (see Figure 15). This result supports a number of earlier observations that the increase in SSA does not assure the increase in capacitance [146, 147, 150] if the morphology of the surface is inappropriate for the electro-sorption of ions. Assuming that suitable surface morphology is connected to the size and geometry of the pores, the proper combination of specific surface area and pore size distribution may result in reasonable predictions for the capacitance of high-surface carbon materials.

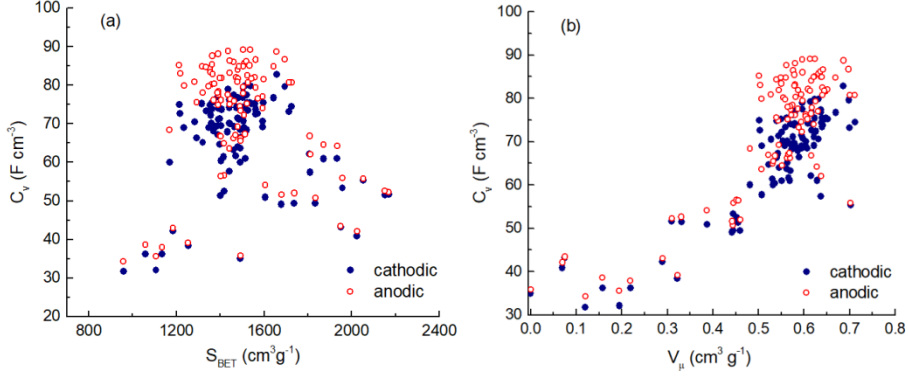


**Figure 15.** Correlations of  $C_V$  vs.  $S_{\text{BET}}$  (a) and  $C_V$  vs.  $V_{\mu}$  (b) for 100 CDCs.

The BMLR analysis resulted in the optimal *in silico* model that has best representation of the property for the given set of descriptors. The three-descriptor model (Eq. 20) developed for the cathodic EDL capacitance includes the BET surface area of carbon powder ( $S_{\text{BET}}$ ), the volume fraction of the pores with the size of less than 1.14 nm ( $V_{d<1.14}$ ) and the bulk density of the carbon electrode film ( $D_{\text{el}}$ ). The correlation between predicted and experimentally measured capacitance values, characterized by  $R^2=0.94$  and  $s^2=8.7$ , is visualized in Figure 16a.

$$C_{V,\text{NEG}} = -11.1 + 0.0184 \cdot S_{\text{BET}} + 72.3 \cdot V_{d<1.14} + 39.6 \cdot D_{\text{el}} \quad (20)$$

The third descriptor in the model (Eq. 20),  $D_{\text{el}}$ , gives to the equation the volumetric dimension.  $D_{\text{el}}$  also takes into account the packing density of the carbon particles; thereby adding an indirect description of the interactions between the carbon particles to the QnSPR model.

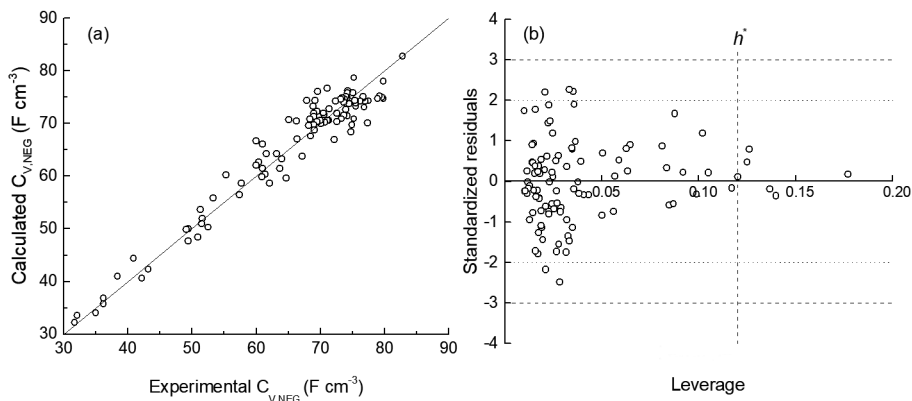


**Figure 16.** Experimental  $C_{V,NEG}$  vs. QnSPR calculated  $C_{V,NEG}$  for 100 CDC obtained with BMLR (a), and corresponding influence plot (b) [IV].

As it can be seen from the Eq. 20, there is a positive correlation with volumetric capacitance for all descriptors. This means that as the volume of pores smaller than 1.14 nm ( $V_{d<1.14}$ ) increases, the cathodic capacitance also increases. The same applies to the BET surface area of carbon powder ( $S_{BET}$ ) and the bulk density of the carbon electrode film ( $D_{el}$ ).

The model diagnostics are summarized in the influence plot (Figure 16b), where residuals analysis (on vertical axis) shows five moderate outliers and five data points have higher hat-values (leverage) than critical value, but still very close to the threshold line. The outliers and the samples with higher leverage value mostly are related to the materials with larger pores (like partly mesoporous CDC). Apparently, such carbons are poorly described by the given three-descriptors QnSPR model, which may be caused by limitations of the  $S_{BET}$  descriptor.

The reliability of the model for the prediction of volumetric EDL capacitance of porous carbon was verified via external validation. For this the dataset was divided into training and external validation sets. The training set consisted of 53 carbon materials, which had been post-treated using  $H_2O$ -activation, and 47 materials, that had not been post-treated, composed the validation set. The descriptors that worked out for the training set are exactly the same as used for the full set analysis and the best three-descriptors multiple linear regression model derived with BMLR for  $C_{V,NEG}$  of training set is characterized by  $R^2$  of 0.94 (Figure 17). This result particularly confirms that there is no need for additional descriptors in the QnSPR model for describing the changes in surface chemistry due the possible oxidation of carbon during gas-activation.

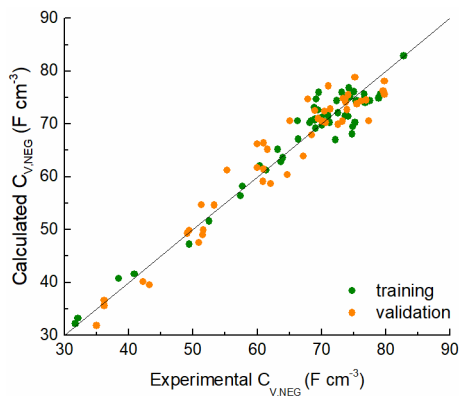


**Figure 17.** Correlations between experimental and QnSPR calculated  $C_{V,NEG}$  values according to BLMR of the training-set (53 structures) and validation set (47 structures) [IV].

Most importantly, the current QnSPR model shows that when the structure of nanoporous carbon material is well quantified and the data set systematically covers that structural variation, the *in silico* model derived allows mechanistically justified explanation on the level of physico-chemical phenomenon. In general terms, this work reveals that the experimental adsorption-based characteristics describing the structure of nanoporous carbon material can be successfully used in QnSPR models. The model and data are available at QsarDB repository (<http://dx.doi.org/10.15152/QDB.205>).

### 3.2.2 SBP-BF<sub>4</sub> electrolyte case

In order to model the relationship between EDL capacitance and CDC nanostructure for SBP-BF<sub>4</sub> electrolyte, 110 CDCs of different structure and pore sizes prepared from ten different metal carbides at different synthesis temperatures (see Figure 18a), were compiled into one dataset [V]. The overall variability of carbon samples is characterized by the range of  $S_{BET}$  values of 325–2464 m<sup>2</sup>g<sup>-1</sup> and  $S_{dff}$  values of 303–2094 m<sup>2</sup>g<sup>-1</sup>, total pore volume of 0.29–1.87 cm<sup>3</sup>g<sup>-1</sup> and a ratio of micropore volume to total pore volume of 0.09–0.89. Average pore sizes ( $APS = 2V_i/S_{dff}$ ) remain within the range of 0.8–3.6 nm. The carbon materials are numbered from CDC-1 to CDC-110 in ascending order of the cathodic capacitance in SBP-BF<sub>4</sub>/ACN electrolyte. As one can see in Figure 18b, in SBP-BF<sub>4</sub> based electrolyte, the capacitances are comparable for both positively and negatively polarized electrodes (unlike to TEMA-BF<sub>4</sub> electrolyte in previous chapter, where the cathodic capacitance always had a lower value), wherein the values over the all carbon samples fall in-between 20 – 160 F g<sup>-1</sup>.

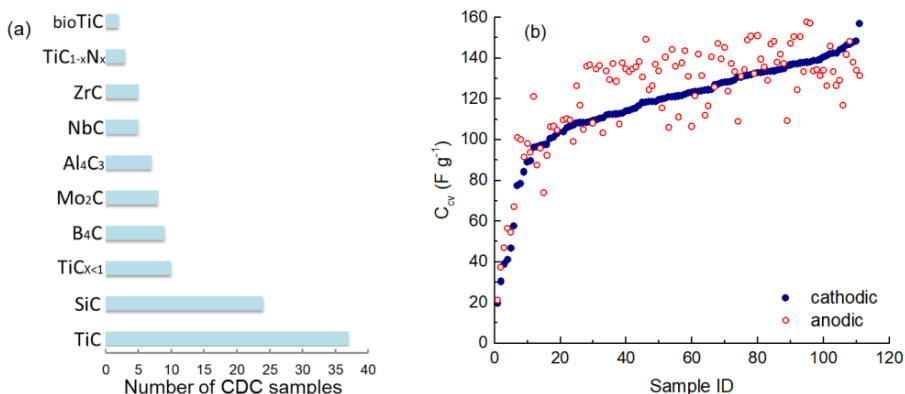


**Figure 18.** Metal carbides used as precursors for the set of 110 CDCs (a), and capacitance ( $C_{cv}$ ) of these CDC materials at positive (red) and negative (blue) polarization (b) in SBP- $BF_4/ACN$  electrolyte.

The reason for the competition between positive and negative capacities is probably due to the comparable dimensions of the electrolyte ions (0.46 nm vs. 0.42 nm for  $BF_4^-$  and  $SBP^+$ , respectively) [160, 165, 166]. Although the  $SBP^+$  cation takes up a slightly more volume than  $BF_4^-$  anion (0.114 nm<sup>3</sup> vs. 0.073 nm<sup>3</sup>) [167–169], considering its rigid “8” shape structure, one can assume that, in some cases, it fits better and allows faster ion transfer in micropores and, therefore, provides higher capacitance [166, 170, 171].

For obtaining the experiment-derived structure descriptors, the volumes of different pore size fractions of CDC samples were extracted from cumulative PSD patterns calculated by DFT from  $N_2$  and  $CO_2$  sorption data. Pore size fractions were defined in 0.1 nm increments also including the fractions with pore sizes up to a minimum threshold (0.8 nm and 0.4 nm for  $N_2$  and  $CO_2$ , respectively). Thus, from nitrogen adsorption measurements, the pore size fractions were calculated up to 5 nm, and from  $CO_2$  adsorption up to 1.2 nm for more precise characterizing of the sub-nanometer size pores.

From the pool of experiment-derived structure descriptors for MLR models were found stepwise using both top-down and bottom-up descriptor selection approaches, where AIC was used to determine, which descriptor to leave out or include next. Ultimately, the final model was chosen by considering AIC and  $R^2$ . The best model for cathodic gravimetric capacitance (Eq. 21) has  $R^2 = 0.91$  and estimated model scale parameter  $\hat{\sigma} = 7.38$ . The correlation between predicted and experimentally measured capacitance values is visualized in Figure 19a.

$$C_{CV,g}^- = -5.82 + 0.0582 \cdot S_{dft} + 212 \cdot V_{CO_2[0.4-0.7]} \quad (21)$$

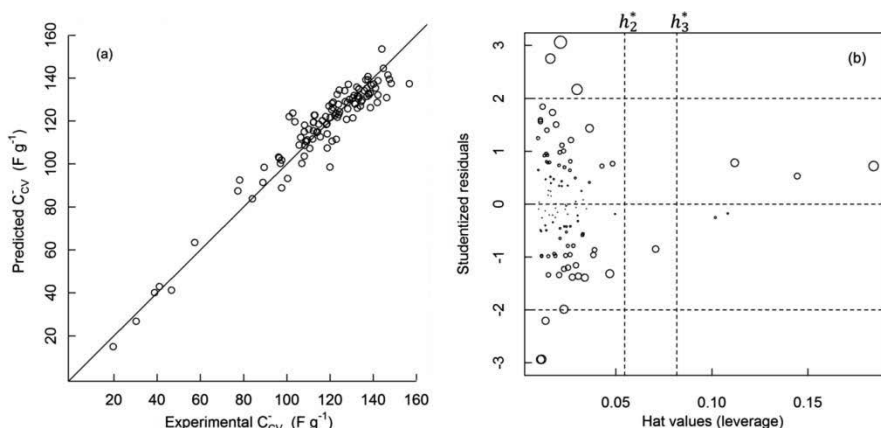


**Figure 19.** Experimental vs. predicted gravimetric capacitance (a) and model influence plot (b) corresponding to Eq. 21 [V].

According to this QnSPR model (Eq. 21), the effective surface area is presented as a combination from the volume of the most efficient pore size, which appears to be close to that of the size of a bare electrolyte ion, and the total surface area. Alone these parameters are not statistically sufficient to give prediction quality to the model (Figure 20). The relationship of cathodic and anodic capacitances on the SSA agrees that, in general, the capacitance increases with increasing specific surface area (Figure 20a). Comparison of  $V_t$  and  $V_\mu$  provides assurance that the pore size distribution is the one that plays a significant role in shaping capacitance. While increasing  $V_\mu$ , including ultra-micropores (Figures 20b and 20d) shows a clear proportional growth of capacitance, the  $V_t$  (Figure 20c) does not have straightforward effect on it. Comparing the pore volume relationships, one can clearly see that the capacitance of nanoporous CDC is strongly related to the amount of ultra-micropores not the total pore volume.

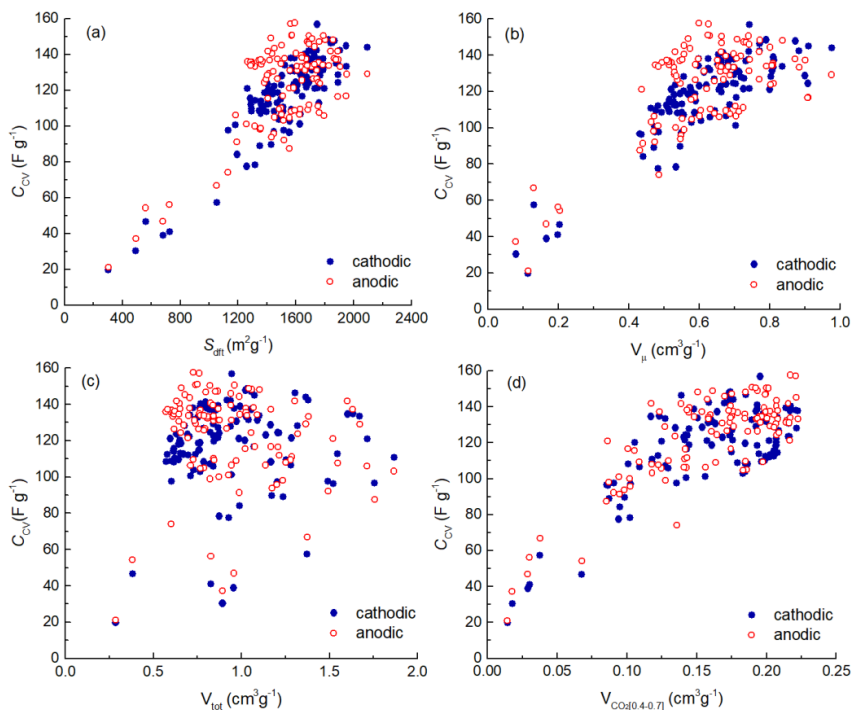


**Figure 20.** Specific capacitance ( $C_{CV}$ ) of CDC material vs.  $S_{dft}$  (a),  $V_{\mu}$  according DFT (b),  $V_t$  (c) and  $V_{CO_2[0.4-0.7]}$  (d) [V].

Considering the size of the  $SBP^+$  cation and common pore size distribution of CDC, the obtained model is consistent with the assumption that pores and ions with similar dimensions result in the highest EDL capacitance.

Model diagnostics is summarized in Figure 19b, where the vertical axis shows the standardized residuals, the horizontal axis shows the leverage (hat values) of observations with the two dashed vertical lines representing double ( $h_2^*$ ) and triple ( $h_3^*$ ) mean values, and the radii of circles show the Cook's distance. Following the influence plot (Figure 19b), one can see that the model is stable, without considerable outliers. Residuals analysis (on the vertical axis) shows six moderate outliers and five materials have higher hat-values (leverage). Cook's distances for all materials are also within the permitted limits. Materials with higher leverage values are of low capacitance and with more graphitic structure, synthesized at high temperature from  $Al_4C_3$  and SiC. The six moderate outliers do not form a clearly identifiable subgroup; however, the result is probably affected by the degree of purity of the carbon material, which is disparate over the materials.

Considering the increasing practical need to evaluate not only the electrochemical properties of the material but also the capacitance of the energy storage device, a model describing the volumetric capacitance was developed.

The best model for cathodic volumetric capacitance is with coefficient of determination  $R^2 = 0.95$  and estimated model scale parameter  $\hat{\sigma} = 5.16$  (Eq. 22). The correlation between predicted and experimentally measured capacitance values is shown in Figure 21.

$$C_{CV,vol}^- = -76.0 + 0.0357 \cdot S_{dft} + 143 \cdot V_{CO_2[0.4-0.7]} + 102 \cdot D_{el} \quad (22)$$

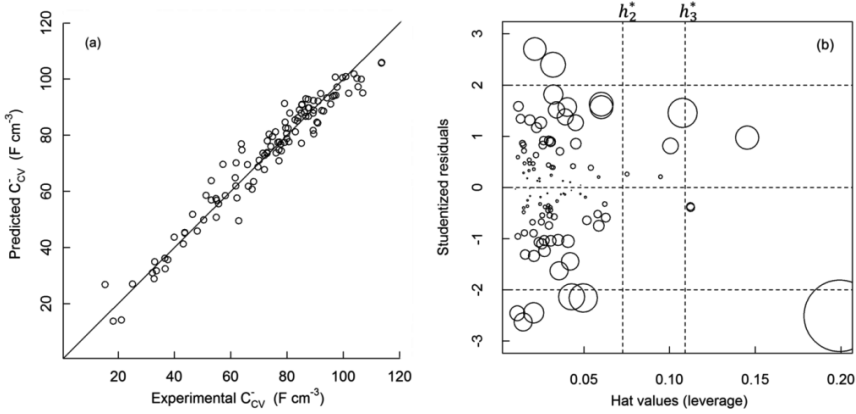


**Figure 21.** Experimental vs. predicted volumetric capacitance (a) and model influence plot (b) corresponding to Eq. 22 [V].

The first two descriptors  $S_{dft}$  and  $V_{CO_2[0.4-0.7]}$  take into account the properties of the carbon material in powder, while bulk density of the carbon electrode (third descriptor) characterizes the compressed conditions of the carbon particles in carbon film as discussed in the previous section.  $D_{el}$  is a complex value comprising the apparent density of the carbon, the density of the binder (kept constant in all examined carbon electrodes of this study) and the packing density of carbon particles in the finished electrode. Importantly, the last one also takes into account the possible differences in particles sizes in different CDC electrodes. It follows from the model (Eq. 22) that the denser the electrode, the higher the capacitance. However, attention should be drawn to the fact that it works within certain limits; the density of the electrode cannot be increased infinitely. In this work, the electrode densities range from 0.33 to 0.96 g cm<sup>-3</sup>.

The influence plot of model (Eq. 22) is shown in Figure 21b. The situation is quite similar to that of gravimetric capacitance model (Eq. 21): there are seven moderate outliers and four materials that have higher hat-values (leverage). Materials with higher hat values are the same as in gravimetric capacitance model, some accidental changes are among the seven moderate outliers. The main distinction is that, in this model, we have one material with higher Cook's distance (0.373 vs. critical level  $>1$  [128]). This material, made of SiC using

graphitizing catalysts, also has the smallest capacitance and is of the most graphitic structure. However, according to all three criteria (Cook’s distance, leverage and outlier detection), even this material (CDC-1) does not exceed the critical limit and we do not have a clear reason to believe that the current model is not suitable for this type (graphitic structure) of carbon material. In the case of the volumetric capacitance, in addition to the purity of the material, inaccuracies from the calculation of the electrode density must also be taken into account.

For the external validation of the models, four activated commercial carbons were used: YP-50 from Kuraray Chemical Co., Ltd; HDLC 20B STUW from Haycarb PLC; and V2 and P2 from EnerG2 Technologies Inc., which are commonly used electrode materials in energy storage devices [172]. As the results in Table 2 show, both models predict the capacitance of AC materials with a good accuracy, meaning that these models can be used for the primary capacitance assessment of activated carbons, too.

**Table 2.** Experimental and predicted capacitance values and selected descriptors for AC used for external validation of statistical models

AC	$S_{\text{dft}}$ ( $\text{m}^2\text{g}^{-1}$ )	$V_{\text{CO}_2[0.4-0.7]}$ (nm)	$D_{\text{el}}$ ( $\text{g cm}^{-3}$ )	$C_{\text{CV.g}}^-$ ( $\text{F g}^{-1}$ )		$C_{\text{CV.vol}}^-$ ( $\text{F cm}^{-3}$ )	
				Exp.	Pred.	Exp.	Pred.
YP-50	1531	0.159	0.676	120.3	117	72.4	70.4
V2	1573	0.171	0.773	122.5	122	84.7	83.5
HDLC 20B	1550	0.137	0.761	109.5	113.4	74.1	76.5
P2	1588	0.172	0.503	114.9	123.1	53.2	56.6

Both models (*i.e.* for gravimetric and volumetric capacitance in SBP-BF<sub>4</sub>/ACN) contain two common descriptors: the volume of a pore size fraction in between 0.4 and 0.7 nm, which is very close to the smallest dimension of the SBP<sup>+</sup> cation, and the specific surface area. A third descriptor, the electrode density, which is particularly dependent on the particle size of the carbon and the method of forming the electrodes, appears in the model for volumetric cathodic capacitance. As one can see, in both models, the coefficients of descriptors, SSA ( $S_{\text{dft}}$ ), the pore size fraction ( $V_{\text{CO}_2[0.4-0.7]}$ ) and bulk density of electrode ( $D_{\text{el}}$ ) are positive, meaning that with the increase of any descriptor values – individually or in combination, the capacitance increases as well.

In summary, using linear regression analysis, two models were independently developed; one to describe gravimetric cathodic capacitance, and the other for volumetric cathodic capacitance. Both models confirm the key role of the pore size fraction 0.4–0.7 nm, which is very close to the smallest dimension of the SBP<sup>+</sup> cation. All structure descriptors of the proposed QnSPR models have a clear physical meaning due to the association with the modeled EDL capacitance, thus giving the models a physical meaning. Both models and data are available at QsarDB repository (<http://dx.doi.org/10.15152/QDB.210>).

## SUMMARY

The dissertation focuses on nanoporous carbon materials, specifically, to the relationships between experimental properties and structure, relevant to the practical applications of carbide-derived carbon (CDC) materials, and on the coding of these relationships into multi-linear regression models. The study provides a comprehensive insight into the effect of pore size distribution on the electrical double-layer capacitance and helps to guide both the CDC synthesis process and post-treatment conditions to promote the development on carbon materials for energy storage.

This dissertation can be divided into two parts. The first part focuses on preparation and characterization of nanoporous carbon materials (approximately 200, starting from variety of precursors TiC, SiC, B<sub>4</sub>C, NbC, ZrC, Mo<sub>2</sub>C, Al<sub>4</sub>C<sub>3</sub>, TiC<sub>1-x</sub>N<sub>x</sub>, TiC<sub>x<1</sub>): the effects of synthesis conditions, modifications and post-treatment on the structure of carbon materials. The second part investigates QnSPRs based on experimental measurements (electrical double-layer capacitance vs. porosity characteristics) and develops multi-linear models that can be used to explain and predict specific capacitance of nanoporous carbon.

Current experimental studies clearly show that the carbon structure made on the high temperature chlorination of metal carbides depends on many different factors including chemical composition, reactivity and stoichiometry of the carbide. A well-known rule, that the higher the synthesis temperature the more preferable is the formation of CDC with graphite structure is confirmed in the work. It is also confirmed that the lower the proportion of carbon in the carbide, the wider the pore distribution on carbon. The results of the adsorption analysis of N<sub>2</sub> and CO<sub>2</sub> used to study the structural properties of the carbon materials synthesized in this research show that CDCs with narrow pore distribution can be made from silicon or titanium carbide, but broader pore distribution is achieved from niobium or zirconium carbide. Mo<sub>2</sub>C and B<sub>4</sub>C allow preparing the micro/mesoporous carbon materials.

The results of physical activation show that the macrostructure of nanoporous carbon materials does not change during activation, but the specific surface value can be varied within 1000 units (m<sup>2</sup>g<sup>-1</sup>). It was proved that carbon material with more amorphous structure is more susceptible to water vapor treatment and the total porosity of the material increases about 50% during the treatment. In addition, it is shown that using biomorphic carbide, made by carbothermal reduction of metal oxide and deciduous wood-origin charcoal (*e.g.*, bio-TiC) as starting carbide, can significantly affect the porosity of carbon. Among the nanoporous carbon materials investigated in this paper, CDCs made from biomorphic carbide exhibited the highest specific surface area and unique cellular morphology, which favors good mass transport into nanopores.

The effect of catalysts (metals of iron subgroup) on graphitization of the CDC structure was also investigated. The results show that the structure of the carbon materials highly depends on the combined effect of catalyst concentration and

synthesis temperature. In the presence of catalysts, it is possible to synthesize graphitically structured materials at much lower temperatures and the porosity of the material can be controlled in the wide range.

The second part of the dissertation examines the applicability of experiment-derived structural porosity descriptors to characterize carbon materials in QnSPR models. Predictive models have been constructed using multi-linear regression analysis to describe the electric double-layer capacitance of a nanoporous carbon in two non-aqueous electrolytes: SBP-BF<sub>4</sub> and TEMA-BF<sub>4</sub> in acetonitrile. The models contain three common descriptors for both electrolytes: the volume of a pore fraction of a certain size, the specific surface area of carbon, and the density of the electrode formed from the same carbon, which depends on the particle size of the carbon and the method of making the electrode.

The results of the studies set a milestone that experiment-derived structure descriptors calculated from the N<sub>2</sub> and CO<sub>2</sub> adsorption isotherms allow successfully construct QnSPR models that accurately describe and predict the specific capacitance of nanoporous carbon materials.

All molecular descriptors in QnSPR models do have clear physical-chemical meaning and the relationship with the modelled property (electric double-layer capacitance) gives physico-chemical significance to the models, *i.e.* they provide clear explanation of interaction mechanisms. The results obtained suggest that under fixed experimental conditions, the specific capacitance of the nanoporous carbon electrode depends mainly on the effective surface area of the carbon material. In the derived QnSPR models this is expressed as a combination of the volume of the most efficient pore size that appears to be close to that of the size of a bare electrolyte ion, and the total surface area.

In conclusion, for the first time, the multivariate mathematical models to describe and predict the physical and chemical properties of porous carbon using experiment-derived structural descriptors are constructed and the descriptors show their application potential in QnSPR models. The developed QnSPR models are well applicable for describing the electric double-layer capacitance of a nanoporous carbon with various pore size distributions; moreover they allow precise prediction of electric double-layer capacitance.

## REFERENCES

- [1] Kaneko, K.; Rodríguez-Reinoso, F. *Nanoporous Materials for Gas Storage*; Springer Nature Singapore Ltd, 2019.
- [2] Álvarez-Torrellas, S.; Munoz, M.; Gläsel, J.; de Pedro, Z. M.; Domínguez, C. M.; García, J.; Etzold, B. J. M.; Casas, J. A. Highly Efficient Removal of Pharmaceuticals from Water by Well-Defined Carbide-Derived Carbons. *Chem. Eng. J.*, **2018**, *347*, 595–606.
- [3] Gusain, R.; Kumar, N.; Ray, S. S. Recent Advances in Carbon Nanomaterial-Based Adsorbents for Water Purification. *Coord. Chem. Rev.*, **2020**, *405*, 213111.
- [4] White, R. J.; Ed. *Porous Carbon Materials from Sustainable Precursors*; RSC Green Chemistry; Royal Society of Chemistry: Cambridge, 2015.
- [5] Conway, B. E. *Electrochemical Supercapacitors: Scientific Fundamentals and Technological Applications*; Springer Science+Business Media: New York, 1999.
- [6] Béguin, F., Frackowiak, E.; Eds. *Supercapacitors: Materials, Systems, and Applications*; Wiley-VCH: Weinheim, 2013.
- [7] Béguin, F.; Presser, V.; Balducci, A.; Frackowiak, E. Carbons and Electrolytes for Advanced Supercapacitors. *Adv. Mater.*, **2014**, *26* (14), 2219–2251.
- [8] Mirzaeian, M.; Abbas, Q.; Ogwu, A.; Hall, P.; Goldin, M.; Mirzaeian, M.; Jirandehi, H. F. Electrode and Electrolyte Materials for Electrochemical Capacitors. *Int. J. Hydrog. Energy*, **2017**, *42* (40), 25565–25587.
- [9] Sarapuu, A.; Kibena-Pöldsepp, E.; Borghei, M.; Tammeveski, K. Electrocatalysis of Oxygen Reduction on Heteroatom-Doped Nanocarbons and Transition Metal–Nitrogen–Carbon Catalysts for Alkaline Membrane Fuel Cells. *J. Mater. Chem. A*, **2018**, *6* (3), 776–804.
- [10] Ratso, S.; Kruusenberg, I.; Käärik, M.; Kook, M.; Puust, L.; Saar, R.; Leis, J.; Tammeveski, K. Highly Efficient Transition Metal and Nitrogen Co-Doped Carbide-Derived Carbon Electrocatalysts for Anion Exchange Membrane Fuel Cells. *J. Power Sources*, **2018**, *375*, 233–243.
- [11] Ratso, S.; Ranjbar Sahraie, N.; Sougrati, M. T.; Käärik, M.; Kook, M.; Saar, R.; Paiste, P.; Jia, Q.; Leis, J.; Mukerjee, S.; et al. Synthesis of Highly-Active Fe–N–C Catalysts for PEMFC with Carbide-Derived Carbons. *J. Mater. Chem. A*, **2018**, *6* (30), 14663–14674.
- [12] Gogotsi, Y.; Ed. *Nanomaterials Handbook*; CRC/Taylor & Francis: Boca Raton, 2006.
- [13] Gogotsi, Y.; Nikitin, A.; Ye, H.; Zhou, W.; Fischer, J. E.; Yi, B.; Foley, H. C.; Barsoum, M. W. Nanoporous Carbide-Derived Carbon with Tunable Pore Size. *Nat. Mater.*, **2003**, *2* (9), 591–594.
- [14] Marsh, H.; Rodríguez-Reinoso, F. *Activated Carbon*, 1st ed.; Elsevier: Amsterdam ; Boston, 2006.
- [15] Bansal, R. C.; Goyal, M. *Activated Carbon Adsorption*; Taylor & Francis: Boca Raton, 2005.
- [16] Väli, R.; Jänes, A.; Thomberg, T.; Lust, E. D-Glucose Derived Nanospheric Hard Carbon Electrodes for Room-Temperature Sodium-Ion Batteries. *J. Electrochem. Soc.*, **2016**, *163* (8), A1619–A1626.

- [17] Ello, A. S.; de Souza, L. K. C.; Trokourey, A.; Jaroniec, M. Coconut Shell-Based Microporous Carbons for CO<sub>2</sub> Capture. *Microporous Mesoporous Mater.*, **2013**, *180*, 280–283.
- [18] Sharon, M.; Sharon, M. Effect of Inherent Anatomy of Plant Fibers on the Morphology of Carbon Synthesized from Them and Their Hydrogen Absorption Capacity. *Carbon Lett.*, **2012**, *13* (3), 161–166.
- [19] Lin, H.; Liu, Y.; Chang, Z.; Yan, S.; Liu, S.; Han, S. A New Method of Synthesizing Hemicellulose-Derived Porous Activated Carbon for High-Performance Supercapacitors. *Microporous Mesoporous Mater.*, **2020**, *292*, 109707.
- [20] González-García, P. Activated Carbon from Lignocellulosics Precursors: A Review of the Synthesis Methods, Characterization Techniques and Applications. *Renew. Sustain. Energy Rev.*, **2018**, *82*, 1393–1414.
- [21] Krüner, B.; Lee, J.; Jäckel, N.; Tolosa, A.; Presser, V. Sub-Micrometer Novolac-Derived Carbon Beads for High Performance Supercapacitors and Redox Electrolyte Energy Storage. *ACS Appl. Mater. Interfaces*, **2016**, *8* (14), 9104–9115.
- [22] Yuan, Z.; Zhang, Y.; Zhou, Y.; Han, J. Preparation and Characterization of Porous Carbons Obtained from Mixtures of Furfuryl Alcohol and Phenol-Formaldehyde Resin. *Mater. Chem. Phys.*, **2014**, *143* (2), 707–712.
- [23] Zhang, Z.; Luo, X.; Liu, Y.; Zhou, P.; Ma, G.; Lei, Z.; Lei, L. A Low Cost and Highly Efficient Adsorbent (Activated Carbon) Prepared from Waste Potato Residue. *J. Taiwan Inst. Chem. Eng.*, **2015**, *49*, 206–211.
- [24] Wong, S.; Ngadi, N.; Inuwa, I. M.; Hassan, O. Recent Advances in Applications of Activated Carbon from Biowaste for Wastewater Treatment: A Short Review. *J. Clean. Prod.*, **2018**, *175*, 361–375.
- [25] Singh, G.; Lakhi, K. S.; Sil, S.; Bhosale, S. V.; Kim, I.; Albahily, K.; Vinu, A. Biomass Derived Porous Carbon for CO<sub>2</sub> Capture. *Carbon*, **2019**, *148*, 164–186.
- [26] Volperts, A.; Plavniece, A.; Dobeles, G.; Zhurinsh, A.; Kruusenberg, I.; Kaare, K.; Locs, J.; Tamasauskaite-Tamasiunaite, L.; Norkus, E. Biomass Based Activated Carbons for Fuel Cells. *Renew. Energy*, **2019**, *141*, 40–45.
- [27] Nishihara, H.; Kyotani, T. Zeolite-Templated Carbons – Three-Dimensional Microporous Graphene Frameworks. *Chem. Commun.*, **2018**, *54* (45), 5648–5673.
- [28] Urbonaite, S.; Juárez-Galán, J. M.; Leis, J.; Rodríguez-Reinoso, F.; Svensson, G. Porosity Development along the Synthesis of Carbons from Metal Carbides. *Microporous Mesoporous Mater.*, **2008**, *113* (1–3), 14–21.
- [29] Leis, J.; Perkson, A.; Arulepp, M.; Käärik, M.; Svensson, G. Carbon Nanostructures Produced by Chlorinating Aluminium Carbide. *Carbon*, **2001**, *39* (13), 2043–2048.
- [30] Perkson, A.; Leis, J.; Arulepp, M.; Käärik, M.; Urbonaite, S.; Svensson, G. Barrel-like Carbon Nanoparticles from Carbide by Catalyst Assisted Chlorination. *Carbon*, **2003**, *41* (9), 1729–1735.
- [31] Gogotsi, Y.; Welz, S.; Ersoy, D. A.; McNallan, M. J. Conversion of Silicon Carbide to Crystalline Diamond-Structured Carbon at Ambient Pressure. *Nature*, **2001**, *411* (6835), 283–287.
- [32] Tee, E.; Tallo, I.; Thomberg, T.; Jänes, A.; Lust, E. Steam and Carbon Dioxide Co-Activated Silicon Carbide-Derived Carbons for High Power Density Electrical Double Layer Capacitors. *J. Electrochem. Soc.*, **2018**, *165* (10), A2357–A2364.

- [33] Leis, J.; Arulepp, M.; Käärrik, M.; Perkson, A. The Effect of Mo<sub>2</sub>C Derived Carbon Pore Size on the Electrical Double-Layer Characteristics in Propylene Carbonate-Based Electrolyte. *Carbon*, **2010**, *48* (14), 4001–4008.
- [34] Jänes, A.; Thomberg, T.; Kurig, H.; Lust, E. Nanoscale Fine-Tuning of Porosity of Carbide-Derived Carbon Prepared from Molybdenum Carbide. *Carbon*, **2009**, *47* (1), 23–29.
- [35] Leis, J.; Perkson, A.; Arulepp, M.; Nigu, P.; Svensson, G. Catalytic Effects of Metals of the Iron Subgroup on the Chlorination of Titanium Carbide to Form Nanostructural Carbon. *Carbon*, **2002**, *40* (9), 1559–1564.
- [36] Dash, R.; Chmiola, J.; Yushin, G.; Gogotsi, Y.; Laudisio, G.; Singer, J.; Fischer, J.; Kucheyev, S. Titanium Carbide Derived Nanoporous Carbon for Energy-Related Applications. *Carbon*, **2006**, *44* (12), 2489–2497.
- [37] Dash, R. K.; Yushin, G.; Gogotsi, Y. Synthesis, Structure and Porosity Analysis of Microporous and Mesoporous Carbon Derived from Zirconium Carbide. *Microporous Mesoporous Mater.*, **2005**, *86* (1–3), 50–57.
- [38] Xu, J. ( 1 ); Wu, C. ( 1 ); Yan, P. ( 1 ); Zhang, R. ( 1 ); Yue, X. ( 2 ); Ge, S. ( 3 ). Pore Characteristics of Carbide-Derived Carbons Obtained from Carbides with Different Carbon Volume Fractions. *Microporous Mesoporous Mater.*, **2014**, *198*, 74–81.
- [39] Yan, P.; Xu, J.; Wu, C.; Zhang, R.; Jin, J. Structure and Supercapacitive Performance of Hierarchical Porous Carbon Obtained by Catalyzing Microporous Carbide-Derived Carbon. *Mater. Lett.*, **2015**, *139*, 340–343.
- [40] Xu, J.; Zhang, R.; Chen, P.; Shen, D.; Ye, X.; Ge, S. Mechanism of Formation and Electrochemical Performance of Carbide-Derived Carbons Obtained from Different Carbides. *Carbon*, **2013**, *64*, 444–455.
- [41] Dash, R. K.; Nikitin, A.; Gogotsi, Y. Microporous Carbon Derived from Boron Carbide. *Microporous Mesoporous Mater.*, **2004**, *72* (1–3), 203–208.
- [42] Dimovski, S.; Nikitin, A.; Ye, H.; Gogotsi, Y. Synthesis of Graphite by Chlorination of Iron Carbide at Moderate Temperatures. *J. Mater. Chem.*, **2004**, *14* (2), 238.
- [43] Thomberg, T.; Kurig, H.; Jänes, A.; Lust, E. Mesoporous Carbide-Derived Carbons Prepared from Different Chromium Carbides. *Microporous Mesoporous Mater.*, **2011**, *141* (1–3), 88–93.
- [44] Tallo, I.; Thomberg, T.; Kontturi, K.; Jänes, A.; Lust, E. Nanostructured Carbide-Derived Carbon Synthesized by Chlorination of Tungsten Carbide. *Carbon*, **2011**, *49* (13), 4427–4433.
- [45] González-García, P.; Navarro-Suárez, A. M.; Carretero-González, J.; Urones-Garrote, E.; Ávila-Brandé, D.; Otero-Díaz, L. C. Nanostructure, Porosity and Electrochemical Performance of Chromium Carbide Derived Carbons. *Carbon*, **2015**, *85*, 38–49.
- [46] Presser, V.; Heon, M.; Gogotsi, Y. Carbide-Derived Carbons - From Porous Networks to Nanotubes and Graphene. *Adv. Funct. Mater.*, **2011**, *21* (5), 810–833.
- [47] Kukushkina, J. A.; Sokolov, V. V.; Tomkovich, M. V. Effect of Nonstoichiometry of Titanium Carbide on Porous Structure of Nanoporous Carbon Produced from the Carbide. *Russ. J. Appl. Chem.*, **2015**, *88* (1), 27–30.
- [48] Tallo, I.; Thomberg, T.; Kurig, H.; Kontturi, K.; Jänes, A.; Lust, E. Novel Micro-mesoporous Carbon Materials Synthesized from Tantalum Hafnium Carbide and Tungsten Titanium Carbide. *Carbon*, **2014**, *67*, 607–616.

- [49] Seo, M. S.; Kim, J. H.; Kim, J. M.; Han, J. S.; Kang, S.; Ihm, J. S.; Kim, D. O. Tunable and Selective Formation of Micropores and Mesopores in Carbide-Derived Carbon. *Carbon*, **2013**, *60*, 299–306.
- [50] Sui, J.; Lu, J.-J. Synthesis of Carbon Nitride Powder by Selective Etching of TiC<sub>0.3</sub>N<sub>0.7</sub> in Chlorine-Containing Atmosphere at Moderate Temperature. *Mater. Chem. Phys.*, **2010**, *123* (1), 264–268.
- [51] Yeon, S.-H.; Jung, K.-N.; Yoon, S.; Shin, K.-H.; Jin, C.-S. Electrochemical Performance of Carbide-Derived Carbon Anodes for Lithium-Ion Batteries. *J. Phys. Chem. Solids*, **2013**, *74* (7), 1045–1055.
- [52] Käärik, M.; Arulepp, M.; Kook, M.; Kozlova, J.; Ritslaid, P.; Aruväli, J.; Mäeorg, U.; Sammelselg, V.; Leis, J. A Microporous Carbide-Derived Carbon of Leaf-Wood Origin as an Electrode Material for the Electrical Double-Layer Capacitor; *7th Baltic Electrochemistry Conference: Finding New Inspiration*, Tartu, 2018.
- [53] Dyjak, S.; Kiciński, W.; Norek, M.; Dyjak, M.; Cudziło, S. Carbide-Derived Carbon Obtained via Bromination of Titanium Carbide: Comparative Analysis with Chlorination and Hydrogen Storage Studies. *Microporous Mesoporous Mater.*, **2019**, *273*, 26–34.
- [54] Batische, N.; Guérin, K.; Dubois, M.; Hamwi, A. The Synthesis of Microporous Carbon by the Fluorination of Titanium Carbide. *Carbon*, **2011**, *49* (9), 2998–3009.
- [55] Xu, J.; Zhang, R.; Ge, S.; Wang, J.; Liu, Y.; Chen, P. Effect of Iron Catalyst on the Microstructure and Electrochemical Properties of Vanadium Carbide-Derived Carbons. *Mater. Chem. Phys.*, **2013**, *141* (1), 540–548.
- [56] Jeong, J.-H.; Bae, H.-T.; Lim, D.-S. The Effect of Iron Catalysts on the Microstructure and Tribological Properties of Carbide-Derived Carbon. *Carbon*, **2010**, *48* (12), 3628–3634.
- [57] Ariyanto, T.; Glaesel, J.; Kern, A.; Zhang, G.-R.; Etzold, B. J. M. Improving Control of Carbide-Derived Carbon Microstructure by Immobilization of a Transition-Metal Catalyst within the Shell of Carbide/Carbon Core-Shell Structures. *Beilstein J. Nanotechnol.*, **2019**, *10*, 419–427.
- [58] Portet, C.; Lillo-Ródenas, M. Á.; Linares-Solano, A.; Gogotsi, Y. Capacitance of KOH Activated Carbide-Derived Carbons. *Phys. Chem. Chem. Phys.*, **2009**, *11* (25), 4943.
- [59] Sevilla, M.; Mokaya, R. Activation of Carbide-Derived Carbons: A Route to Materials with Enhanced Gas and Energy Storage Properties. *J Mater Chem*, **2011**, *21* (13), 4727–4732.
- [60] Kierzek, K.; Frackowiak, E.; Lota, G.; Gryglewicz, G.; Machnikowski, J. Electrochemical Capacitors Based on Highly Porous Carbons Prepared by KOH Activation. *Electrochimica Acta*, **2004**, *49* (4), 515–523.
- [61] Osswald, S.; Portet, C.; Gogotsi, Y.; Laudisio, G.; Singer, J. P.; Fischer, J. E.; Sokolov, V. V.; Kukulshkina, J. A.; Kravchik, A. E. Porosity Control in Nanoporous Carbide-Derived Carbon by Oxidation in Air and Carbon Dioxide. *J. Solid State Chem.*, **2009**, *182* (7), 1733–1741.
- [62] Kormann, M.; Popovska, N. Processing of Carbide-Derived Carbons with Enhanced Porosity by Activation with Carbon Dioxide. *Microporous Mesoporous Mater.*, **2010**, *130* (1), 167–173.
- [63] Tee, E.; Tallo, I.; Kurig, H.; Thomberg, T.; Jänes, A.; Lust, E. Huge Enhancement of Energy Storage Capacity and Power Density of Supercapacitors Based

- on the Carbon Dioxide Activated Microporous SiC-CDC. *Electrochimica Acta*, **2015**, *161*, 364–370.
- [64] Duan, L.; Ma, Q.; Ma, L.; Dong, L.; Wang, B.; Dai, X.; Zhang, B. Effect of the CO<sub>2</sub> Activation Parameters on the Pore Structure of Silicon Carbide-Derived Carbons. *New Carbon Mater.*, **2019**, *34* (4), 367–372.
- [65] Fałtynowicz, H.; Kaczmarczyk, J.; Kułażyński, M. Preparation and Characterization of Activated Carbons from Biomass Material – Giant Knotweed (*Reynoutria Sachalinensis*). *Open Chem.*, **2015**, *13* (1).
- [66] Tee, E.; Tallo, I.; Lust, E.; Jänes, A.; Thomberg, T. Electrical Double Layer Capacitors Based on Steam and CO<sub>2</sub> -Steam Co-Activated Carbon Electrodes and Ionic Liquid Electrolyte. *J. Electrochem. Soc.*, **2019**, *166* (8), A1558–A1567.
- [67] Bleda-Martínez, M. J.; Maciá-Agulló, J. A.; Lozano-Castelló, D.; Morallón, E.; Cazorla-Amorós, D.; Linares-Solano, A. Role of Surface Chemistry on Electric Double Layer Capacitance of Carbon Materials. *Carbon*, **2005**, *43* (13), 2677–2684.
- [68] Gusachenko, E. I.; Stesik, L. N. The Oxidation of High-Dispersity Diamond and Amorphous Carbon Powders by Water Vapor. *Russ. J. Phys. Chem. B*, **2011**, *5* (2), 220–226.
- [69] Molina-Sabio, M.; Gonzalez, M. T.; Rodriguez-Reinoso, F.; Sepúlveda-Escribano, A. Effect of Steam and Carbon Dioxide Activation in the Micropore Size Distribution of Activated Carbon. *Carbon*, **1996**, *34* (4), 505–509.
- [70] Rodríguez-Reinoso, F.; Molina-Sabio, M.; González, M. T. The Use of Steam and CO<sub>2</sub> as Activating Agents in the Preparation of Activated Carbons. *Carbon*, **1995**, *33* (1), 15–23.
- [71] Popovska N.; Almeida-Streitwieser D.; Xu C.; Gerhard H.; Sieber H. Kinetic Analysis of the Processing of Porous Biomorphic Titanium Carbide Ceramics by Chemical Vapor Infiltration. *Chem. Vap. Depos.*, **2005**, *11* (3), 153–158.
- [72] Borchardt, L.; Hoffmann, C.; Oschatz, M.; Mammitzsch, L.; Petasch, U.; Herrmann, M.; Kaskel, S. Preparation and Application of Cellular and Nanoporous Carbides. *Chem. Soc. Rev.*, **2012**, *41* (15), 5053.
- [73] Yukhymchuk, V. O.; Kiselov, V. S.; Valakh, M. Y.; Tryus, M. P.; Skoryk, M. A.; Rozhin, A. G.; Kulinich, S. A.; Belyaev, A. E. Biomorphous SiC Ceramics Prepared from Cork Oak as Precursor. *J. Phys. Chem. Solids*, **2016**, *91*, 145–151.
- [74] Greil, P.; Vogli, E.; Fey, T.; Bezold, A.; Popovska, N.; Gerhard, H.; Sieber, H. Effect of Microstructure on the Fracture Behavior of Biomorphous Silicon Carbide Ceramics. *J. Eur. Ceram. Soc.*, **2002**, *22* (14–15), 2697–2707.
- [75] Rambo, C. R.; Cao, J.; Rusina, O.; Sieber, H. Manufacturing of Biomorphous (Si,Ti,Zr)-Carbide Ceramics by Sol–Gel Processing. *Carbon*, **2005**, *43* (6), 1174–1183.
- [76] Gómez-Martín, A.; Orihuela, M. P.; Ramírez-Rico, J.; Chacartegui, R.; Martínez-Fernández, J. Thermal Conductivity of Porous Biomorphous SiC Derived from Wood Precursors. *Ceram. Int.*, **2016**, *42* (14), 16220–16229.
- [77] Adam, M.; Oschatz, M.; Nickel, W.; Kaskel, S. Preparation of Hierarchical Porous Biomorphous Carbide-Derived Carbon by Polycarbosilane Impregnation of Wood. *Microporous Mesoporous Mater.*, **2015**, *210*, 26–31.
- [78] Kormann, M.; Gerhard, H.; Popovska, N. Comparative Study of Carbide-Derived Carbons Obtained from Biomorphous TiC and SiC Structures. *Carbon*, **2009**, *47* (1), 242–250.

- [79] Kormann, M.; Ghanem, H.; Gerhard, H.; Popovska, N. Processing of Carbide-Derived Carbon (CDC) Using Biomorphic Porous Titanium Carbide Ceramics. *J. Eur. Ceram. Soc.*, **2008**, *28* (6), 1297–1303.
- [80] Rouquerol, F.; Rouquerol, J.; Sing, K. S. W.; Llewellyn, P. L.; Maurin, G. *Adsorption by Powders and Porous Solids: Principles, Methodology and Applications*, Second edition.; Elsevier/AP: Amsterdam, 2014.
- [81] Thommes, M.; Kaneko, K.; Neimark, A. V.; Olivier, J. P.; Rodriguez-Reinoso, F.; Rouquerol, J.; Sing, K. S. W. Physisorption of Gases, with Special Reference to the Evaluation of Surface Area and Pore Size Distribution (IUPAC Technical Report). *Pure Appl. Chem.*, **2015**, *87* (9–10).
- [82] Kreyling, W. G.; Semmler-Behnke, M.; Chaudhry, Q. A Complementary Definition of Nanomaterial. *Nano Today*, **2010**, *5* (3), 165–168.
- [83] Sing, K. S. W. Reporting Physisorption Data for Gas/Solid Systems with Special Reference to the Determination of Surface Area and Porosity (Recommendations 1984). *Pure Appl. Chem.*, **1985**, *57* (4), 603–619.
- [84] Tascón, J. M. D.; Ed. *Novel Carbon Adsorbents*; Elsevier: Oxford, U.K., 2012.
- [85] Landers, J.; Gor, G. Yu.; Neimark, A. V. Density Functional Theory Methods for Characterization of Porous Materials. *Colloids Surf. Physicochem. Eng. Asp.*, **2013**, *437*, 3–32.
- [86] Caguiat, J. N.; Kirk, D. W.; Jia, C. Q. Uncertainties in Characterization of Nanoporous Carbons Using Density Functional Theory-Based Gas Physisorption. *Carbon*, **2014**, *72*, 47–56.
- [87] Brunauer, S.; Emmett, P. H.; Teller, E. Adsorption of Gases in Multimolecular Layers. *J. Am. Chem. Soc.*, **1938**, *60* (2), 309–319.
- [88] NOVAtouch™ Model 1 and TouchWin™ Version 1.1 Operating Manual. Quantachrome Instruments 1900 Corporate Drive Boynton Beach, FL 33426 USA 2016 2015.
- [89] de Boer, J. H.; Lippens, B. C.; Linsen, B. G.; Broekhoff, J. C. P.; van den Heuvel, A.; Osinga, Th. J. Thet-Curve of Multimolecular N<sub>2</sub>-Adsorption. *J. Colloid Interface Sci.*, **1966**, *21* (4), 405–414.
- [90] Kanellopoulos, N.; Ed. *Nanoporous Materials: Advanced Techniques for Characterization, Modeling, and Processing*; CRC Press, Boca Raton, 2011.
- [91] Halsey, G. Physical Adsorption on Non-Uniform Surfaces. *J. Chem. Phys.*, **1948**, *16* (10), 931–937.
- [92] Deboer, J. Studies on Pore Systems in Catalysts VII. Description of the Pore Dimensions of Carbon Blacks by the t Method. *J. Catal.*, **1965**, *4* (6), 649–653.
- [93] Olivier, J. P. Modeling Physical Adsorption on Porous and Nonporous Solids Using Density Functional Theory. *J. Porous Mater.*, **1995**, *2* (1), 9–17.
- [94] Neimark, A. V.; Lin, Y.; Ravikovitch, P. I.; Thommes, M. Quenched Solid Density Functional Theory and Pore Size Analysis of Micro-Mesoporous Carbons. *Carbon*, **2009**, *47* (7), 1617–1628.
- [95] Barrett, E. P.; Joyner, L. G.; Halenda, P. P. The Determination of Pore Volume and Area Distributions in Porous Substances. I. Computations from Nitrogen Isotherms. *J. Am. Chem. Soc.*, **1951**, *73* (1), 373–380.
- [96] Țucureanu, V.; Matei, A.; Avram, A. M. FTIR Spectroscopy for Carbon Family Study. *Crit. Rev. Anal. Chem.*, **2016**, *46* (6), 502–520.
- [97] Teng, L.; Tang, T. IR Study on Surface Chemical Properties of Catalytic Grown Carbon Nanotubes and Nanofibers. *J. Zhejiang Univ.-Sci. A*, **2008**, *9* (5), 720–726. <https://doi.org/10.1631/jzus.A071503>.

- [98] Inagaki, M.; Ed. *Materials Science and Engineering of Carbon: Characterization*; Elsevier: Amsterdam, 2016.
- [99] Brender, P.; Gadiou, R.; Rietsch, J.-C.; Fioux, P.; Dentzer, J.; Ponche, A.; Vix-Guterl, C. Characterization of Carbon Surface Chemistry by Combined Temperature Programmed Desorption with in Situ X-Ray Photoelectron Spectrometry and Temperature Programmed Desorption with Mass Spectrometry Analysis. *Anal. Chem.*, **2012**, *84* (5), 2147–2153.
- [100] Ferrari, A. C.; Robertson, J. Interpretation of Raman Spectra of Disordered and Amorphous Carbon. *Phys. Rev. B*, **2000**, *61* (20), 14095–14107.
- [101] Zickler, G. A.; Smarsly, B.; Gierlinger, N.; Peterlik, H.; Paris, O. A Reconsideration of the Relationship between the Crystallite Size  $L_a$  of Carbons Determined by X-Ray Diffraction and Raman Spectroscopy. *Carbon*, **2006**, *44* (15), 3239–3246.
- [102] Inagaki, M.; Ed. *New Carbons: Control of Structure and Functions*; Elsevier Science: Amsterdam; New York, 2000.
- [103] Zou, L.; Huang, B.; Huang, Y.; Huang, Q.; Wang, C. An Investigation of Heterogeneity of the Degree of Graphitization in Carbon–Carbon Composites. *Mater. Chem. Phys.*, **2003**, *82* (3), 654–662.
- [104] Kravchik, A. E.; Osmakov, A. S.; Avarbe, R. G. Analysis of a Structure of Paracrystalline and Turbostratic Carbon Materials. *Zh Prikl Khim*, **1989**, *62* (11), 2430–2435.
- [105] Ferrari, A. C. Raman Spectroscopy of Graphene and Graphite: Disorder, Electron–Phonon Coupling, Doping and Nonadiabatic Effects. *Solid State Commun.*, **2007**, *143* (1–2), 47–57.
- [106] Tuinstra, F.; Koenig, J. L. Raman Spectrum of Graphite. *J. Chem. Phys.*, **1970**, *53* (3), 1126–1130.
- [107] Sato, Y.; Kamo, M.; Setaka, N. Raman Spectra of Carbons at 2600–3300  $\text{cm}^{-1}$  Region. *Carbon*, **1978**, *16* (4), 279–280.
- [108] Lee, Y.-J. The Second Order Raman Spectroscopy in Carbon Crystallinity. *J. Nucl. Mater.*, **2004**, *325* (2–3), 174–179.
- [109] Harris, P. Transmission Electron Microscopy of Carbon: A Brief History. *C*, **2018**, *4* (1), 4.
- [110] Oschatz, M.; Pré, P.; Dörfler, S.; Nickel, W.; Beaunier, P.; Rouzaud, J.-N.; Fischer, C.; Brunner, E.; Kaskel, S. Nanostructure Characterization of Carbide-Derived Carbons by Morphological Analysis of Transmission Electron Microscopy Images Combined with Physisorption and Raman Spectroscopy. *Carbon*, **2016**, *105*, 314–322.
- [111] de Tomas, C.; Suarez-Martinez, I.; Vallejos-Burgos, F.; López, M. J.; Kaneko, K.; Marks, N. A. Structural Prediction of Graphitization and Porosity in Carbide-Derived Carbons. *Carbon*, **2017**, *119*, 1–9.
- [112] Urbonaitė, S.; Wachtmeister, S.; Mirguet, C.; Coronel, E.; Zou, W. Y.; Csillag, S.; Svensson, G. EELS Studies of Carbide Derived Carbons. *Carbon*, **2007**, *45* (10), 2047–2053.
- [113] Haerle, R.; Riedo, E.; Pasquarello, A.; Baldereschi, A.  $\text{sp}^2 / \text{sp}^3$  Hybridization Ratio in Amorphous Carbon from C 1 s Core-Level Shifts: X-Ray Photoelectron Spectroscopy and First-Principles Calculation. *Phys. Rev. B*, **2001**, *65* (4), 045101.

- [114] Titantah, J. T.; Lamoen, D. Sp<sup>3</sup>/Sp<sup>2</sup> Characterization of Carbon Materials from First-Principles Calculations: X-Ray Photoelectron versus High Energy Electron Energy-Loss Spectroscopy Techniques. *Carbon*, **2005**, *43* (6), 1311–1316.
- [115] Mezzi, A.; Kaciulis, S. Surface Investigation of Carbon Films: From Diamond to Graphite. *Surf. Interface Anal.*, **2010**, *42* (6–7), 1082–1084.
- [116] Piir, G.; Kahn, I.; García-Sosa, A. T.; Sild, S.; Ahte, P.; Maran, U. Best Practices for QSAR Model Reporting: Physical and Chemical Properties, Ecotoxicity, Environmental Fate, Human Health, and Toxicokinetics Endpoints. *Environ. Health Perspect.*, **2018**, *126* (12), 126001.
- [117] Karelson, M. *Molecular Descriptors in QSAR/QSPR*; Wiley-Interscience: New York, 2000.
- [118] Roy, K.; Kar, S.; Das, R.N. *A Primer on QSAR/QSPR Modeling*; Springer Heidelberg: New York, 2015.
- [119] Zhou, T.; Song, Z.; Sundmacher, K. Big Data Creates New Opportunities for Materials Research: A Review on Methods and Applications of Machine Learning for Materials Design. *Engineering*, **2019**, S2095809918313559.
- [120] Shahlaei, M. Descriptor Selection Methods in Quantitative Structure–Activity Relationship Studies: A Review Study. *Chem. Rev.*, **2013**, *113* (10), 8093–8103.
- [121] Draper, N. R.; Smith, H. *Applied Regression Analysis*, 3rd ed.; Wiley series in probability and statistics; Wiley: New York, 1998.
- [122] Fox, J.; Weisberg, S. *An R Companion to Applied Regression*, Third edition.; Sage Publications, Inc: Thousand Oaks, California, 2019.
- [123] Fox, J.; Fox, J. *Applied Regression Analysis and Generalized Linear Models*, Third Edition.; SAGE: Los Angeles, 2016.
- [124] Jaworska, J.; Nikolova-Jeliazkova, N.; Aldenberg, T. QSAR Applicability Domain Estimation by Projection of the Training Set in Descriptor Space: A Review. *Altern. Lab. Anim.*, **2005**, *33* (5), 445–459.
- [125] Netzeva, T. I.; Worth, A. P.; Aldenberg, T.; Benigni, R.; Cronin, M. T. D.; Gramatica, P.; Jaworska, J. S.; Kahn, S.; Klopman, G.; Marchant, C. A.; et al. Current Status of Methods for Defining the Applicability Domain of (Quantitative) Structure-Activity Relationships: The Report and Recommendations of ECVAM Workshop 52. *Altern. Lab. Anim.*, **2005**, *33* (2), 155–173.
- [126] Sahigara, F.; Mansouri, K.; Ballabio, D.; Mauri, A.; Consonni, V.; Todeschini, R. Comparison of Different Approaches to Define the Applicability Domain of QSAR Models. *Molecules*, **2012**, *17* (5), 4791–4810.
- [127] Atkinson, A. C. *Plots, Transformations, and Regression: An Introduction to Graphical Methods of Diagnostic Regression Analysis*; Oxford University Press: Oxford, 1985.
- [128] Cook, R. D.; Weisberg, S. *Residuals and Influence in Regression*; Monographs on statistics and applied probability; Chapman and Hall: New York, 1982.
- [129] Puzyn, T.; Leszczynska, D.; Leszczynski, J. Toward the Development of “Nano-QSARs”: Advances and Challenges. *Small*, **2009**, *5* (22), 2494–2509.
- [130] Fourches, D.; Pu, D.; Tassa, C.; Weissleder, R.; Shaw, S. Y.; Mumper, R. J.; Tropsha, A. Quantitative Nanostructure–Activity Relationship Modeling. *ACS Nano*, **2010**, *4* (10), 5703–5712.
- [131] Worth, A.; Aschberger, K.; Asturiol Bofill, D.; Bessems, J.; Gerloff, K.; Graepel, R.; Joossens, E.; Lamon, L.; Palosaari, T.; Richarz, A. *Evaluation of the Availability and Applicability of Computational Approaches in the Safety*

- Assessment of Nanomaterials*; EUR 28617 EN; Publications Office of the European Union: Luxemburg, 2017.
- [132] Le, T.; Epa, V. C.; Burden, F. R.; Winkler, D. A. Quantitative Structure–Property Relationship Modeling of Diverse Materials Properties. *Chem. Rev.*, **2012**, *112* (5), 2889–2919.
- [133] Xu, X.; Li, L.; Yan, F.; Jia, Q.; Wang, Q.; Ma, P. Predicting Solubility of Fullerene C 60 in Diverse Organic Solvents Using Norm Indexes. *J. Mol. Liq.*, **2016**, *223*, 603–610.
- [134] Martin, D.; Maran, U.; Sild, S.; Karelson, M. QSPR Modeling of Solubility of Polyaromatic Hydrocarbons and Fullerene in 1-Octanol and *n*-Heptane. *J. Phys. Chem. B*, **2007**, *111* (33), 9853–9857.
- [135] Martin, D.; Sild, S.; Maran, U.; Karelson, M. QSPR Modeling of the Polarizability of Polyaromatic Hydrocarbons and Fullerenes. *J. Phys. Chem. C*, **2008**, *112* (13), 4785–4790.
- [136] Metivier-Pignon, H.; Faur, C.; Cloirec, P. L. Adsorption of Dyes onto Activated Carbon Cloth: Using QSPRs as Tools to Approach Adsorption Mechanisms. *Chemosphere*, **2007**, *66* (5), 887–893.
- [137] Rahimi-Nasrabadi, M.; Akhoondi, R.; Pourmortazavi, S. M.; Ahmadi, F. Predicting Adsorption of Aromatic Compounds by Carbon Nanotubes Based on Quantitative Structure Property Relationship Principles. *J. Mol. Struct.*, **2015**, *1099*, 510–515.
- [138] Lata, S.; Vikas. Concentration Dependent Adsorption of Aromatic Organic Compounds by SWCNTs: Quantum-Mechanical Descriptors for Nano-Toxicological Studies of Biomolecules and Agrochemicals. *J. Mol. Graph. Model.*, **2018**, *85*, 232–241.
- [139] Toropova, A. P.; Toropov, A. A. Assessment of Nano-QSPR Models of Organic Contaminant Absorption by Carbon Nanotubes for Ecological Impact Studies. *Mater. Discov.*, **2016**, *4*, 22–28.
- [140] Yilmaz, H.; Rasulev, B.; Leszczynski, J. Modeling the Dispersibility of Single Walled Carbon Nanotubes in Organic Solvents by Quantitative Structure-Activity Relationship Approach. *Nanomaterials*, **2015**, *5* (2), 778–791.
- [141] González-Durruthy, M.; Alberici, L. C.; Curti, C.; Naal, Z.; Atique-Sawazaki, D. T.; Vázquez-Naya, J. M.; González-Díaz, H.; Munteanu, C. R. Experimental–Computational Study of Carbon Nanotube Effects on Mitochondrial Respiration: In Silico Nano-QSPR Machine Learning Models Based on New Raman Spectra Transform with Markov–Shannon Entropy Invariants. *J. Chem. Inf. Model.*, **2017**, *57* (5), 1029–1044.
- [142] Winkler, D. A.; Mombelli, E.; Pietroiusti, A.; Tran, L.; Worth, A.; Fadeel, B.; McCall, M. J. Applying Quantitative Structure–Activity Relationship Approaches to Nanotoxicology: Current Status and Future Potential. *Toxicology*, **2013**, *313* (1), 15–23.
- [143] Winkler, D. A. Recent Advances, and Unresolved Issues, in the Application of Computational Modelling to the Prediction of the Biological Effects of Nanomaterials. *Toxicol. Appl. Pharmacol.*, **2016**, *299*, 96–100.
- [144] Burello, E. Review of (Q)SAR Models for Regulatory Assessment of Nanomaterials Risks. *NanoImpact*, **2017**, *8*, 48–58.
- [145] Oksel, C.; Ma, C. Y.; Liu, J. J.; Wilkins, T.; Wang, X. Z. (Q)SAR Modelling of Nanomaterial Toxicity: A Critical Review. *Particuology*, **2015**, *21*, 1–19.

- [146] Lobato, B.; Suarez, L.; Guardia, L.; Centeno, T. A. Capacitance and Surface of Carbons in Supercapacitors. *Carbon*, **2017**, *122*, 434–445.
- [147] Jäckel, N.; Rodner, M.; Schreiber, A.; Jeongwook, J.; Zeiger, M.; Aslan, M.; Weingarh, D.; Presser, V. Anomalous or Regular Capacitance? The Influence of Pore Size Dispersity on Double-Layer Formation. *J. Power Sources*, **2016**, *326*, 660–671.
- [148] Chmiola, J.; Yushin, G.; Dash, R.; Gogotsi, Y. Effect of Pore Size and Surface Area of Carbide Derived Carbons on Specific Capacitance. *J. Power Sources*, **2006**, *158* (1), 765–772. <https://doi.org/10.1016/j.jpowsour.2005.09.008>.
- [149] Viswanathan, B. *Energy Sources: Fundamentals of Chemical Conversion Processes and Applications*; Elsevier: Amsterdam ; Boston, 2017.
- [150] Barbieri, O.; Hahn, M.; Herzog, A.; Kötz, R. Capacitance Limits of High Surface Area Activated Carbons for Double Layer Capacitors. *Carbon*, **2005**, *43* (6), 1303–1310.
- [151] García-Gómez, A.; Moreno-Fernández, G.; Lobato, B.; Centeno, T. A. Constant Capacitance in Nanopores of Carbon Monoliths. *Phys. Chem. Chem. Phys.*, **2015**, *17* (24), 15687–15690.
- [152] Heimböckel, R.; Hoffmann, F.; Fröba, M. Insights into the Influence of the Pore Size and Surface Area of Activated Carbons on the Energy Storage of Electric Double Layer Capacitors with a New Potentially Universally Applicable Capacitor Model. *Phys. Chem. Chem. Phys.*, **2019**, *21* (6), 3122–3133.
- [153] Zhou, M.; Gallegos, A.; Liu, K.; Dai, S.; Wu, J. Insights from Machine Learning of Carbon Electrodes for Electric Double Layer Capacitors. *Carbon*, **2020**, *157*, 147–152.
- [154] Su, H.; Lian, C.; Liu, J.; Liu, H. Machine Learning Models for Solvent Effects on Electric Double Layer Capacitance. *Chem. Eng. Sci.*, **2019**, *202*, 186–193.
- [155] Leis, J.; Arulepp, M.; Kuura, A.; Lätt, M.; Lust, E. Electrical Double-Layer Characteristics of Novel Carbide-Derived Carbon Materials. *Carbon*, **2006**, *44* (11), 2122–2129.
- [156] Leis, J.; Arulepp, M.; Perkson, A. Method to Modify Pore Characteristics of Porous Carbon and Porous Carbon Materials Produced by the Method. US20060140846A1.
- [157] Pitman, R. M. Wood Ash Use in Forestry – a Review of the Environmental Impacts. *Forestry*, **2006**, *79* (5), 563–588.
- [158] Lätt, M.; Käärrik, M.; Permann, L.; Kuura, H.; Arulepp, M.; Leis, J. A Structural Influence on the Electrical Double-Layer Characteristics of Al<sub>4</sub>C<sub>3</sub>-Derived Carbon. *J. Solid State Electrochem.*, **2010**, *14* (4), 543–548.
- [159] Liu, C.-F.; Liu, Y.-C.; Yi, T.-Y.; Hu, C.-C. Carbon Materials for High-Voltage Supercapacitors. *Carbon*, **2019**, *145*, 529–548.
- [160] Inagaki, M.; Konno, H.; Tanaike, O. Carbon Materials for Electrochemical Capacitors. *J. Power Sources*, **2010**, *195* (24), 7880–7903.
- [161] Katritzky, A. R.; Lobanov, V.; Karelson, M. *CODESSA Reference Manual*; University of Florida: Gainesville, FL, USA, 1994.
- [162] *R Core Team* (2018). *R: A Language and Environment for Statistical Computing. R Foundation for Statistical Computing, Vienna, Austria.*
- [163] Menéndez, J. A.; Phillips, J.; Xia, B.; Radovic, L. R. On the Modification and Characterization of Chemical Surface Properties of Activated Carbon: In the Search of Carbons with Stable Basic Properties. *Langmuir*, **1996**, *12* (18), 4404–4410.

- [164] Leis, Jaan; Arulepp, M.; Lätt, Marko; Kuura, Helle. A Method of Making the Porous Carbon Material and Porous Carbon Materials Produced by the Method. US7,803,345, 2010.
- [165] Yu, X.; Ruan, D.; Wu, C.; Wang, J.; Shi, Z. Spiro-(1,1')-Bipyrrolidinium Tetrafluoroborate Salt as High Voltage Electrolyte for Electric Double Layer Capacitors. *J. Power Sources*, **2014**, *265*, 309–316.
- [166] Yang, X.; Li, M.; Guo, N.; Yan, M.; Yang, R.; Wang, F. Functionalized Porous Carbon with Appropriate Pore Size Distribution and Open Hole Texture Prepared by H<sub>2</sub> O<sub>2</sub> and EDTA-2Na Treatment of Loofa Sponge and Its Excellent Performance for Supercapacitors. *RSC Adv.*, **2016**, *6* (6), 4365–4376.
- [167] DeRosa, D.; Higashiya, S.; Schulz, A.; Rane-Fondacaro, M.; Haldar, P. High Performance Spiro Ammonium Electrolyte for Electric Double Layer Capacitors. *J. Power Sources*, **2017**, *360*, 41–47.
- [168] Jäckel, N.; Patrick Emge, S.; Krüner, B.; Roling, B.; Presser, V. Quantitative Information about Electrosorption of Ionic Liquids in Carbon Nanopores from Electrochemical Dilatometry and Quartz Crystal Microbalance Measurements. *J. Phys. Chem. C*, **2017**, *121* (35), 19120–19128.
- [169] Krossing, I.; Slattery, J. M.; Daguene, C.; Dyson, P. J.; Oleinikova, A.; Weingärtner, H. Why Are Ionic Liquids Liquid? A Simple Explanation Based on Lattice and Solvation Energies. *J. Am. Chem. Soc.*, **2006**, *128* (41), 13427–13434.
- [170] Nguyen, H. V. T.; Kwak, K.; Lee, K.-K. 1,1-Dimethylpyrrolidinium Tetrafluoroborate as Novel Salt for High-Voltage Electric Double-Layer Capacitors. *Electrochimica Acta*, **2019**, *299*, 98–106.
- [171] Hong, J.; Hwang, B.; Lee, J.; Kim, K. Effects of Cyclic Structure of Ammonium Ions on Capacitance in Electrochemical Double Layer Supercapacitors. *J. Electrochem. Sci. Technol.*, **2017**, *8* (1), 1–6.
- [172] Maletin, Y.; Strelko, V.; Stryzhakova, N.; Zelinsky, S.; Rozhenko, A. B.; Gromadsky, D.; Volkov, V.; Tychina, S.; Gozhenko, O.; Drobny, D. Carbon Based Electrochemical Double Layer Capacitors of Low Internal Resistance. *Energy Environ. Res.*, **2013**, *3* (2), p156.

## SUMMARY IN ESTONIAN

### Nanopoorne süsinik: kontrollitud nanostruktuur ja struktuur-omadussõltuvused

Doktoritöö keskendub nanopoorsetele süsinikmaterjalidele, konkreetselt seoste otsimisele karbiidset päritolu süsinikmaterjalide (CDC) rakenduslikku tähtsust omavate eksperimentaalsete omaduste ja struktuuri vahel ning vastavate statistiliste mitmeparametriseliste korrelatsioonimudelite väljaarendamisele. Uurimus annab põhjaliku ülevaate pooride suuruse jaotuse mõjust elektrilise kaksikkihi mahtvusele ja aitab suunata nii CDC sünteesi protsessi kui ka järeltöötamise tingimusi, et edendada energia salvestamiseks mõeldud süsinikmaterjalide arengut.

Teostatud uurimuse võib tinglikult jagada kahte ossa. Töö esimeses osas käsitletakse peamiselt nanopoorse CDC (ligikaudu 200, eri lähteained TiC, SiC, B<sub>4</sub>C, NbC, ZrC, Mo<sub>2</sub>C, Al<sub>4</sub>C<sub>3</sub>, TiC<sub>1-x</sub>N<sub>x</sub>, TiC<sub>x<1</sub>) mitmesuguseid valmistamis- meetodeid ning uuritakse lähtematerjalide sünteesitingimuste modifikatsioonide ja järeltöötamise mõju süsiniku struktuurile. Teises osas uuritakse eksperimentaalsetele mõõtmistulemustele (CDC poorsuse karakteristikud ja elektrilise kaksikkihi mahtvus) tuginedes kvantitatiivseid nanostruktuur-omadus sõltuvusi (QnSPR) ning koostatakse multilineaarsed võrrandid, mida on võimalik kasutada nanopoorsete süsinikmaterjalide mahtvuse prognoosimiseks ja mahtuvust mõjutavate füüsikalise-keemiliste protsesside selgitamiseks.

Selle töö eksperimentaalsed uuringud näitavad, et metalli karbiidide kõrgtemperatuurisel kloorimisel tekkiv süsiniku struktuur sõltub paljudest erinevatest teguritest: karbiidi keemilisest koostisest, reaktsioonivõimest ja stöhhiomeetriast. Töös leiab kinnistust üldtuntud reegel, et mida kõrgem on sünteesitemperatuur, seda eelistatum on suurema struktuurse korrapäraga (e. grafiitsema) CDC teke. Samuti leiab töös kinnitust seaduspära, et mida väiksem on süsiniku osakaal karbiidis, seda laiema poorijaotusega (ka mesopoorsema) süsinik saadakse. Töös sünteesitud süsinikmaterjalide struktuursete omaduste uurimiseks kasutatud N<sub>2</sub> ja CO<sub>2</sub> adsorptsioonanalüüsi tulemused näitavad, et kitsa poorijaotusega CDC-d on otstarbekas valmistada räni- või titaankarbiidist, kuna laiemat mikropooride jaotust võimaldab pigem nioobium- või tsirkoonium karbiid. Mo<sub>2</sub>C ja B<sub>4</sub>C võimaldavad sobiva sünteesitemperatuuri valiku korral valmistada mikro/mesopoorseid süsinikmaterjale.

Järeltöötamiseks kasutatud füüsikalise aktivatsiooni tulemustest näeme, et nanopoorsete süsinikmaterjalide makrostruktuur aktivatsiooni käigus ei muutu, küll aga on võimalik eripinna väärtust varieerida kuni 1000 ühiku piires (m<sup>2</sup>g<sup>-1</sup>). Uurimus tõestab, et veeauru töötlemisele on vastuvõtlikum korrapäratu amorfse struktuuriga süsinikmaterjal, mille kogupoorsus võib töötlemise käigus suureneda kuni 50%. Lisaks näidatakse, et CDC poorset struktuuri on võimalik oluliselt mõjutada, kasutades lähtekarbiidina biomorfset materjali (näit bio-TiC), mis käesolevas töös sünteesiti titaanoksiidi ja kohalikust lehtpuust valmistatud grill-sõe karbotermilisel taandamisel. Käesolevas töös uuritud nanopoorsete süsinik-

materjalide seas eristus biomorfsest karbiidist valmistatud CDC kõige suurema eripinna ( $\sim 2500 \text{ m}^2\text{g}^{-1}$ ) ja unikaalse, nanopooridesse head massitransporti soodustava morfoloogia poolest.

Uuringu üheks osaks oli ka katalüsaatorite (raua alarühma metallide) toime CDC struktuuri grafitisatsioonile. Tulemused näitavad, et süsinikmaterjalide struktuurne korrapära sõltub oluliselt katalüsaatorite kontsentratsioonist ja sünteesitemperatuuri koostmõjust. Katalüsaatorite juuresolekul on võimalik grafiitse struktuuriga materjale sünteesida madalamatel temperatuuridel ja seeläbi on võimalik materjali poorsust ja struktureeritust samaaegselt muuta laias vahemikus.

Väitekirja teises osas uuritakse eksperimendist tuletatud struktuuritunnuste rakendatavust süsinikmaterjalide kirjeldamiseks QnSPR mudelites. Süsiniku poorsuse parameetritele tuginedes koostati lineaarse regressioonanalüüsi abil prognoosimudelid kirjeldamiseks nanopoorse süsiniku elektrilise kaksikkihi mahtuvust kahes aprotoonses elektrolüüdis: SBP-BF<sub>4</sub> ja TEMA-BF<sub>4</sub> atsetonitriilis. Mudelid sisaldavad mõlema elektrolüüdi korral kolme ühist kirjeldavat struktuuritunnust: teatud suurusega pooride fraktsiooni ruumala, süsiniku eripinna väärtust ja samast süsinikust vormitud elektroodi tihedust, mis omakorda sõltub süsiniku osakeste suurusest ja elektroodi valmistamismeetodist.

Uuringute tulemused on verstepostiks, et N<sub>2</sub> ja CO<sub>2</sub> adsorptsiooni isotermidest arvatud eksperimendist tuletatud struktuuritunnused võimaldavad edukalt konstrueerida QnSPR mudeleid, mis kirjeldavad ja prognoosivad suure täpsusega struktuuriliselt mittehomoogeensete nanopoorsete süsinikmaterjalide erimahtuvust.

Kõigil QnSPR mudelites kaasatud süsiniku struktuuri kirjeldatavatel tunnustel on selge füüsikalise-keemiline seos modelleeritud omadusega (elektrilise kaksikkihi mahtuvusega) ja nad selgitavad seotud interaktsioonimehhanisme. Saadud tulemused näitavad, et fikseeritud katsetingimuste korral sõltub nanopoorse süsinikelektroodi erimahtuvus peamiselt süsinikmaterjali efektiivsest pindalast, mis tuletatud QnSPR mudelites väljendub kombinatsioonina materjali kogupindalast ja elektrolüüdi iooni mõõtmetega lähedase suurusega süsiniku pooride summaarsest ruumalast.

Kokkuvõtteks saame öelda, et esmakordselt õnnestus eksperimendist tuletatud struktuuritunnuste abil konstrueerida mitmeparameetrilised matemaatilised mudelid poorse süsiniku rakenduslikult olulise füüsikalise omaduse kirjeldamiseks ja prognoosimiseks. Töös tuletatud QnSPR mudelid sobivad nanopoorse süsiniku elektrilise kaksikkihi mahtuvuse kirjeldamiseks nii täielikult mikropoorset kui ka mikro-mesopoorset pooride jaotust omavate süsinikmaterjalide korral, peale selle võimaldavad nad täpselt ennustada elektrilise kaksikkihi mahtuvust.

## ACKNOWLEDGEMENTS

Firstly, I would like to express my sincere gratitude to my supervisors, Dr. Jaan Leis and Dr. Uko Maran for their advice, support and patience throughout the studies. I am grateful to all my colleagues, without your support this work would not have been completed. Very special thanks go to Dr. Mati Arulepp for his guidance on electrochemical studies and to Mrs. Helle Kuura. Helle, heartfelt thanks to you for the fact that you were always there, ready to listen to me and always support. I would like to thank all the co-authors for their contribution to the publications.

I am most grateful to my sons and husband for their love and support. Thank you for always being with me during this intense time.

This work has been financially supported by Estonian Ministry for Education and Research (grant ID: IUT34-14), European Regional Development Fund – European Commission (Foundation Archimedes, grant IDs: 3.2.1201.13-0021; TK143 “Center of Excellence in Molecular Cell Engineering”) and, the EU FP7 project HESCAP (grant ID: 241405).



## **PUBLICATIONS**

## CURRICULUM VITAE

**Nimi:** Maike Käärik  
**Date of birth:** February 15<sup>th</sup>, 1976, Paide, Estonia  
**Citizenship:** Estonian  
**Address:** Institute of Chemistry, University of Tartu, Ravila 14A, 50411, Tartu, Estonia  
**E-mail:** maike.kaarik@gmail.com

### Education:

2015–... University of Tartu, Molecular Engineering, Phd student  
1999–2008 University of Tartu, Faculty of Physics and Chemistry, MSc  
1998–1999 University of Tartu, Faculty of Physics and Chemistry, Teacher training  
1994–1998 University of Tartu, Faculty of Physics and Chemistry, BSc

### Professional employment:

2009–... University of Tartu, Institute of Chemistry, Research Fellow  
2012–2016 Skeleton Technologies OÜ, Researcher-Technologist  
2007–2008 University of Tartu, Institute of Chemistry, Chemist  
2008–2009 Carbon Nanotech OÜ, Technologist  
2000–2008 Tartu Tehnoloogiad OÜ, Chemist-Technologist  
1997–2000 Akrom-Ex OÜ, Assistant

### Scientific publications:

1. **Käärik, M.**; Arulepp, M.; Käärik, M.; Maran, U.; Leis, J. Characterization and Prediction of Double-Layer Capacitance of Nanoporous Carbon Materials Using the Quantitative Nano-Structure-Property Relationship Approach Based on Experimentally Determined Porosity Descriptors. *Carbon*, **2020**, *158*, 494–504.
2. Lüsi, M.; Erikson, H.; Sarapuu, A.; Merisalu, M.; Rähn, M.; Treshchalov, A.; Paiste, P.; **Käärik, M.**; Leis, J.; Sammelselg, V.; et al. Electroreduction of Oxygen on Carbide-Derived Carbon Supported Pd Catalysts. *ChemElectroChem*, **2020**, *7* (2), 546–554.
3. Praats, R.; **Käärik, M.**; Kikas, A.; Kisand, V.; Aruväli, J.; Paiste, P.; Merisalu, M.; Leis, J.; Sammelselg, V.; Zagal, J. H.; et al. Electrocatalytic Oxygen Reduction Reaction on Iron Phthalocyanine-Modified Carbide-Derived Carbon/Carbon Nanotube Composite Electrocatalysts. *Electrochimica Acta*, **2020**, *334*, 135575.
4. Malmberg, S.; Arulepp, M.; Savest, N.; Tarasova, E.; Vassiljeva, V.; Krasnou, I.; **Käärik, M.**; Mikli, V.; Krumme, A. Directly Electrospun Electrodes for Electrical Double-Layer Capacitors from Carbide-Derived Carbon. *J. Electroanal. Chem.*, **2020**, *103*, 103396.

5. **Käärrik, M.**; Arulepp, M.; Kook, M.; Kozlova, J.; Ritslaid, P.; Aruväli, J.; Mäeorg, U.; Sammelseg, V.; Leis, J. High-Performance Microporous Carbon from Deciduous Wood-Origin Metal Carbide. *Microporous Mesoporous Mater.*, **2019**, *278*, 14–22.
6. Praats, R.; Kruusenberg, I.; **Käärrik, M.**; Joost, U.; Aruväli, J.; Paiste, P.; Saar, R.; Rauwel, P.; Kook, M.; Leis, J.; et al. Electroreduction of Oxygen in Alkaline Solution on Iron Phthalocyanine Modified Carbide-Derived Carbons. *Electrochimica Acta*, **2019**, *299*, 999–1010.
7. Ping, K.; Alam, M.; **Käärrik, M.**; Leis, J.; Kongi, N.; Järving, I.; Starkov, P. Surveying Iron–Organic Framework TAL-1-Derived Materials in Ligandless Heterogeneous Oxidative Catalytic Transformations of Alkylarenes. *Synlett*, **2019**, *30* (13), 1536–1540.
8. Ratso, S.; **Käärrik, M.**; Kook, M.; Paiste, P.; Aruväli, J.; Vlassov, S.; Kisand, V.; Leis, J.; Kannan, A. M.; Tammeveski, K. High Performance Catalysts Based on Fe/N Co-Doped Carbide-Derived Carbon and Carbon Nanotube Composites for Oxygen Reduction Reaction in Acid Media. *Int. J. Hydrog. Energy*, **2019**, *44* (25), 12636–12648.
9. Bhowmick, G. D.; Kibena-Pöldsepp, E.; Matisen, L.; Merisalu, M.; Kook, M.; **Käärrik, M.**; Leis, J.; Sammelseg, V.; Ghangrekar, M. M.; Tammeveski, K. Multi-Walled Carbon Nanotube and Carbide-Derived Carbon Supported Metal Phthalocyanines as Cathode Catalysts for Microbial Fuel Cell Applications. *Sustain. Energy Fuels*, **2019**, *3* (12), 3525–3537.
10. Ratso, S.; Sougrati, M. T.; **Käärrik, M.**; Merisalu, M.; Rahn, M.; Kisand, V.; Kikas, A.; Paiste, P.; Leis, J.; Sammelseg, V.; et al. Effect of Ball-Milling on the Oxygen Reduction Reaction Activity of Iron and Nitrogen Co-Doped Carbide-Derived Carbon Catalysts in Acid Media. *ACS Appl. Energy Mater.*, **2019**, *2* (11), 7952–7962.
11. **Käärrik, M.**; Arulepp, M.; Kook, M.; Mäeorg, U.; Kozlova, J.; Sammelseg, V.; Perkson, A.; Leis, J. Characterisation of Steam-Treated Nanoporous Carbide-Derived Carbon of TiC Origin: Structure and Enhanced Electrochemical Performance. *J. Porous Mater.*, **2017**, *25* (4), 1057–1070
12. Ratso, S.; Kruusenberg, I.; **Käärrik, M.**; Kook, M.; Puust, L.; Saar, R.; Leis, J.; Tammeveski, K. Highly Efficient Transition Metal and Nitrogen Co-Doped Carbide-Derived Carbon Electrocatalysts for Anion Exchange Membrane Fuel Cells. *J. Power Sources*, **2018**, *375*, 233–243.
13. Ratso, S.; **Käärrik, M.**; Kook, M.; Paiste, P.; Kisand, V.; Vlassov, S.; Leis, J.; Tammeveski, K. Iron and Nitrogen Co-Doped Carbide-Derived Carbon and Carbon Nanotube Composite Catalysts for Oxygen Reduction Reaction. *ChemElectroChem*, **2018**, *5* (14), 1827–1836. <https://doi.org/10.1002/celec.201800132>.
14. Kisand, K.; Sarapuu, A.; Peikolainen, A.-L.; Seemen, H.; Kook, M.; **Käärrik, M.**; Leis, J.; Sammelseg, V.; Tammeveski, K. Oxygen Reduction on Fe- and Co-Containing Nitrogen-Doped Nanocarbons. *ChemElectroChem*, **2018**, *5* (14), 2002–2009.

15. Ratso, S.; Ranjbar Sahraie, N.; Sougrati, M. T.; **Käärrik, M.**; Kook, M.; Saar, R.; Paiste, P.; Jia, Q.; Leis, J.; Mukerjee, S.; et al. Synthesis of Highly-Active Fe–N–C Catalysts for PEMFC with Carbide-Derived Carbons. *J. Mater. Chem. A*, **2018**, *6* (30), 14663–14674.
16. Sibul, R.; Kibena-Pöldsepp, E.; Ratso, S.; Kook, M.; **Käärrik, M.**; Merisalu, M.; Paiste, P.; Leis, J.; Sammelselg, V.; Tammeveski, K. Nitrogen-Doped Carbon-Based Electrocatalysts Synthesised by Ball-Milling. *Electrochem. Commun.*, **2018**, *93*, 39–43.
17. **Käärrik, M.**; Maran, U.; Arulepp, M.; Perkson, A.; Leis, J. Quantitative Nano-Structure–Property Relationships for the Nanoporous Carbon: Predicting the Performance of Energy Storage Materials. *ACS Appl. Energy Mater.*, **2018**, *1* (8), 4016–4024.
18. Linge, J. M.; Erikson, H.; Merisalu, M.; Matisen, L.; **Käärrik, M.**; Leis, J.; Sammelselg, V.; Aruväli, J.; Kaljuvee, T.; Tammeveski, K. Oxygen Reduction on Silver Nanoparticles Supported on Carbide-Derived Carbons. *J. Electrochem. Soc.*, **2018**, *165* (14), F1199–F1205.
19. Ratso, S.; Kruusenberg, I.; **Käärrik, M.**; Kook, M.; Saar, R.; Pärs, M.; Leis, J.; Tammeveski, K. Highly Efficient Nitrogen-Doped Carbide-Derived Carbon Materials for Oxygen Reduction Reaction in Alkaline Media. *Carbon*, **2017**, *113*, 159–169.
20. Ratso, S.; Kruusenberg, I.; **Käärrik, M.**; Kook, M.; Saar, R.; Kanninen, P.; Kallio, T.; Leis, J.; Tammeveski, K. Transition Metal-Nitrogen Co-Doped Carbide-Derived Carbon Catalysts for Oxygen Reduction Reaction in Alkaline Direct Methanol Fuel Cell. *Appl. Catal. B Environ.*, **2017**, *219*, 276–286.
21. Leis, J.; Torop, J.; **Käärrik, M.**; Aabloo, A.; Arulepp, M.; Madiberk, T.; Ehin, R. Nanotuned carbide-derived carbon as a potential low-voltage actuator in lab-on-chip applications for blood analysis and point-of-care medicine. *Journal for Clinical Studies*, **2013**, *5* (3), 34–37.
22. Leis, J.; Arulepp, M.; **Käärrik, M.**; Perkson, A. The Effect of Mo<sub>2</sub>C Derived Carbon Pore Size on the Electrical Double-Layer Characteristics in Propylene Carbonate-Based Electrolyte. *Carbon*, **2010**, *48* (14), 4001–4008.
23. Lätt, M.; **Käärrik, M.**; Permann, L.; Kuura, H.; Arulepp, M.; Leis, J. A Structural Influence on the Electrical Double-Layer Characteristics of Al<sub>4</sub>C<sub>3</sub>-Derived Carbon. *J. Solid State Electrochem.*, **2010**, *14* (4), 543–548.
24. **Käärrik, M.**; Arulepp, M.; Karelson, M.; Leis, J. The Effect of Graphitization Catalyst on the Structure and Porosity of SiC Derived Carbons. *Carbon*, **2008**, *46* (12), 1579–1587.
25. Pentchuk, J.; Alumaa, P.; Ivask, J.; **Käärrik, M.** Separation of Calcium and Magnesium Ions by Ion Chromatography with HEMA-EDMA column. *Proceedings of the Estonian Academy of Sciences. Chemistry*, **2005**, *54* (4), 189–193

26. Perkson, A.; Leis, J.; Arulepp, M.; **Käärrik, M.**; Urbonaite, S.; Svensson, G. Barrel-like Carbon Nanoparticles from Carbide by Catalyst Assisted Chlorination. *Carbon*, **2003**, *41* (9), 1729–1735.
27. Leis, J.; Perkson, A.; Arulepp, M.; **Käärrik, M.**; Svensson, G. Carbon Nanostructures Produced by Chlorinating Aluminium Carbide. *Carbon*, **2001**, *39* (13), 2043–2048.

### **Industrial property**

1. Post-activation of nanoporous carbon for energy storage; Omanikud: Skeleton Technologies OÜ; Autorid: Jaan Leis, **Maike Käärrik**, Anti Perkson, Mati Arulepp; Priority number: 62/343,180; Priority date: 31.05.2016.
2. Method of synthesis of electrocatalytically active porous carbonmaterial for oxygen reduction in low-temperature fuel cells; Omanikud: Skeleton Technologies OÜ; Autorid: Jaan Leis, Mati Arulepp, **Maike Käärrik**, Anti Perkson; Priority number: 61/510,358; Priority date: 21.07.2011.
3. A method for production of carbon composite material with modified microstructure and a carbon composite material produced thereof; Omanikud: Carbon.ee OÜ; Autorid: Jaan Leis, Mati Arulepp, Marko Lätt, Helle Kuura, Andres Kuura, **Maike Käärrik**; Priority number: P200800008; Priority date: 14.02.2008

# ELULOOKIRJELDUS

**Nimi:** Maike Käärrik  
**Sünniaeg:** 15. veebruar 1976, Paide, Eesti  
**Kodakondsus:** Eesti  
**Aadress:** Keemia instituut, Tartu Ülikool, Ravila 14A, 50411, Tartu, Eesti  
**E-mail:** maike.kaarik@gmail.com

## Haridus:

2015–... doktoriõpe, Tartu Ülikool, loodus- ja täppisteaduste valdkond, molekulaartehnoloogia  
1999–2008 magistriõpe, Tartu Ülikool, loodus- ja tehnoloogiateaduskond, MSc füüsikalise ja analüütilise keemia erialal  
1998–1999 õpetajakoolitus, Tartu Ülikool, füüsika-keemia teaduskond  
1994–1998 bakalaureuseõpe, Tartu Ülikool, füüsika-keemia teaduskond, BSc keemia erialal

## Teenistuskäik:

2009–... Tartu Ülikool, loodus- ja täppisteaduste valdkond, keemia instituut, teadur  
2012–2016 Skeleton Technologies OÜ, teadur-tehnoloog  
2007–2008 Tartu Ülikool, Loodus- ja tehnoloogiateaduskond, keemia instituut, keemik  
2008–2009 Carbon Nanotech OÜ, tehnoloog  
2000–2008 Tartu Tehnoloogiad OÜ, keemik-tehnoloog  
1997–2000 Akrom-Ex OÜ, assistent

## Teaduspublikatsioonid:

1. **Käärrik, M.**; Arulepp, M.; Käärrik, M.; Maran, U.; Leis, J. Characterization and Prediction of Double-Layer Capacitance of Nanoporous Carbon Materials Using the Quantitative Nano-Structure-Property Relationship Approach Based on Experimentally Determined Porosity Descriptors. *Carbon*, **2020**, *158*, 494–504.
2. Lüsi, M.; Erikson, H.; Sarapuu, A.; Merisalu, M.; Rähn, M.; Treshchalov, A.; Paiste, P.; **Käärrik, M.**; Leis, J.; Sammelselg, V.; et al. Electroreduction of Oxygen on Carbide-Derived Carbon Supported Pd Catalysts. *ChemElectroChem*, **2020**, *7* (2), 546–554.
3. Praats, R.; **Käärrik, M.**; Kikas, A.; Kisand, V.; Aruväli, J.; Paiste, P.; Merisalu, M.; Leis, J.; Sammelselg, V.; Zagal, J. H.; et al. Electrocatalytic Oxygen Reduction Reaction on Iron Phthalocyanine-Modified Carbide-Derived Carbon/Carbon Nanotube Composite Electrocatalysts. *Electrochimica Acta*, **2020**, *334*, 135575.

4. Malmberg, S.; Arulepp, M.; Savest, N.; Tarasova, E.; Vassiljeva, V.; Krasnou, I.; **Käärrik, M.**; Mikli, V.; Krumme, A. Directly Electrospun Electrodes for Electrical Double-Layer Capacitors from Carbide-Derived Carbon. *J. Electrostat.*, **2020**, *103*, 103396.
5. **Käärrik, M.**; Arulepp, M.; Kook, M.; Kozlova, J.; Ritslaid, P.; Aruväli, J.; Mäeorg, U.; Sammelselg, V.; Leis, J. High-Performance Microporous Carbon from Deciduous Wood-Origin Metal Carbide. *Microporous Mesoporous Mater.*, **2019**, *278*, 14–22.
6. Praats, R.; Kruusenberg, I.; **Käärrik, M.**; Joost, U.; Aruväli, J.; Paiste, P.; Saar, R.; Rauwel, P.; Kook, M.; Leis, J.; et al. Electroreduction of Oxygen in Alkaline Solution on Iron Phthalocyanine Modified Carbide-Derived Carbons. *Electrochimica Acta*, **2019**, *299*, 999–1010.
7. Ping, K.; Alam, M.; **Käärrik, M.**; Leis, J.; Kongi, N.; Järving, I.; Starkov, P. Surveying Iron–Organic Framework TAL-1-Derived Materials in Ligandless Heterogeneous Oxidative Catalytic Transformations of Alkylarenes. *Synlett*, **2019**, *30* (13), 1536–1540.
8. Ratso, S.; **Käärrik, M.**; Kook, M.; Paiste, P.; Aruväli, J.; Vlassov, S.; Kisand, V.; Leis, J.; Kannan, A. M.; Tammeveski, K. High Performance Catalysts Based on Fe/N Co-Doped Carbide-Derived Carbon and Carbon Nanotube Composites for Oxygen Reduction Reaction in Acid Media. *Int. J. Hydrog. Energy*, **2019**, *44* (25), 12636–12648.
9. Bhowmick, G. D.; Kibena-Pöldsepp, E.; Matisen, L.; Merisalu, M.; Kook, M.; **Käärrik, M.**; Leis, J.; Sammelselg, V.; Ghangrekar, M. M.; Tammeveski, K. Multi-Walled Carbon Nanotube and Carbide-Derived Carbon Supported Metal Phthalocyanines as Cathode Catalysts for Microbial Fuel Cell Applications. *Sustain. Energy Fuels*, **2019**, *3* (12), 3525–3537.
10. Ratso, S.; Sougrati, M. T.; **Käärrik, M.**; Merisalu, M.; Rähn, M.; Kisand, V.; Kikas, A.; Paiste, P.; Leis, J.; Sammelselg, V.; et al. Effect of Ball-Milling on the Oxygen Reduction Reaction Activity of Iron and Nitrogen Co-Doped Carbide-Derived Carbon Catalysts in Acid Media. *ACS Appl. Energy Mater.*, **2019**, *2* (11), 7952–7962.
11. **Käärrik, M.**; Arulepp, M.; Kook, M.; Mäeorg, U.; Kozlova, J.; Sammelselg, V.; Perkson, A.; Leis, J. Characterisation of Steam-Treated Nanoporous Carbide-Derived Carbon of TiC Origin: Structure and Enhanced Electrochemical Performance. *J. Porous Mater.*, **2017**, *25* (4), 1057–1070.
12. Ratso, S.; Kruusenberg, I.; **Käärrik, M.**; Kook, M.; Puust, L.; Saar, R.; Leis, J.; Tammeveski, K. Highly Efficient Transition Metal and Nitrogen Co-Doped Carbide-Derived Carbon Electrocatalysts for Anion Exchange Membrane Fuel Cells. *J. Power Sources*, **2018**, *375*, 233–243.
13. Ratso, S.; **Käärrik, M.**; Kook, M.; Paiste, P.; Kisand, V.; Vlassov, S.; Leis, J.; Tammeveski, K. Iron and Nitrogen Co-Doped Carbide-Derived Carbon and Carbon Nanotube Composite Catalysts for Oxygen Reduction Reaction. *ChemElectroChem*, **2018**, *5* (14), 1827–1836. <https://doi.org/10.1002/celec.201800132>.

14. Kisand, K.; Sarapuu, A.; Peikolainen, A.-L.; Seemen, H.; Kook, M.; **Käärrik, M.**; Leis, J.; Sammelselg, V.; Tammeveski, K. Oxygen Reduction on Fe- and Co-Containing Nitrogen-Doped Nanocarbons. *ChemElectro Chem*, **2018**, *5* (14), 2002–2009.
15. Ratso, S.; Ranjbar Sahraie, N.; Sougrati, M. T.; **Käärrik, M.**; Kook, M.; Saar, R.; Paiste, P.; Jia, Q.; Leis, J.; Mukerjee, S.; et al. Synthesis of Highly-Active Fe–N–C Catalysts for PEMFC with Carbide-Derived Carbons. *J. Mater. Chem. A*, **2018**, *6* (30), 14663–14674.
16. Sibul, R.; Kibena-Pöldsepp, E.; Ratso, S.; Kook, M.; **Käärrik, M.**; Merisalu, M.; Paiste, P.; Leis, J.; Sammelselg, V.; Tammeveski, K. Nitrogen-Doped Carbon-Based Electrocatalysts Synthesised by Ball-Milling. *Electrochem. Commun.*, **2018**, *93*, 39–43.
17. **Käärrik, M.**; Maran, U.; Arulepp, M.; Perkson, A.; Leis, J. Quantitative Nano-Structure–Property Relationships for the Nanoporous Carbon: Predicting the Performance of Energy Storage Materials. *ACS Appl. Energy Mater.*, **2018**, *1* (8), 4016–4024.
18. Linge, J. M.; Erikson, H.; Merisalu, M.; Matisen, L.; **Käärrik, M.**; Leis, J.; Sammelselg, V.; Aruväli, J.; Kaljuvee, T.; Tammeveski, K. Oxygen Reduction on Silver Nanoparticles Supported on Carbide-Derived Carbons. *J. Electrochem. Soc.*, **2018**, *165* (14), F1199–F1205.
19. Ratso, S.; Kruusenberg, I.; **Käärrik, M.**; Kook, M.; Saar, R.; Pärs, M.; Leis, J.; Tammeveski, K. Highly Efficient Nitrogen-Doped Carbide-Derived Carbon Materials for Oxygen Reduction Reaction in Alkaline Media. *Carbon*, **2017**, *113*, 159–169.
20. Ratso, S.; Kruusenberg, I.; **Käärrik, M.**; Kook, M.; Saar, R.; Kanninen, P.; Kallio, T.; Leis, J.; Tammeveski, K. Transition Metal-Nitrogen Co-Doped Carbide-Derived Carbon Catalysts for Oxygen Reduction Reaction in Alkaline Direct Methanol Fuel Cell. *Appl. Catal. B Environ.*, **2017**, *219*, 276–286.
21. Leis, J.; Torop, J.; **Käärrik, M.**; Aabloo, A.; Arulepp, M.; Madiberk, T.; Ehin, R. Nanotuned carbide-derived carbon as a potential low-voltage actuator in lab-on-chip applications for blood analysis and point-of-care medicine. *Journal for Clinical Studies*, **2013**, *5* (3), 34–37.
22. Leis, J.; Arulepp, M.; **Käärrik, M.**; Perkson, A. The Effect of Mo<sub>2</sub>C Derived Carbon Pore Size on the Electrical Double-Layer Characteristics in Propylene Carbonate-Based Electrolyte. *Carbon*, **2010**, *48* (14), 4001–4008.
23. Lätt, M.; **Käärrik, M.**; Permann, L.; Kuura, H.; Arulepp, M.; Leis, J. A Structural Influence on the Electrical Double-Layer Characteristics of Al<sub>4</sub>C<sub>3</sub>-Derived Carbon. *J. Solid State Electrochem.*, **2010**, *14* (4), 543–548.
24. **Käärrik, M.**; Arulepp, M.; Karelson, M.; Leis, J. The Effect of Graphitization Catalyst on the Structure and Porosity of SiC Derived Carbons. *Carbon*, **2008**, *46* (12), 1579–1587.

25. Pentchuk, J.; Alumaa, P.; Ivask, J.; **Käärrik, M.** Separation of Calcium and Magnesium Ions by Ion Chromatography with HEMA-EDMA column. *Proceedings of the Estonian Academy of Sciences. Chemistry*, **2005**, 54 (4), 189–193
26. Perkson, A.; Leis, J.; Arulepp, M.; **Käärrik, M.**; Urbonaite, S.; Svensson, G. Barrel-like Carbon Nanoparticles from Carbide by Catalyst Assisted Chlorination. *Carbon*, **2003**, 41 (9), 1729–1735.
27. Leis, J.; Perkson, A.; Arulepp, M.; **Käärrik, M.**; Svensson, G. Carbon Nanostructures Produced by Chlorinating Aluminium Carbide. *Carbon*, **2001**, 39 (13), 2043–2048.

### **Tööstusomand**

1. Patentne leiutis: Post-activation of nanoporous carbon for energy storage; Omanikud: Skeleton Technologies OÜ; Autorid: Jaan Leis, **Maike Käärrik**, Anti Perkson, Mati Arulepp; Prioriteedi number: 62/343,180; Prioriteedi kuupäev: 31.05.2016.
2. Patentne leiutis: Method of synthesis of electrocatalytically active porous carbonmaterial for oxygen reduction in low-temperature fuel cells; Omanikud: Skeleton Technologies OÜ; Autorid: Jaan Leis, Mati Arulepp, **Maike Käärrik**, Anti Perkson; Prioriteedi number: 61/510,358; Prioriteedi kuupäev: 21.07.2011.
3. Patentne leiutis: A method for production of carbon composite material with modified microstructure and a carbon composite material produced thereof; Omanikud: Carbon.ee OÜ; Autorid: Jaan Leis, Mati Arulepp, Marko Lätt, Helle Kuura, Andres Kuura, **Maike Käärrik**; Prioriteedi number: P200800008; Prioriteedi kuupäev: 14.02.2008.

## DISSERTATIONES CHIMICAE UNIVERSITATIS TARTUENSIS

1. **Toomas Tamm.** Quantum-chemical simulation of solvent effects. Tartu, 1993, 110 p.
2. **Peeter Burk.** Theoretical study of gas-phase acid-base equilibria. Tartu, 1994, 96 p.
3. **Victor Lobanov.** Quantitative structure-property relationships in large descriptor spaces. Tartu, 1995, 135 p.
4. **Vahur Mäemets.** The  $^{17}\text{O}$  and  $^1\text{H}$  nuclear magnetic resonance study of  $\text{H}_2\text{O}$  in individual solvents and its charged clusters in aqueous solutions of electrolytes. Tartu, 1997, 140 p.
5. **Andrus Metsala.** Microcanonical rate constant in nonequilibrium distribution of vibrational energy and in restricted intramolecular vibrational energy redistribution on the basis of slater's theory of unimolecular reactions. Tartu, 1997, 150 p.
6. **Uko Maran.** Quantum-mechanical study of potential energy surfaces in different environments. Tartu, 1997, 137 p.
7. **Alar Jänes.** Adsorption of organic compounds on antimony, bismuth and cadmium electrodes. Tartu, 1998, 219 p.
8. **Kaido Tammeveski.** Oxygen electroreduction on thin platinum films and the electrochemical detection of superoxide anion. Tartu, 1998, 139 p.
9. **Ivo Leito.** Studies of Brønsted acid-base equilibria in water and non-aqueous media. Tartu, 1998, 101 p.
10. **Jaan Leis.** Conformational dynamics and equilibria in amides. Tartu, 1998, 131 p.
11. **Toonika Rinke.** The modelling of amperometric biosensors based on oxidoreductases. Tartu, 2000, 108 p.
12. **Dmitri Panov.** Partially solvated Grignard reagents. Tartu, 2000, 64 p.
13. **Kaja Orupõld.** Treatment and analysis of phenolic wastewater with microorganisms. Tartu, 2000, 123 p.
14. **Jüri Ivask.** Ion Chromatographic determination of major anions and cations in polar ice core. Tartu, 2000, 85 p.
15. **Lauri Vares.** Stereoselective Synthesis of Tetrahydrofuran and Tetrahydropyran Derivatives by Use of Asymmetric Horner-Wadsworth-Emmons and Ring Closure Reactions. Tartu, 2000, 184 p.
16. **Martin Lepiku.** Kinetic aspects of dopamine  $\text{D}_2$  receptor interactions with specific ligands. Tartu, 2000, 81 p.
17. **Katrin Sak.** Some aspects of ligand specificity of  $\text{P2Y}$  receptors. Tartu, 2000, 106 p.
18. **Vello Pällin.** The role of solvation in the formation of iotsitch complexes. Tartu, 2001, 95 p.
19. **Katrin Kollist.** Interactions between polycyclic aromatic compounds and humic substances. Tartu, 2001, 93 p.

20. **Ivar Koppel.** Quantum chemical study of acidity of strong and superstrong Brønsted acids. Tartu, 2001, 104 p.
21. **Viljar Pihl.** The study of the substituent and solvent effects on the acidity of OH and CH acids. Tartu, 2001, 132 p.
22. **Natalia Palm.** Specification of the minimum, sufficient and significant set of descriptors for general description of solvent effects. Tartu, 2001, 134 p.
23. **Sulev Sild.** QSPR/QSAR approaches for complex molecular systems. Tartu, 2001, 134 p.
24. **Ruslan Petrukhin.** Industrial applications of the quantitative structure-property relationships. Tartu, 2001, 162 p.
25. **Boris V. Rogovoy.** Synthesis of (benzotriazolyl)carboximidamides and their application in relations with *N*- and *S*-nucleophiles. Tartu, 2002, 84 p.
26. **Koit Herodes.** Solvent effects on UV-vis absorption spectra of some solvatochromic substances in binary solvent mixtures: the preferential solvation model. Tartu, 2002, 102 p.
27. **Anti Perkson.** Synthesis and characterisation of nanostructured carbon. Tartu, 2002, 152 p.
28. **Ivari Kaljurand.** Self-consistent acidity scales of neutral and cationic Brønsted acids in acetonitrile and tetrahydrofuran. Tartu, 2003, 108 p.
29. **Karmen Lust.** Adsorption of anions on bismuth single crystal electrodes. Tartu, 2003, 128 p.
30. **Mare Piirsalu.** Substituent, temperature and solvent effects on the alkaline hydrolysis of substituted phenyl and alkyl esters of benzoic acid. Tartu, 2003, 156 p.
31. **Meeri Sassian.** Reactions of partially solvated Grignard reagents. Tartu, 2003, 78 p.
32. **Tarmo Tamm.** Quantum chemical modelling of polypyrrole. Tartu, 2003. 100 p.
33. **Erik Teinmaa.** The environmental fate of the particulate matter and organic pollutants from an oil shale power plant. Tartu, 2003. 102 p.
34. **Jaana Tammiku-Taul.** Quantum chemical study of the properties of Grignard reagents. Tartu, 2003. 120 p.
35. **Andre Lomaka.** Biomedical applications of predictive computational chemistry. Tartu, 2003. 132 p.
36. **Kostyantyn Kirichenko.** Benzotriazole – Mediated Carbon–Carbon Bond Formation. Tartu, 2003. 132 p.
37. **Gunnar Nurk.** Adsorption kinetics of some organic compounds on bismuth single crystal electrodes. Tartu, 2003, 170 p.
38. **Mati Arulepp.** Electrochemical characteristics of porous carbon materials and electrical double layer capacitors. Tartu, 2003, 196 p.
39. **Dan Cornel Fara.** QSPR modeling of complexation and distribution of organic compounds. Tartu, 2004, 126 p.
40. **Riina Mahlapuu.** Signalling of galanin and amyloid precursor protein through adenylate cyclase. Tartu, 2004, 124 p.

41. **Mihkel Kerikmäe.** Some luminescent materials for dosimetric applications and physical research. Tartu, 2004, 143 p.
42. **Jaanus Kruusma.** Determination of some important trace metal ions in human blood. Tartu, 2004, 115 p.
43. **Urmas Johanson.** Investigations of the electrochemical properties of polypyrrole modified electrodes. Tartu, 2004, 91 p.
44. **Kaido Sillar.** Computational study of the acid sites in zeolite ZSM-5. Tartu, 2004, 80 p.
45. **Aldo Oras.** Kinetic aspects of dATP $\alpha$ S interaction with P2Y<sub>1</sub> receptor. Tartu, 2004, 75 p.
46. **Erik Mölder.** Measurement of the oxygen mass transfer through the air-water interface. Tartu, 2005, 73 p.
47. **Thomas Thomberg.** The kinetics of electroreduction of peroxodisulfate anion on cadmium (0001) single crystal electrode. Tartu, 2005, 95 p.
48. **Olavi Loog.** Aspects of condensations of carbonyl compounds and their imine analogues. Tartu, 2005, 83 p.
49. **Siim Salmar.** Effect of ultrasound on ester hydrolysis in aqueous ethanol. Tartu, 2006, 73 p.
50. **Ain Uustare.** Modulation of signal transduction of heptahelical receptors by other receptors and G proteins. Tartu, 2006, 121 p.
51. **Sergei Yurchenko.** Determination of some carcinogenic contaminants in food. Tartu, 2006, 143 p.
52. **Kaido Tämm.** QSPR modeling of some properties of organic compounds. Tartu, 2006, 67 p.
53. **Olga Tšubrik.** New methods in the synthesis of multisubstituted hydrazines. Tartu, 2006, 183 p.
54. **Lilli Sooväli.** Spectrophotometric measurements and their uncertainty in chemical analysis and dissociation constant measurements. Tartu, 2006, 125 p.
55. **Eve Koort.** Uncertainty estimation of potentiometrically measured pH and pK<sub>a</sub> values. Tartu, 2006, 139 p.
56. **Sergei Kopanchuk.** Regulation of ligand binding to melanocortin receptor subtypes. Tartu, 2006, 119 p.
57. **Silvar Kallip.** Surface structure of some bismuth and antimony single crystal electrodes. Tartu, 2006, 107 p.
58. **Kristjan Saal.** Surface silanization and its application in biomolecule coupling. Tartu, 2006, 77 p.
59. **Tanel Tätte.** High viscosity Sn(OBu)<sub>4</sub> oligomeric concentrates and their applications in technology. Tartu, 2006, 91 p.
60. **Dimitar Atanasov Dobchev.** Robust QSAR methods for the prediction of properties from molecular structure. Tartu, 2006, 118 p.
61. **Hannes Hagu.** Impact of ultrasound on hydrophobic interactions in solutions. Tartu, 2007, 81 p.
62. **Rutha Jäger.** Electroreduction of peroxodisulfate anion on bismuth electrodes. Tartu, 2007, 142 p.

63. **Kaido Viht.** Immobilizable bisubstrate-analogue inhibitors of basophilic protein kinases: development and application in biosensors. Tartu, 2007, 88 p.
64. **Eva-Ingrid Rõõm.** Acid-base equilibria in nonpolar media. Tartu, 2007, 156 p.
65. **Sven Tamp.** DFT study of the cesium cation containing complexes relevant to the cesium cation binding by the humic acids. Tartu, 2007, 102 p.
66. **Jaak Nerut.** Electroreduction of hexacyanoferrate(III) anion on Cadmium (0001) single crystal electrode. Tartu, 2007, 180 p.
67. **Lauri Jalukse.** Measurement uncertainty estimation in amperometric dissolved oxygen concentration measurement. Tartu, 2007, 112 p.
68. **Aime Lust.** Charge state of dopants and ordered clusters formation in CaF<sub>2</sub>:Mn and CaF<sub>2</sub>:Eu luminophors. Tartu, 2007, 100 p.
69. **Iiris Kahn.** Quantitative Structure-Activity Relationships of environmentally relevant properties. Tartu, 2007, 98 p.
70. **Mari Reinik.** Nitrates, nitrites, N-nitrosamines and polycyclic aromatic hydrocarbons in food: analytical methods, occurrence and dietary intake. Tartu, 2007, 172 p.
71. **Heili Kasuk.** Thermodynamic parameters and adsorption kinetics of organic compounds forming the compact adsorption layer at Bi single crystal electrodes. Tartu, 2007, 212 p.
72. **Erki Enkvist.** Synthesis of adenosine-peptide conjugates for biological applications. Tartu, 2007, 114 p.
73. **Svetoslav Hristov Slavov.** Biomedical applications of the QSAR approach. Tartu, 2007, 146 p.
74. **Eneli Härk.** Electroreduction of complex cations on electrochemically polished Bi(*hkl*) single crystal electrodes. Tartu, 2008, 158 p.
75. **Priit Möller.** Electrochemical characteristics of some cathodes for medium temperature solid oxide fuel cells, synthesized by solid state reaction technique. Tartu, 2008, 90 p.
76. **Signe Viggor.** Impact of biochemical parameters of genetically different pseudomonads at the degradation of phenolic compounds. Tartu, 2008, 122 p.
77. **Ave Sarapuu.** Electrochemical reduction of oxygen on quinone-modified carbon electrodes and on thin films of platinum and gold. Tartu, 2008, 134 p.
78. **Agnes Kütt.** Studies of acid-base equilibria in non-aqueous media. Tartu, 2008, 198 p.
79. **Rouvim Kadis.** Evaluation of measurement uncertainty in analytical chemistry: related concepts and some points of misinterpretation. Tartu, 2008, 118 p.
80. **Valter Reedo.** Elaboration of IVB group metal oxide structures and their possible applications. Tartu, 2008, 98 p.
81. **Aleksei Kuznetsov.** Allosteric effects in reactions catalyzed by the cAMP-dependent protein kinase catalytic subunit. Tartu, 2009, 133 p.

82. **Aleksei Bredihhin.** Use of mono- and polyanions in the synthesis of multisubstituted hydrazine derivatives. Tartu, 2009, 105 p.
83. **Anu Ploom.** Quantitative structure-reactivity analysis in organosilicon chemistry. Tartu, 2009, 99 p.
84. **Argo Vonk.** Determination of adenosine A<sub>2A</sub>- and dopamine D<sub>1</sub> receptor-specific modulation of adenylate cyclase activity in rat striatum. Tartu, 2009, 129 p.
85. **Indrek Kivi.** Synthesis and electrochemical characterization of porous cathode materials for intermediate temperature solid oxide fuel cells. Tartu, 2009, 177 p.
86. **Jaanus Eskusson.** Synthesis and characterisation of diamond-like carbon thin films prepared by pulsed laser deposition method. Tartu, 2009, 117 p.
87. **Marko Lätt.** Carbide derived microporous carbon and electrical double layer capacitors. Tartu, 2009, 107 p.
88. **Vladimir Stepanov.** Slow conformational changes in dopamine transporter interaction with its ligands. Tartu, 2009, 103 p.
89. **Aleksander Trummal.** Computational Study of Structural and Solvent Effects on Acidities of Some Brønsted Acids. Tartu, 2009, 103 p.
90. **Eerold Vellemäe.** Applications of mischmetal in organic synthesis. Tartu, 2009, 93 p.
91. **Sven Parkel.** Ligand binding to 5-HT<sub>1A</sub> receptors and its regulation by Mg<sup>2+</sup> and Mn<sup>2+</sup>. Tartu, 2010, 99 p.
92. **Signe Vahur.** Expanding the possibilities of ATR-FT-IR spectroscopy in determination of inorganic pigments. Tartu, 2010, 184 p.
93. **Tavo Romann.** Preparation and surface modification of bismuth thin film, porous, and microelectrodes. Tartu, 2010, 155 p.
94. **Nadežda Aleksejeva.** Electrocatalytic reduction of oxygen on carbon nanotube-based nanocomposite materials. Tartu, 2010, 147 p.
95. **Marko Kullapere.** Electrochemical properties of glassy carbon, nickel and gold electrodes modified with aryl groups. Tartu, 2010, 233 p.
96. **Liis Siinor.** Adsorption kinetics of ions at Bi single crystal planes from aqueous electrolyte solutions and room-temperature ionic liquids. Tartu, 2010, 101 p.
97. **Angela Vaasa.** Development of fluorescence-based kinetic and binding assays for characterization of protein kinases and their inhibitors. Tartu 2010, 101 p.
98. **Indrek Tulp.** Multivariate analysis of chemical and biological properties. Tartu 2010, 105 p.
99. **Aare Selberg.** Evaluation of environmental quality in Northern Estonia by the analysis of leachate. Tartu 2010, 117 p.
100. **Darja Lavõgina.** Development of protein kinase inhibitors based on adenosine analogue-oligoarginine conjugates. Tartu 2010, 248 p.
101. **Laura Herm.** Biochemistry of dopamine D<sub>2</sub> receptors and its association with motivated behaviour. Tartu 2010, 156 p.

102. **Terje Raudsepp.** Influence of dopant anions on the electrochemical properties of polypyrrole films. Tartu 2010, 112 p.
103. **Margus Marandi.** Electroformation of Polypyrrole Films: *In-situ* AFM and STM Study. Tartu 2011, 116 p.
104. **Kairi Kivirand.** Diamine oxidase-based biosensors: construction and working principles. Tartu, 2011, 140 p.
105. **Anneli Kruve.** Matrix effects in liquid-chromatography electrospray mass-spectrometry. Tartu, 2011, 156 p.
106. **Gary Urb.** Assessment of environmental impact of oil shale fly ash from PF and CFB combustion. Tartu, 2011, 108 p.
107. **Nikita Oskolkov.** A novel strategy for peptide-mediated cellular delivery and induction of endosomal escape. Tartu, 2011, 106 p.
108. **Dana Martin.** The QSPR/QSAR approach for the prediction of properties of fullerene derivatives. Tartu, 2011, 98 p.
109. **Säde Viirlaid.** Novel glutathione analogues and their antioxidant activity. Tartu, 2011, 106 p.
110. **Ülis Sõukand.** Simultaneous adsorption of Cd<sup>2+</sup>, Ni<sup>2+</sup>, and Pb<sup>2+</sup> on peat. Tartu, 2011, 124 p.
111. **Lauri Lipping.** The acidity of strong and superstrong Brønsted acids, an outreach for the “limits of growth”: a quantum chemical study. Tartu, 2011, 124 p.
112. **Heisi Kurig.** Electrical double-layer capacitors based on ionic liquids as electrolytes. Tartu, 2011, 146 p.
113. **Marje Kasari.** Bisubstrate luminescent probes, optical sensors and affinity adsorbents for measurement of active protein kinases in biological samples. Tartu, 2012, 126 p.
114. **Kalev Takkis.** Virtual screening of chemical databases for bioactive molecules. Tartu, 2012, 122 p.
115. **Ksenija Kisseljova.** Synthesis of aza-β<sup>3</sup>-amino acid containing peptides and kinetic study of their phosphorylation by protein kinase A. Tartu, 2012, 104 p.
116. **Riin Rebane.** Advanced method development strategy for derivatization LC/ESI/MS. Tartu, 2012, 184 p.
117. **Vladislav Ivaništšev.** Double layer structure and adsorption kinetics of ions at metal electrodes in room temperature ionic liquids. Tartu, 2012, 128 p.
118. **Irja Helm.** High accuracy gravimetric Winkler method for determination of dissolved oxygen. Tartu, 2012, 139 p.
119. **Karin Kipper.** Fluoroalcohols as Components of LC-ESI-MS Eluents: Usage and Applications. Tartu, 2012, 164 p.
120. **Arno Ratas.** Energy storage and transfer in dosimetric luminescent materials. Tartu, 2012, 163 p.
121. **Reet Reinart-Okugbeni.** Assay systems for characterisation of subtype-selective binding and functional activity of ligands on dopamine receptors. Tartu, 2012, 159 p.

122. **Lauri Sikk.** Computational study of the Sonogashira cross-coupling reaction. Tartu, 2012, 81 p.
123. **Karita Raudkivi.** Neurochemical studies on inter-individual differences in affect-related behaviour of the laboratory rat. Tartu, 2012, 161 p.
124. **Indrek Saar.** Design of GalR2 subtype specific ligands: their role in depression-like behavior and feeding regulation. Tartu, 2013, 126 p.
125. **Ann Laheäär.** Electrochemical characterization of alkali metal salt based non-aqueous electrolytes for supercapacitors. Tartu, 2013, 127 p.
126. **Kerli Tõnurist.** Influence of electrospun separator materials properties on electrochemical performance of electrical double-layer capacitors. Tartu, 2013, 147 p.
127. **Kaija Põhako-Esko.** Novel organic and inorganic ionogels: preparation and characterization. Tartu, 2013, 124 p.
128. **Ivar Kruusenberg.** Electroreduction of oxygen on carbon nanomaterial-based catalysts. Tartu, 2013, 191 p.
129. **Sander Piiskop.** Kinetic effects of ultrasound in aqueous acetonitrile solutions. Tartu, 2013, 95 p.
130. **Ilona Faustova.** Regulatory role of L-type pyruvate kinase N-terminal domain. Tartu, 2013, 109 p.
131. **Kadi Tamm.** Synthesis and characterization of the micro-mesoporous anode materials and testing of the medium temperature solid oxide fuel cell single cells. Tartu, 2013, 138 p.
132. **Iva Bozhidarova Stoyanova-Slavova.** Validation of QSAR/QSPR for regulatory purposes. Tartu, 2013, 109 p.
133. **Vitali Grozovski.** Adsorption of organic molecules at single crystal electrodes studied by *in situ* STM method. Tartu, 2014, 146 p.
134. **Santa Veikšina.** Development of assay systems for characterisation of ligand binding properties to melanocortin 4 receptors. Tartu, 2014, 151 p.
135. **Jüri Liiv.** PVDF (polyvinylidene difluoride) as material for active element of twisting-ball displays. Tartu, 2014, 111 p.
136. **Kersti Vaarmets.** Electrochemical and physical characterization of pristine and activated molybdenum carbide-derived carbon electrodes for the oxygen electroreduction reaction. Tartu, 2014, 131 p.
137. **Lauri Tõntson.** Regulation of G-protein subtypes by receptors, guanine nucleotides and Mn<sup>2+</sup>. Tartu, 2014, 105 p.
138. **Aiko Adamson.** Properties of amine-boranes and phosphorus analogues in the gas phase. Tartu, 2014, 78 p.
139. **Elo Kibena.** Electrochemical grafting of glassy carbon, gold, highly oriented pyrolytic graphite and chemical vapour deposition-grown graphene electrodes by diazonium reduction method. Tartu, 2014, 184 p.
140. **Teemu Näykki.** Novel Tools for Water Quality Monitoring – From Field to Laboratory. Tartu, 2014, 202 p.
141. **Karl Kaupmees.** Acidity and basicity in non-aqueous media: importance of solvent properties and purity. Tartu, 2014, 128 p.

142. **Oleg Lebedev.** Hydrazine polyanions: different strategies in the synthesis of heterocycles. Tartu, 2015, 118 p.
143. **Geven Piir.** Environmental risk assessment of chemicals using QSAR methods. Tartu, 2015, 123 p.
144. **Olga Mazina.** Development and application of the biosensor assay for measurements of cyclic adenosine monophosphate in studies of G protein-coupled receptor signaling. Tartu, 2015, 116 p.
145. **Sandip Ashokrao Kadam.** Anion receptors: synthesis and accurate binding measurements. Tartu, 2015, 116 p.
146. **Indrek Tallo.** Synthesis and characterization of new micro-mesoporous carbide derived carbon materials for high energy and power density electrical double layer capacitors. Tartu, 2015, 148 p.
147. **Heiki Erikson.** Electrochemical reduction of oxygen on nanostructured palladium and gold catalysts. Tartu, 2015, 204 p.
148. **Erik Anderson.** *In situ* Scanning Tunnelling Microscopy studies of the interfacial structure between Bi(111) electrode and a room temperature ionic liquid. Tartu, 2015, 118 p.
149. **Girinath G. Pillai.** Computational Modelling of Diverse Chemical, Biochemical and Biomedical Properties. Tartu, 2015, 140 p.
150. **Piret Pikma.** Interfacial structure and adsorption of organic compounds at Cd(0001) and Sb(111) electrodes from ionic liquid and aqueous electrolytes: an *in situ* STM study. Tartu, 2015, 126 p.
151. **Ganesh babu Manoharan.** Combining chemical and genetic approaches for photoluminescence assays of protein kinases. Tartu, 2016, 126 p.
152. **Carolyn Siimenson.** Electrochemical characterization of halide ion adsorption from liquid mixtures at Bi(111) and pyrolytic graphite electrode surface. Tartu, 2016, 110 p.
153. **Asko Laaniste.** Comparison and optimisation of novel mass spectrometry ionisation sources. Tartu, 2016, 156 p.
154. **Hanno Evard.** Estimating limit of detection for mass spectrometric analysis methods. Tartu, 2016, 224 p.
155. **Kadri Ligi.** Characterization and application of protein kinase-responsive organic probes with triplet-singlet energy transfer. Tartu, 2016, 122 p.
156. **Margarita Kagan.** Biosensing penicillins' residues in milk flows. Tartu, 2016, 130 p.
157. **Marie Kriisa.** Development of protein kinase-responsive photoluminescent probes and cellular regulators of protein phosphorylation. Tartu, 2016, 106 p.
158. **Mihkel Vestli.** Ultrasonic spray pyrolysis deposited electrolyte layers for intermediate temperature solid oxide fuel cells. Tartu, 2016, 156 p.
159. **Silver Sepp.** Influence of porosity of the carbide-derived carbon on the properties of the composite electrocatalysts and characteristics of polymer electrolyte fuel cells. Tartu, 2016, 137 p.
160. **Kristjan Haav.** Quantitative relative equilibrium constant measurements in supramolecular chemistry. Tartu, 2017, 158 p.

161. **Anu Teearu.** Development of MALDI-FT-ICR-MS methodology for the analysis of resinous materials. Tartu, 2017, 205 p.
162. **Taavi Ivan.** Bifunctional inhibitors and photoluminescent probes for studies on protein complexes. Tartu, 2017, 140 p.
163. **Maarja-Liisa Oldekop.** Characterization of amino acid derivatization reagents for LC-MS analysis. Tartu, 2017, 147 p.
164. **Kristel Jukk.** Electrochemical reduction of oxygen on platinum- and palladium-based nanocatalysts. Tartu, 2017, 250 p.
165. **Siim Kukk.** Kinetic aspects of interaction between dopamine transporter and *N*-substituted nortropine derivatives. Tartu, 2017, 107 p.
166. **Birgit Viira.** Design and modelling in early drug development in targeting HIV-1 reverse transcriptase and Malaria. Tartu, 2017, 172 p.
167. **Rait Kivi.** Allosteric in cAMP dependent protein kinase catalytic subunit. Tartu, 2017, 115 p.
168. **Agnes Heering.** Experimental realization and applications of the unified acidity scale. Tartu, 2017, 123 p.
169. **Delia Juronen.** Biosensing system for the rapid multiplex detection of mastitis-causing pathogens in milk. Tartu, 2018, 85 p.
170. **Hedi Rahnel.** ARC-inhibitors: from reliable biochemical assays to regulators of physiology of cells. Tartu, 2018, 176 p.
171. **Anton Ruzanov.** Computational investigation of the electrical double layer at metal–aqueous solution and metal–ionic liquid interfaces. Tartu, 2018, 129 p.
172. **Katrin Kestav.** Crystal Structure-Guided Development of Bisubstrate-Analogue Inhibitors of Mitotic Protein Kinase Haspin. Tartu, 2018, 166 p.
173. **Mihkel Ilisson.** Synthesis of novel heterocyclic hydrazine derivatives and their conjugates. Tartu, 2018, 101 p.
174. **Anni Allikalt.** Development of assay systems for studying ligand binding to dopamine receptors. Tartu, 2018, 160 p.
175. **Ove Oll.** Electrical double layer structure and energy storage characteristics of ionic liquid based capacitors. Tartu, 2018, 187 p.
176. **Rasmus Palm.** Carbon materials for energy storage applications. Tartu, 2018, 114 p.
177. **Jürgen Metsik.** Preparation and stability of poly(3,4-ethylenedioxythiophene) thin films for transparent electrode applications. Tartu, 2018, 111 p.
178. **Sofja Tšepelevitš.** Experimental studies and modeling of solute-solvent interactions. Tartu, 2018, 109 p.
179. **Märt Lõkov.** Basicity of some nitrogen, phosphorus and carbon bases in acetonitrile. Tartu, 2018, 104 p.
180. **Anton Mastitski.** Preparation of  $\alpha$ -aza-amino acid precursors and related compounds by novel methods of reductive one-pot alkylation and direct alkylation. Tartu, 2018, 155 p.
181. **Jürgen Vahter.** Development of bisubstrate inhibitors for protein kinase CK2. Tartu, 2019, 186 p.

182. **Piia Liigand.** Expanding and improving methodology and applications of ionization efficiency measurements. Tartu, 2019, 189 p.
183. **Sigrīd Selberg.** Synthesis and properties of lipophilic phosphazene-based indicator molecules. Tartu, 2019, 74 p.
184. **Jaanus Liigand.** Standard substance free quantification for LC/ESI/MS analysis based on the predicted ionization efficiencies. Tartu, 2019, 254 p.
185. **Marek Mooste.** Surface and electrochemical characterisation of aryl film and nanocomposite material modified carbon and metal-based electrodes. Tartu, 2019, 304 p.
186. **Mare Oja.** Experimental investigation and modelling of pH profiles for effective membrane permeability of drug substances. Tartu, 2019, 306 p.
187. **Sajid Hussain.** Electrochemical reduction of oxygen on supported Pt catalysts. Tartu, 2019, 220 p.
188. **Ronald Väli.** Glucose-derived hard carbon electrode materials for sodium-ion batteries. Tartu, 2019, 180 p.
189. **Ester Tee.** Analysis and development of selective synthesis methods of hierarchical micro- and mesoporous carbons. Tartu, 2019, 210 p.
190. **Martin Maide.** Influence of the microstructure and chemical composition of the fuel electrode on the electrochemical performance of reversible solid oxide fuel cell. Tartu, 2020, 144 p.
191. **Edith Viirlaid.** Biosensing Pesticides in Water Samples. Tartu, 2020, 102 p.